Hard X-ray Probing of Dark Clouds: Protostar Structure and Magnetic Activities

Yohko TSUBOI

Department of Physics. Graduated School of Science,

Kyoto University, Sakyo-ku, Kyoto 606-8502, Japan

Submitted to the Department of Physics,

Kyoto University on January 5, 1999,

in partial fulfillment of the requirements for

the degree of Doctor of Philosophy

Abstract

A star is born from a molecular cloud core and evolves to main sequence through the protostellar and T Tauri phases. With the *ASCA* satellite, we probed 17 fields (totally 24 observations) of nearby dark clouds to search X-rays from protostars. In this survey, we detected X-rays from 40% of protostar candidates with $S/N > 5$ level in the 2–10 keV band. They include Class 0 protostars, i.e. earliest phase of protostars, which had never been detected before.

Based on the results of the outflow observations, we found that the X-ray detection of a protostar is highly dependent on the orientation of the outflow; the X-rays can only be detected from a pole-on viewing angle, where the X-rays penetrate through lower density of the bipolar flow and are less absorbed by dense circumstellar disks. X-ray non-detected protostars have edge-on geometry, hence the X-rays are completely blocked by an extremely high column along the circumstellar disk.

From two Class I protostars (EL29 and YLW15 in ρ Oph), we detected totally four X-ray flares. Their temperatures and emission measures during the flares lie on a universal correlation from solar micro flares to stellar giant flares. From a Class I protostar WL 6, we obtained sinusoidal modulation with constant temperature, which may be due to a spin of a protostar. The period is apparently shorter than the spin periods of the older stages. However, the relation between the X-ray luminosities and $V \sin i$, which are assumed from the period of WL 6, is similar to those in the older phase. These two results imply that at protostellar phase, X-rays in both the flare and quiescent states are emitted magnetically as well as the older phases of low-mass stars.

The flares from YLW 15 was quasi-periodic, which occurred every ∼20 hours. It is consistent with a quasi-periodic reheating of the same plasma loop of $\sim 14\,R_\odot$ with diameter-to-length ratio $a \sim 0.07$. The inferred large-scale magnetic structure and the observed periodicity imply that the reheating events of the same magnetic loop originate in an interaction between the star and the disk due to the differential rotation. This result gives us a crucial information about structure of the central star and its close vicinity, which can not be studied by any other wavelengths.

We detected an intermediate-mass protostar EC95, which exhibited time variability like contiguous flares with higher temperature than in typical T Tauri stars. Since the temperature and the emission measure is plotted on the same correlation with solar-type stars, our result would be the first support that even an intermediate-mass star has magnetic activity in the protostellar phase. They may have a convective zone inside the star itself or/and the inner disk, which has not been expected by any theory of stellar evolution.

Contents

1 Introduction & Review **1**

1.1 Molecular Clouds in Our Galaxy 1

1.1.1 Giant Molecular Cloud 1

1.1.2 Dark Cloud 2

1.1.3 Gould's Belt 2

1.2 Evolution of Young Stellar Objects 5

1.2.1 Classification at Near Infrared Band 5

1.2.2 Classification at milli/submillimeter band 6

1.2.3 Classification by Bolometric Temperature 7

1.3 Outflows from YSOs 9

1.3.1 Features 9

1.3.2 Origin 10

1.4 X-rays from YSOs 13

1.4.1 *Einstein* and *ROSAT* Observations 13

1.4.2 *Temma* and *Ginga* Observations 14

1.4.3 *ASCA* Observations and Unsolved Problems 15

2 Instrument **22**

2.1 *ASCA* 22

2.1.1 XRT 23

2.1.2 GIS 27

2.1.3 SIS 33

3 Observations **40**

3.1 Protostar Sampling 40

3.2 Observed Field 40

3.3 Observation Mode 40
3.3.1 GIS 41
3.3.2 SIS 41
3.4 Images 41
3.5 Detection Criteria 42

4 Rho Ophiuchi (D = 165 pc) 47
4.1 Core region (PV phase) 49
4.1.1 EL 29 49
4.1.2 WL 6 50
4.2 Core region (AO6) 55
4.2.1 YLW15 56
4.3 East region (AO4: 1996 Mar 3) 62

5 Coronae Australis (D = 130 pc) 64
5.1 Core region 1 (AO 4 the 1st day) 65
5.2 Core region 1 (AO 4 the 2nd day) 68
5.3 Core region 2 (AO 6) 70

6 Taurus (D = 140 pc) 72
6.1 B209 region (AO2) 73
6.2 B209 (AO3, the 1st day) 76
6.3 B209 (AO3, the 2nd day) 78
6.4 TMC1 80
6.5 IC359 82
6.6 L1551 84

7 Lupus (D = 140 pc) 86
7.1 Lupus3 87

8 Serpens (D = 310 pc) 90
8.1 Core region 91
8.1.1 EC95 91

9 Perseus (D = 200–350 pc) 96
9.1 NGC1333 96

9.2 L1448 99

10 Orion (D = 450 pc) 102

10.1 NGC1977 104
10.2 Orion Nebula (M42) (PV) 107
10.3 Orion Nebula (M42) (AO 5) 110
10.4 L1641 North 113
10.5 HH212 115
10.6 HH91 117
10.7 L1582B 119

11 Discussions 121

11.1 X-ray Loud vs. X-ray Quiescent 121
11.1.1 Age Effect: When a Star Begins to Emit X-rays ? 126
11.1.2 Stellar Mass Effect 129
11.1.3 Long Term Variability Effect 130
11.1.4 Geometry Effect: A Unified Picture ? 130
11.1.5 Host Cloud Effect: Magnetic Field Orientation 139
11.2 Mechanism of X-ray Flares 140
11.2.1 Individual Flare (1) — EL29 140
11.2.2 Individual Flare (2) — YLW15 141
11.2.3 kT vs. EM 146
11.2.4 Flare Scales 147
11.3 Emission Mechanism of Persistent X-rays 150
11.3.1 L_X vs. $V \sin i$ 150
11.3.2 kT vs. EM 151
11.4 Intermediate-mass Protostars 154

12 Summary 155

A Determination of Physical Parameters of the Flares 159

A.1 Loop Parameters 159
A.2 Magnetic Field 161
A.3 Released Energy 161

Chapter 1

Introduction & Review

1.1 Molecular Clouds in Our Galaxy

In our Galaxy, about a half of the mass of interstellar gas (2–$4\times10^9 M_\odot$) is believed to exist as molecular clouds. Distribution of molecular clouds in the Milky Way is shown in Figure 1.1 (Dame et al. 1987) and Figure 1.2 (Dame et al. 1987).

1.1.1 Giant Molecular Cloud

A large molecular cloud, which has mass of 10^5–$3\times10^6 M_\odot$ and several 10 pc scale, is generally called a Giant Molecular Cloud (hearafter GMC). GMCs are thought to contain most of molecular gas in our Galaxy. GMCs are distributed along spiral arms of the Galactic plane, and do not exist in inter-arms. GMCs are believed to be the places where both the low-mass star ($< 3M_\odot$) formation and high-mass star ($> 3M_\odot$) formation occur simultaneously. The most famous example of GMCs is the Orion molecular cloud ($d \sim 450$ pc).

Radio mapping of the ^{13}CO line, which traces relatively low density region, has revealed that a GMC consists of "clumps", of which the mass, scale, and density are $M \approx 10^3$–$10^4 M_\odot$, $R \approx$2–5 pc, $N_{H_2} \approx 10^{2.5}\mathrm{cm}^{-3}$, respectively. Mapping of the C^{18}O or CS line, which traces relatively higher density region, has revealed that the clumps consist of still smaller and higher density clumps "molecular cloud cores", of which the scale are typically $R \approx$0.1–0.3 pc. Half of the molecular core is associated with "IRAS source" which was detected in far- to mid-infrared band of *IRAS* satellite.

1.1.2 Dark Cloud

Relatively smaller molecular cloud, neighbored with the Sun, is generally called a "dark cloud". The mass is about 1/1000–1/100 of that of GMC. Dark clouds are known to be the places where low-mass star formation occur. The Taurus ($d \sim$ 140 pc) and ρ Oph ($d \sim 165$ pc) dark clouds are famous examples of dark clouds. As well as GMC, observations with various kind of molecular lines have revealed the hierarchical density structure. The molecular cloud cores have typical mass, scale, temperature, and density of $M \approx 4M_{\odot}$, $R \approx 0.1$ pc, $T \approx 1$– 11 K, $N_{H_2} \approx$ 3–80$\times 10^4$cm^{-3}, respectively (Myers & Benson 1983, Mizuno et al. 1994).

1.1.3 Gould's Belt

The dark clouds Lupus and ρ Oph lie at the positive Galactic latitude, while the Orion and Taurus clouds are at the negative-latitude. It indicates the molecular clouds within 500 pc from the Sun follow the "Gould's Belt" (GB hereafter). Gould (1879) found asymmetry in the distribution of the brightest stars on the sky with respect to the Galactic equator, more than one century ago. It has an ellipsoidal shape with a semi-major axis of about 500 pc and a semi-minor axis of about 340 pc, the Sun being located 150 to 250 pc off center. He concluded that these bright stars were aligned along a great circle crossing the Milky-Way at an angle close to 20°. Since then many astronomers have worked on this structure, and confirmed its existence in OB associations or young Galactic clusters, gas, and dust. Recently, Guillout et al. (1998a, b) confirmed with the ROSAT all sky survey that X-ray selected young stars also distribute along the GB.

For the formation of the GB, several scenario such as collisions of high velocity clouds with the Galactic disk (e.g. Comerón & Torra 1992, 1994), supernova explosions, or induced star formation by strong stellar winds originating at a center of Cas-Tau association (e.g. Blaauw 1991) have been proposed. On the other hand, some authors have pointed out that even a random spatial distribution of a few prominent OB associations (which are usually selected to trace the GB) would mimic the impression of an "inclined belt" in the sky. Despite of these many models or scenarios, the origin is thus still a puzzle. An extensive review of the present knowledge on the GB system and the interstellar medium can be found in Pöpel (1997) and references therein.

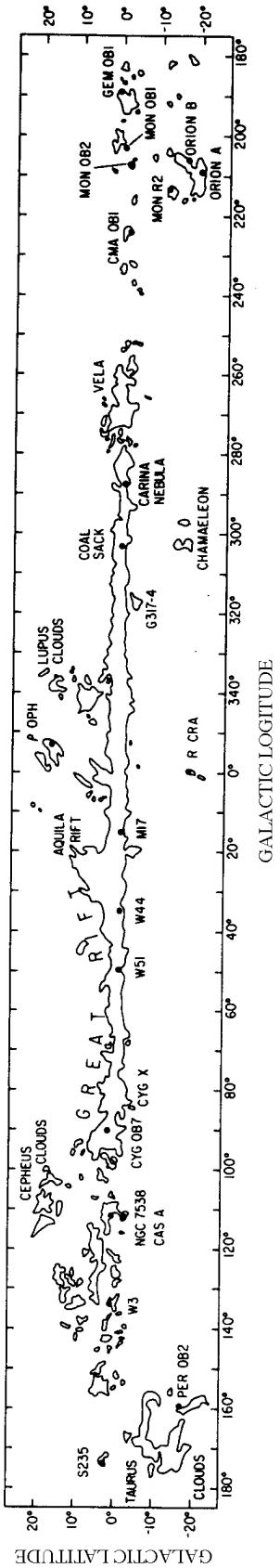

Figure 1.1: The velocity-integrated CO map of the Milky Way obtained by Dame et al. (1987).

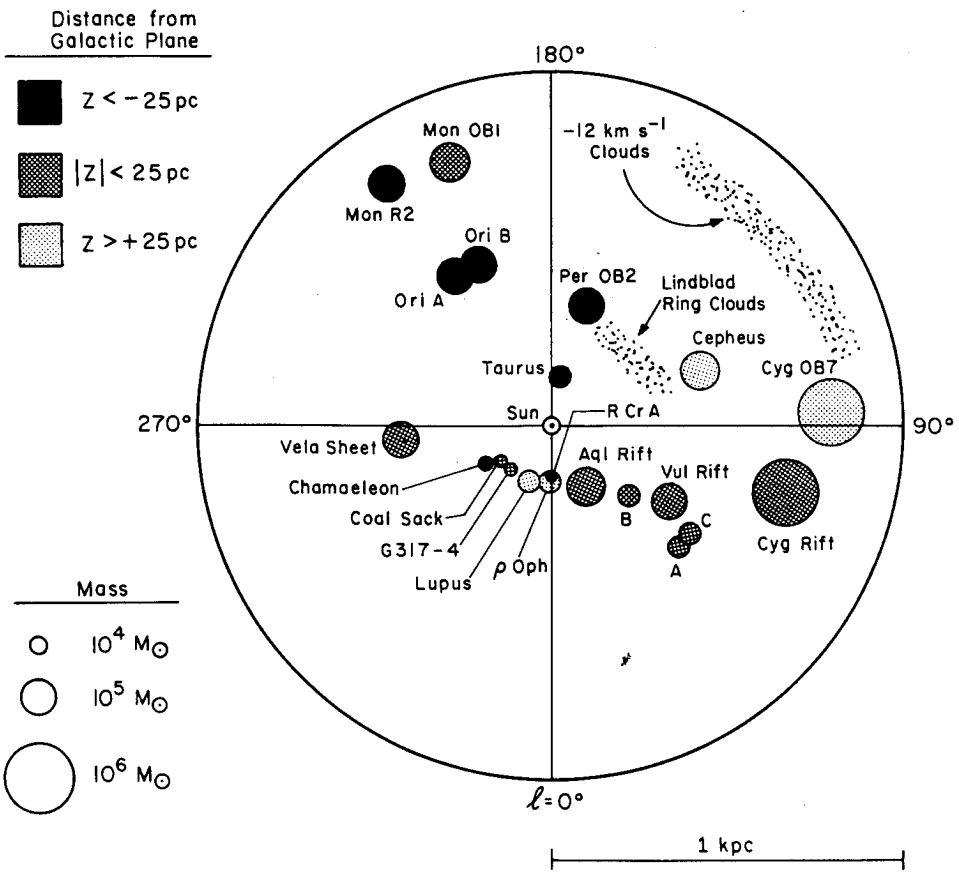

Figure 1.2: The distribution in the Galactic plane of molecular clouds within 1 kpc of the Sun (Dame et al. 1987). The circle radii are proportional to the cube roots of the cloud masses and in most cases are close to the cloud's actual radii. The shading indicates distance from the Galactic plane.

1.2 Evolution of Young Stellar Objects

Early stellar evolution is reviewed by Shu, Adams, & Lizano (1987) and André & Montmerle (1994). In this section, we briefly review the essence. A star is born deep in a molecular cloud and evolve to the main-sequence through a "young stellar object" (YSO). A large fraction of YSOs is either optically invisible or too faint for spectral typing. Its radiation is not a single blackbody spectrum, hence we can hardly trace the evolution of YSOs along a simple scheme like the Hertzsprung-Russell (H-R) diagram as performed by Cohen & Kuhi (1979).

Near-IR spectroscopic studies have placed embedded sources onto the H-R diagram (Greene & Meyer 1995; Greene & Lada 1996), but the number of observed sources is still limited. In practice, most of the YSOs are classified with a broadband infrared photometry: spectral energy distribution (SED: Lada 1987).

1.2.1 Classification at Near Infrared Band

YSOs are believed to evolve by losing a circumstellar material via accretion and outflow. Then the near-infrared band, which is emitted from the circumstellar material, is used for the classification of YSOs. Generally, the spectral index [$\alpha_{IR} = -d \log \nu \mathrm{F}\nu / d \log \nu$] in the infrared band up to 2.2 μm is used for the classification (Lada & Wilking 1984, Adams et al. 1987, Lada 1991).

Class I objects ($\alpha_{IR} > 0$) have the SED peak in the millimeter or infrared bands. The SED is broader than a single blackbody function, probably due to an integrated emission from a hot (3000–5000 K) stellar-like object and warm (300–1000 K) dusty envelopes around it.

These YSOs (Class 0 and I) are associated with dense molecular cores (Myers et al. 1987) and bipolar flows, suggesting dynamic gas accretion phase, which would correspond to a protostellar phase. The ages are thought to be $\sim 10^{4-5}$ yr.

Class II objects ($\alpha_{IR} < 0$) are thought to have exhausted most of the envelope, leaving a circumstellar disk, hence have peaks at the near-infrared band. The SEDs are also broader than a single temperature blackbody, due to contribution of circumstellar disks. The central stars are optically visible and correspond to Classical T Tauri stars (CTTS: $\sim 10^6$ yr).

Class III objects ($\alpha_{IR} < 0$) have blackbody-like spectra. They include pre-main sequence stars surrounded by optically thin disks, very young stars of the

main sequence and "naked" T Tauri stars (Weak-lined T Tauri Stars, WTTS: $\sim 10^7$ yr) (Walter et al. 1988).

1.2.2 Classification at milli/submillimeter band

In addition to Class I–III, the observations with bolometers at millimeter wavelengths have revealed the existence of colder sources that do not fit in the classification scheme depicted above. Such objects are called "Class 0" sources (André et al. 1993) or "extreme Class I" sources (Lada 1991). They are thought to be in an evolutionary stage prior to Class I.

A Class 0 protostar is defined as a (sub)millimeter source with three attributes (André et al. 1993; Barsony 1995): (1) at most, weak emission at $\lambda < 10\mu$m, (2) a spectral energy distribution similar to a blackbody at 15–30 K, and (3) $L_{submm}/L_{bol} > 5 \times 10^{-3}$, where L_{submm} is luminosity measured at $\lambda > 350\mu$m and L_{bol} is a bolometric luminosity. Class 0 protostars can be observationally distinguished from the pre-protostellar cores (see below) by detection of a centimeter source (ionized gas) or an outflow, which is indirect evidence for a central core.

Radiation in the millimeter wavelengths is due to the gravitational energy release of accreting circumstellar envelope. The millimeter fluxes from Class 0 objects (André & Montmerle 1994) have shown that the envelope gas has not been fully accumulated to the central star: the stellar mass is smaller than the envelope mass, $M_{env} > M_*$). The central star in the Class I objects, on the other hand, has already accumulated most of the stellar mass, ($M_{env} < M_*$). The SEDs of these different classes have been successfully modeled by assuming a systematic dispersal of the total circumstellar mass from Class 0 to Class III (Adams et al. 1987, Kenyon et al. 1993); the circumstellar mass decreases by a factor of 5–10 from one class to the next (André & Montmerle 1994). The evolutionary sequence from Class 0 to III (by André 1994) is summarized in Figure 1.3.

Pre-protostellar cores prior to the start of gravitational collapse can also be identified by mapping the millimeter/submillimeter (Benson & Myers 1989, Ward-Thompson et al. 1994) and molecular line (Mizuno et al. 1994) emission in dark clouds. Mizuno et al. (1994) revealed that the time-scale of the pre-protostellar phase is a few hundred thousand years. They showed that the pre-protostellar cores are, in contrast to the results of Benson & Myers (1989), less dense and more

extended than those of protostellar cores.

1.2.3 Classification by Bolometric Temperature

Another useful parameter to classify the YSOs in the SED scheme is the bolometric temperature (T_{bol}; Myers & Ladd 1993): a blackbody temperature with the mean frequency equal to that of the observed continuum spectrum. The temperatures represent the circumstellar conditions. Compared with the other methods, T_{bol} uses all the photometric information of a YSO (see Myers & Ladd 1993), and then can be applied to a wide range of YSOs, including all the four spectral classes (Chen et al. 1995, 1997). T_{bol} increases monotonically from Class 0 objects to Classes I, II, and III, corresponding to the SED evolution. Typical T_{bol} for Class 0, I, II and III sources are, respectively, $\leq$ 100 K, $\sim$700 K, $\sim$2000 K and $\sim$3500 K. The log-log diagram of L_{bol} vs. T_{bol} (the BLT diagram) for YSOs is analogous to the H-R diagram for the main sequence stars. The BLT diagram can be used to compare observations with theoretical evolutionary models and to study in comparison of different star-forming regions (Chen et al. 1995, 1997).

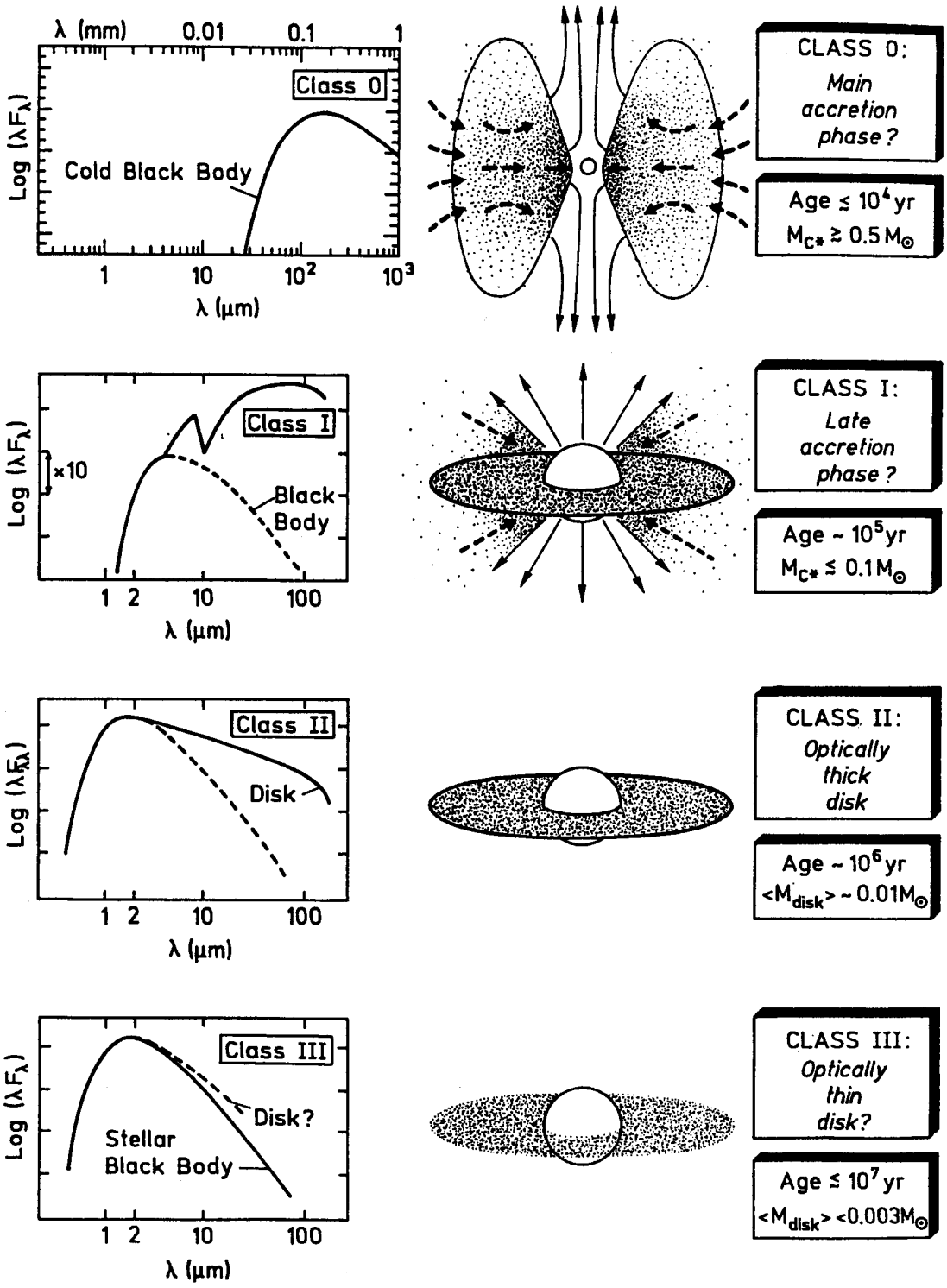

Figure 1.3: Evolutionary sequence of the spectral energy distributions for low-mass YSOs proposed by André (1994). The four panels (Classes 0, I, II, and III) correspond to successive stages of evolution.

1.3 Outflows from YSOs

1.3.1 Features

With the radio molecular-line observation, Snell et al. (1980) unexpectedly discovered an outflow from a protostar L1551 IRS5. Since then, outflow features have been observed in various forms; molecular outflow (in the other word, standard CO outflow), optical HH jet, collimated H_2 molecular jet, Radio Continuum Jet, and Atomic Neutral Jet. The outflow activity is more efficient in Class 0 than Class I.

The standard CO outflow has usually a bipolar structure emerging from a close vicinity of a central star. The total mass of a molecular flow can range from less than 10^{-2} $M_\odot$ (e.g. HH 34; Chernin & Masson 1995a, Terebey et al. 1989) to $\sim 200 M_\odot$ (e.g. Mon R2, Wolf et al. 1990; DR21, Russell et al. 1992). The outflow sizes ranges from less than 0.1 pc (e.g. Ori-I-2, Cernicharo et al. 1992) to $\sim$5 pc. The velocity is generally only a few km s^{-1}. The total kinetic energy of the CO outflow can reach 10^{47}–10^{48} erg (e.g. DR21, Garden et al. 1991). The measured dynamical time scales range from 10^3 to a few 10^5 years. The collimation factor is typically ranging from 2 to 5 (e.g. Richer et al. 1992).

The optical HH jet sometimes contains multiple bow shocks (e.g. HH 34; Reipurth et al. 1986, Bührke et al. 1988, Reipurth & Heathcote 1992, Morse et al. 1992) and extends up to 1.5 pc (Bally & Devine 1994). In many cases, these HH jets have the same orientation, similar extension, and compatible kinematics to the corresponding CO outflows (HH 34: Chernin & Masson 1995a; HH 111: Reipurth & Cernicharo 1995, Cernicharo & Reipurth 1996; HH complexes in L1551: Mundt & Fried 1983, Snell et al. 1980). The HH jets are generally highly collimated, with collimation factors of up to 100. The velocity is generally as high as several 100 km s^{-1}.

The collimated molecular jets characteristic of strong H_2 emission are detected around many Class 0 YSOs, including L1448-mm (Terebey 1991, Bally et al. 1993b, Davis et al. 1994a), IRAS 03282 (Bally et al. 1993a, Bachiller et al. 1994b), IC 348-mm (McCaughrean et al. 1994), VLA 1623 (Dent et al. 1995), and L1157-mm (Hodapp 1994, Davis & Eislöffel 1995). Most of the H_2 molecular jets have short kinematical ages of < 1000 yr (e.g. McCaughrean et al. 1994), and the H_2 emissions form a cocoon shape around the HH jet: i.e. long filaments, which are

not strictly coincident with an axis of the HH jet. The H_2 lines thus are emitted in the mixing layer between ambient and out-flowing materials. The velocity of the H_2 molecular jet is in the range 10–50 km s^{-1} (Shull & Beckwith 1982, Draine et al. 1983, Smith 1994).

The radio continuum jet emerges as a continuum emission at the centimeter wavelengths (Cohen et al. 1982, Bieging et al. 1984, Bieging & Cohen 1985). Most of them are interpreted as free-free emission from a collimated thermal jet (Reynolds 1986), while some of them showed spectral indices characteristic of non-thermal synchrotron emission (e.g. Serpens/FIR1: Curiel et al. 1993; HH 222: Yusef-Zadeh et al. 1990; RCrA IRS7: Brown 1987). The coexistence of thermal and non-thermal radio emission in the YSO jets has been modeled by Henriksen et al. (1991), who suggest that the non-thermal emission is due to relativistic electrons possibly accelerated by a diffusive shock at the region of interaction between the jet and the ambient cloud material.

The atomic neutral jet has been observed with HI 21 cm lines around a few low-mass YSOs such as HH 7–11/IRS, L1551/IRS, and T Tau (Lizano et al. 1988, Giovanardi et al. 1992, Rodríguez et al. 1990, Ruiz et al. 1992). The broad wings indicative of winds of up to 200 km s^{-1} and the mass-loss rates of 10^{-6} to 10^{-5} $M_\odot$ yr^{-1} have been revealed. HI emissions have also been detected in two high-mass bipolar outflows (NGC 2071, Bally & Stark 1983; DR21, Russell et al. 1992).

1.3.2 Origin

The outflows from YSOs have following puzzles as well as the other space jets (AGNs, SS433).

- acceleration and engine

  Is there any kind of pressure, buoyancy, or system like de Laval nozzles ?

- support mechanism of the orientation

  Jets are bipolar, and extend 10^5–10^7 times larger than the central engine. What mechanisms support the orientation ?

- collimation

  They have generally high collimation factors (excluding the CO molecular outflows). What collimates them ?

To address these questions, many magnetically driven jets model have been proposed and numerically simulated. These models can be divided into two categories, depending on whether the jet arises at the disk surface or at the star/disk boundary layer. In both cases, accretion disks can provide momentum and energy to bipolar molecular outflows.

Königl (1989) was the first to consider the disk structure with realistic magnetic fields. Wardle & Königl (1993) refined this model for the disk structure. Pringle (1989) suggested that a strong toroidal magnetic field could be produced at the boundary layer between the accretion disk and the star by a dynamo effect, but the details of the ejection process were not modeled. Other models that place the origin of the jet at the boundary layer have been proposed by Camenzind (1990), Bertout & Regev (1992), Ferreira & Pelletier (1993a, 1993b, 1995).

The most popular model of this category is that of the X-celerator. This model assumed initially (Shu et al. 1988) that the jet was generated at the region of the stellar equator where centrifugal and gravitational forces are compensated (the X-point). The YSO was assumed to have a strong magnetic field and was able to continue accreting by ejecting a strong outflow at a significant fraction of the in-fall rate. Since the mass-loss happens on the equatorial plane, the optical jets are produced by the expansion of the flow toward the rotational poles. The main difficulty of this model is that the star needs to rotate at the break-up velocity at its equator, while actual T Tauri stars are known to rotate at about a tenth of this velocity (Bouvier et al. 1986). The X-celerator model has been modified (Shu et al. 1994a, 1994b; Najita & Shu 1994; Ostriker & Shu 1995) to allow for the star rotating velocity below that of break-up. Following a suggestion by Königl (1991), it is assumed that the stellar magnetic field is strong enough to truncate the disk at a radius from the star. The rapid rotation of the material in a small region around this radius may drive a funnel inflow into the star together with a X-type outflow.

While Shu et al. (1994a) assumed partially open magnetic fields in the magnetosphere between the central star and the disk, Hayashi et al. (1996) assumed that the dipole magnetic field of the central star thread the rotating disk, performed 2.5-dementional MHD simulations, and reproduced a unified picture in which both X-ray flares and outflows are originated simultaneously by reconnection of the loop between star and disk.

These ideas which link outflows and disks are supported by observational results. In T Tauri stars, forbidden line emission, which is thought to arise from an outflow, is only seen in objects presenting near-IR excesses attributed to disks (Edwards 1995), and the intensity of the high-velocity emission seen in the [OI] 6300 Å line is correlated with the near-IR color excess (Edwards et al. 1993). More than 80% of YSOs with the outflows have circumstellar disks (Strom 1995, Dougados et al. 1996). Cabrit & André (1991) found the correlation between momentum flux of CO molecular outflows and the mass of the YSO envelope. This correlation was improved by Bontemps et al. (1996), demonstrating that there is a good continuity from Class 0 to Class I sources. These correlations of outflows and disks imply that outflow and in-fall occurred simultaneously or at least closely linked.

Outflows probably limit the mass of the star/disk system under formation and are indispensable for transporting away the excess angular momentum of accretion disks.

1.4 X-rays from YSOs

1.4.1 *Einstein* and *ROSAT* Observations

The *Einstein* Observatory was the first satellite to detect soft X-rays from low-mass YSOs. The *Einstein* observations discovered not only that a significant fraction of the previously known T Tauri stars ("classical" T Tauri Stars: CTTS) were strong X-ray emitters, but also that a new class of T Tauri Stars (TTSs), lacking the emission-line signatures of the CTTS. These stars, dubbed "weak-lined" TTS (or WTTS), outnumber the CTTS by large factors (generally 2 to 10). Subsequent observations in the infrared wavelength (near- to far-IR, i.e. > 2 μm to 100 μm), and in sub-mm ranges showed that a CTTS was surrounded by optically thick circumstellar disk (i.e. corresponding to a Class II in SED), while a WTTS was surrounded at most by optically thin disk, and the emission lines originate at the interface between the star and the disk, when present (i.e. corresponding to Class III in SED). The X-rays were found to have strong variabilities with occasional rapid flares – consistent with enhanced solar-type activities of magnetic fields produced by the dynamo mechanisms (Feigelson and DeCampli 1981, Montmerle et al. 1983). Then the X-rays were thought to be essentially solar-like, coming from magnetically confined plasma loops, at temperatures comparable to those seen on the Sun ($\sim$ 1 keV), but with larger luminosities than those of solar X-ray ($\sim 10^{27}$ erg s^{-1}) by 3–5 orders of magnitude. Since an outer layer of a TTS is entirely convective over large depth, magnetic fields were assumed to originate from the classical dynamo mechanism. (For reviews, see, e.g. Montmerle et al. 1993, Feigelson 1994.)

After the *Einstein* and post-*Einstein* observations, numerous *ROSAT* observations have been done, first in the course of the All-Sky Survey (RASS), then pointed at various molecular clouds and star-forming regions, or specific classes of young stars, like Herbig Ae/Be stars (more massive counterparts to TTSs). Through these observations, the sample of WTTSs increased remarkably. The increased YSO samples lead to statistical studies and the results are as follows;

(i) Observations of the Cha I cloud (Feigelson et al. 1993), the ρ Oph cloud (Casanova et al. 1995), or the IC346 young star cluster (Preibisch et al. 1995) show that X-ray luminosity of a TTS spans a large dynamic range from as low as 10^{28} erg s^{-1} to more than 4 orders of magnitude. The luminosity is correlated with

global stellar parameters, like bolometric luminosity or mass. In particular, the "saturation line" in X-ray luminosity (see Figure 1.4 and 1.5) is tightly correlated with bolometric luminosity or square of stellar radii, which implies quiescent X-rays come from a large number of mini flares on the stellar surfaces, and when the star is fully covered with flares, it appears as the saturation line.

(*ii*) Correlations between X-ray luminosity and stellar rotation have obtained. It holds not only to TTSs but more generally to cool stars. Stellar rotation is a key for dynamo process, then the results support that X-rays from TTSs are generated by dynamo mechanism. Adopting the correlation between L_X vs. $L_\odot$, the faster rotation of stars lead to larger X-ray active region on the stars.

(*iii*) Correlations of both X-ray luminosity and surface flux with stellar age have been found (Neuhäuser et al. 1995).

(*iv*) No large difference of X-ray properties between CTTS and WTTS (Feigelson et al. 1994, Casanova et al. 1995, Preibisch et al. 1995) is found, except the interstellar extinction (large-scale RASS observations of Taurus, Neuhäuser et al. 1995). This suggests that circumstellar matter plays no essential role for the X-ray emission, hence X-rays are specific signature for an activity state of a central star.

Although, *Einstein* and *ROSAT* detected soft X-rays from many TTSs, only a few protostars were found to emit soft X-rays, because soft X-rays are easily absorbed by dense circumstellar materials around protostars; the reports of X-rays from Class I sources with *ROSAT* were given by Grosso et al. 1997; Neuhäuser & Preibisch 1997. Neither the *Einstein* satellite nor *ROSAT* detected X-rays from Class 0 sources, which have large circumstellar extinction, A_V up to 1000.

1.4.2 *Temma* and *Ginga* Observations

These satellites have no imaging capability, but have a wide spectral range (*Temma*: 2–10 keV, *Ginga*: 1–37 keV), which include the Iron K shell transition line (E$\sim$ 6.7 keV). Therefore they were powerful to determine the spectra of sources, and detected the X-rays from highly obscured regions. The obtained results are as follows:

(*i*) Thin thermal emissions with high temperatures ($\sim$ 2–5 keV) were discovered (Figure 1.6, 1.7).

(*ii*) Flare events in the hard X-ray band ($>$ 2 keV) were found (Figure 1.8,

1.9).

(*iii*) From the Iron K shell line ($E \sim 6.7$ keV), metal abundances of star forming regions were determined for the first time, which were less than cosmic abundance.

(*iv*) X-rays from dark cloud with high absorption of $N_H > 10^{22}$ H cm^{-2} were discovered (Koyama et al. 1987, 1992).

1.4.3 *ASCA* Observations and Unsolved Problems

Though these satellites gave many contributions to YSO study, they still had weak points. The soft X-ray imaging satellites *Einstein* and *ROSAT* had less sensitivity in hard X-ray band which can penetrate dense absorbing matters. Then they could hardly detect protostars in highly obscured regions. The hard X-ray spectroscopic satellites *Temma* and *GINGA* had no imaging capability, hence can hardly pinpoint to any infrared/optical counterpart, even if they detect highly absorbed X-rays. In these senses, *ASCA* has advantage by its high sensitivity from soft to hard (up to 10 keV) band, with a reasonable imaging capability and a high spectral resolution (see Chapter 2).

These capabilities have been already demonstrated by recent *ASCA* results in dense molecular cores. A group of Class I sources has been identified by *ASCA* in the "Coronet" IR cluster, located in the heavily obscured RCrA cloud (Koyama et al. 1996), with evidence for emission up to 10 keV. More mysteriously, the flare spectrum from this region shows a distinct double line at 6.16 and 6.85 keV, in the vicinity of 6.7 keV, where the Fe-K line normally provides a single signature when it comes from a plasma with $kT \simeq 1$ keV. This feature remains unexplained to date. In contrast, in a joint *ROSAT/ASCA* observation of the L1551 cloud, Carkner at al. (1995) detected no X-ray from the Class I source L1551-IRS5 which excites the famous CO outflow.

ASCA also enabled to analyze flares from YSOs very precisely. For example, Tsuboi et al. (1998) detected a large flare on active WTTS V773 Tau in the hard X-ray band (> 2 keV). From the time-sliced spectra, they found several new and interesting features including the highest temperature of 100 million K in the flare peak (Figure 1.10). This demonstrates that if we detect large flares from protostars, we can analyze the spectrum precisely as well as V773 Tau.

The early *ASCA* observations opened a new window for the YSO study. With

the *ASCA* observations on YSOs, we investigate the following unsolved problem.

- When does a star begin to emit X-rays ?

  Although X-rays from Class I protostars were detected (e.g. Koyama et al. 1996, Grosso et al. 1997), whether or not Class 0 protostars emit X-rays is open question. Due to the large amount of accreting gas and the deep location in molecular core, Class 0 objects could have extremely large absorption, up to $\sim 10^{24}$ H cm^{-2} or more. Therefore, with *hard* X-ray imaging by *ASCA*, we reveal this question.

- What is the X-ray emission mechanism ?

  In more evolved TTSs, it is well established that the X-rays are emitted by the stellar magnetic surface activity, independently of the existence of a circumstellar disk. However, at earlier stages, an origin of X-rays are not obvious. One idea is the same as that for TTSs, i.e. dynamo activity at an outer convection layer of the central star. The other possible idea would be the dynamo activity around boundary layer between the central star and inner disk. The difference in X-rays between protostars (Class 0, I) and the other phases of star formation (Class II, III) could be a clue to solve the origin.

- How is the structure and dynamics around a central star ?

  X-rays could be emitted from a close vicinity of a central star, while radio to infrared wavelengths originate from surrounding matters, and not from the central star itself. Hence, from X-ray activity of protostars, we reveal physics around a central star and its inner accretion disk.

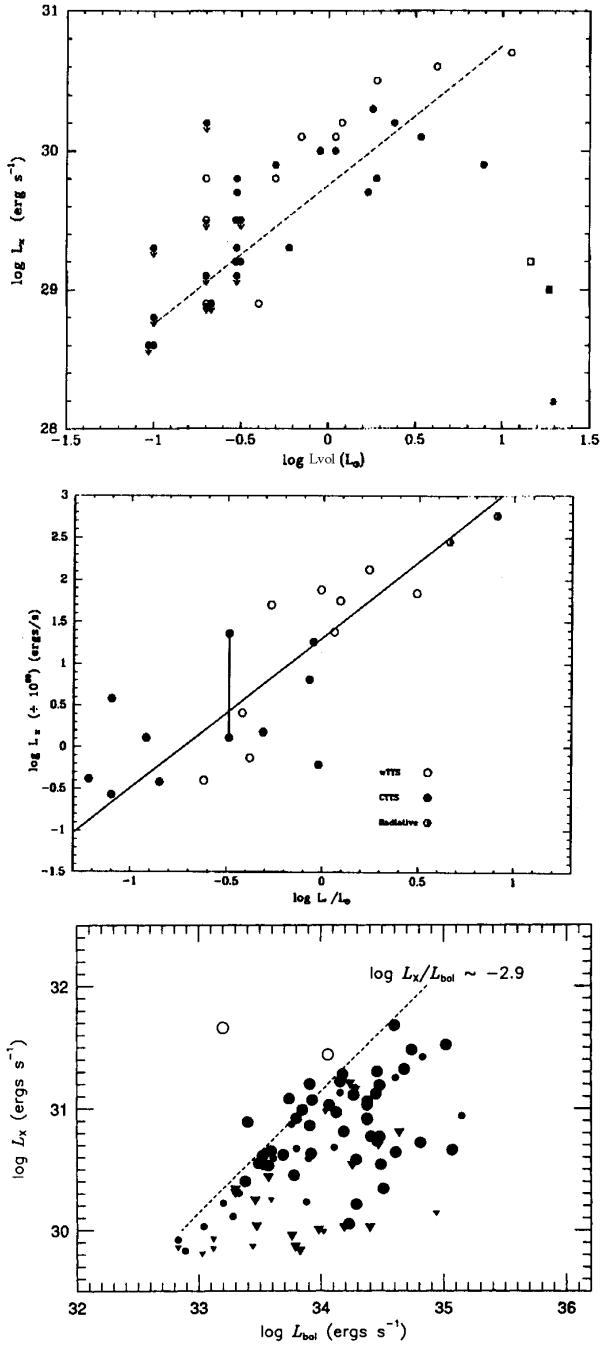

Figure 1.4: X-ray luminosity vs. bolometric luminosity for stars.
left: ChaI region (Feigelson et al. 1994). Filled (open) circles are CTT (WTT) stars, crosses are proposed new T Tauri stars, and squares are the two B9 stars.
center: L1495 region (Strom & Strom 1994). The line shows the best fit to the data.
right: Orion region (Gagné et al. 1995). Downward-pointing triangles indicate X-ray upper limits, smaller symbols indicate uncertain L_{bol} determinations, and open circles indicate that strong X-ray flares were detected on these stars. Most stars appear very close to or below the saturation line corresponding to log $(L_X/L_{bol}) \sim -2.9$.

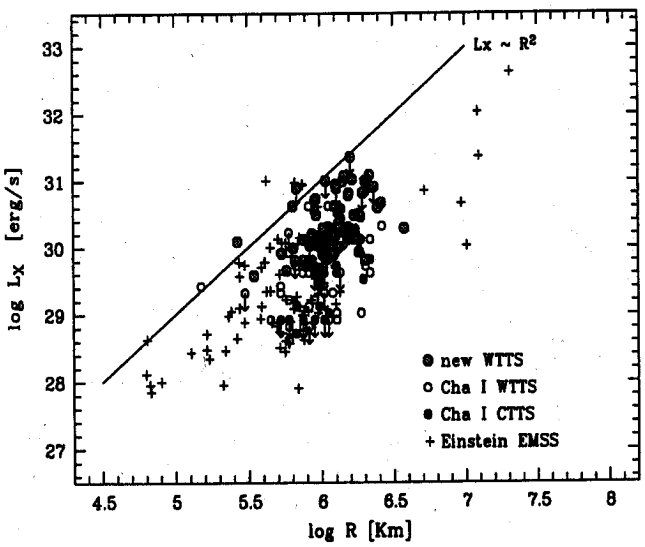

Figure 1.5: X-ray luminosity vs. stellar radii for YSOs. (Alcalá et al. 1997)

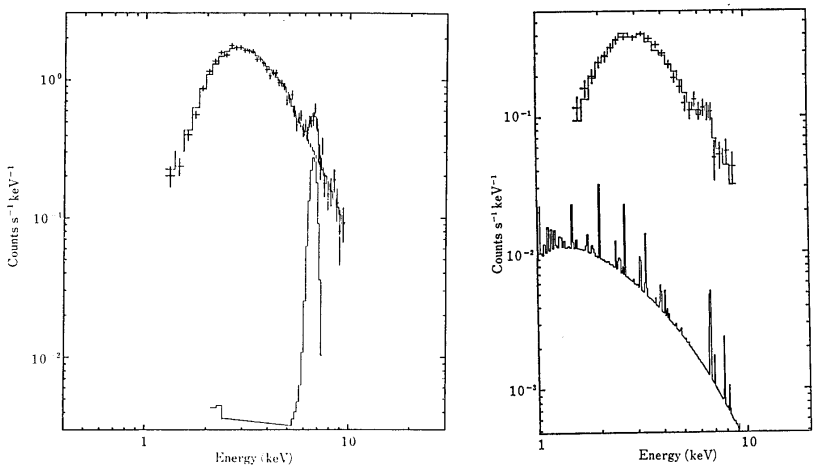

Figure 1.6: The spectrum of the Orion Nebula (Agrawal et al. 1986; left panel) and that of the Rho Oph cloud (Koyama 1987; right panel) obtained with the *Temma* satellite. The solid lines show the best-fit thin thermal plasma models.

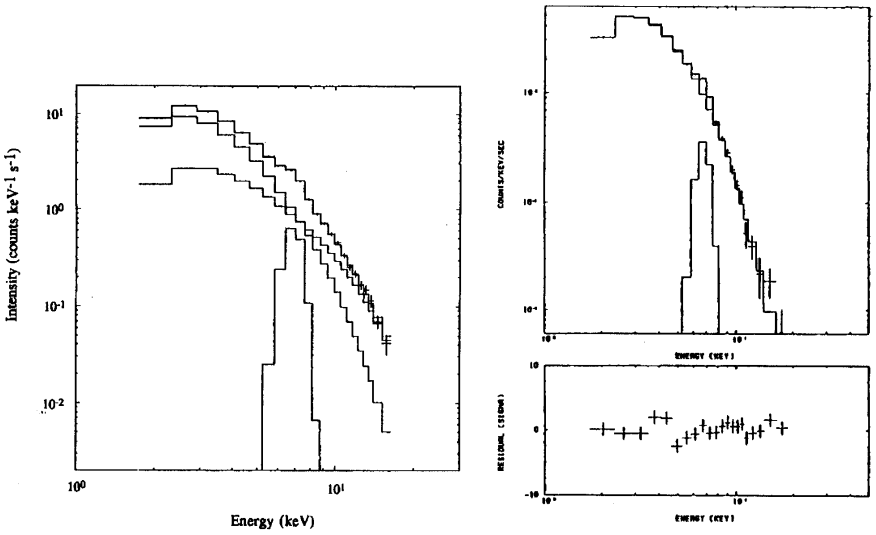

Figure 1.7: The spectrum of the Orion Nebula (Yamauchi & Koyama 1993; left panel) and that of the Rho Oph cloud (Koyama et al. 1992; right panel) obtained with the *Temma* satellite. The solid lines show the best-fit thin thermal plasma models.

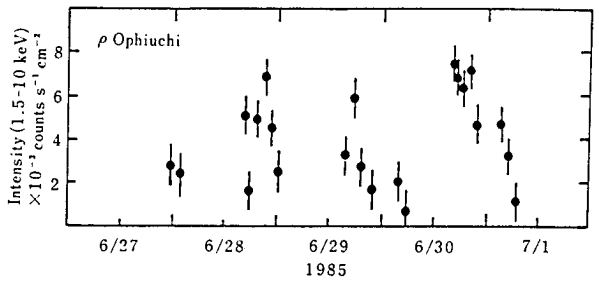

Figure 1.8: The light curve of the Rho Oph cloud obtained with the *Temma* satellite (Koyama 1987).

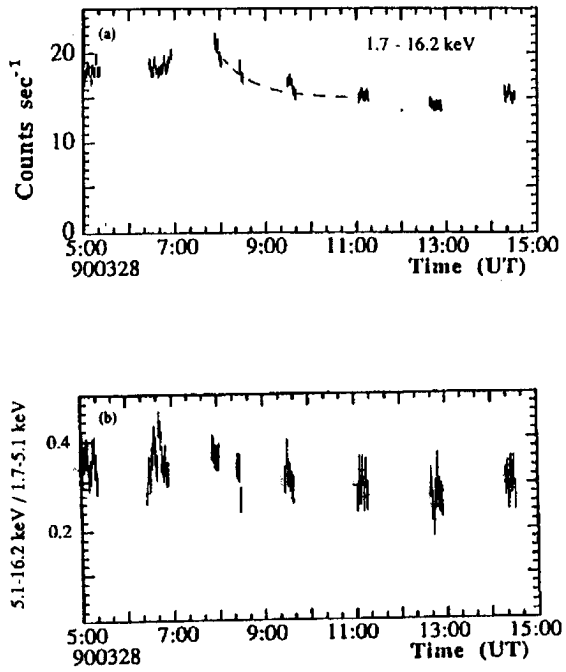

Figure 1.9: The light curve of the Rho Oph cloud in the 1.7–16.2 keV band obtained with The *Ginga* satellite (Koyama et al. 1992). Lower panel shows the hardness ratio (flux ratio of the 5.1–16.2 keV band to the 1.7–5.1 keV band).

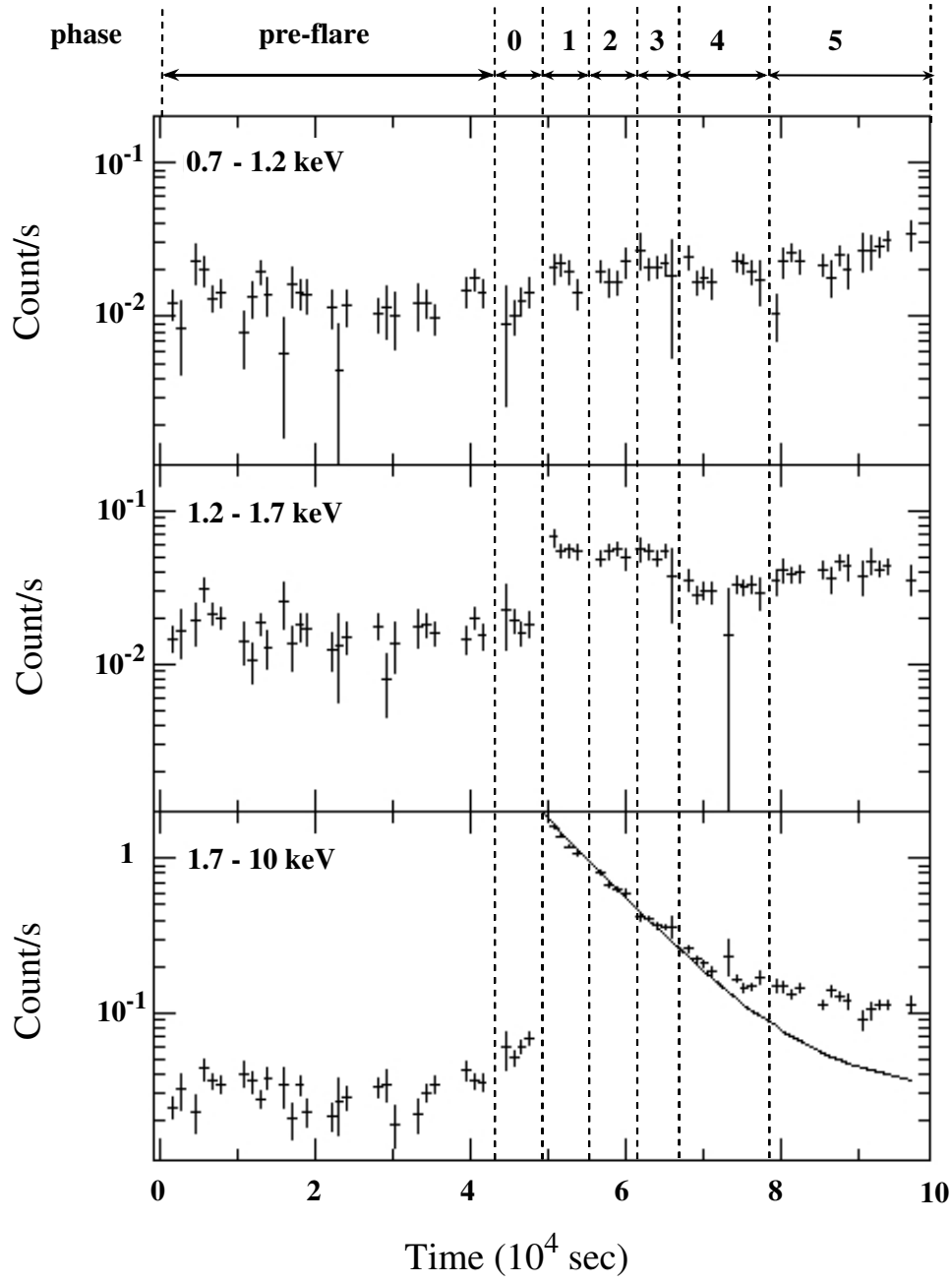

Figure 1.10: X-ray light curves of V773 Tau obtained with *ASCA* (Tsuboi et al. 1998)

Chapter 2

Instrument

In this chapter, we report on the *ASCA* satellite and the instruments onboard *ASCA*.

2.1 *ASCA*

ASCA is the 4th Japanese X-ray satellite launched on 20 February 1993, by the M–3SII–7 rocket from Kagoshima Space Center(KSC)(Tanaka et al. 1994). The satellite orbit is semi-circular with the perigee of 520 km and the apogee of 620 km. It weights 417 kg and is 4.7 m long along the telescope axis and 3.5 m wide across the solar paddles. Figure 2.1 shows the schematic view of *ASCA* in orbit.

ASCA can contact KSC only for about 10 minutes each in 5 (or 6) consecutive orbits out of the 15. These orbits are usually called "contact orbits", and the other ten "remote orbits". During the remote orbits, *ASCA* can send (down-

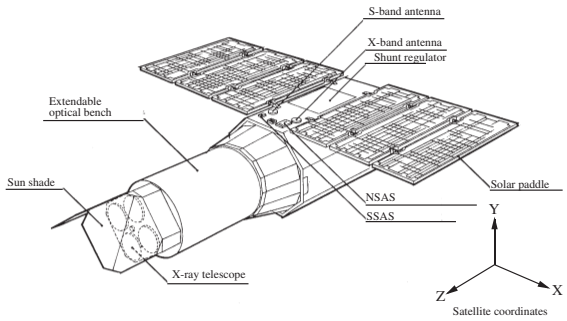

Figure 2.1: The schematic view of the *ASCA* satellite.

link) the stored data to the NASA DSN stations of Madrid, Canberra, Goldstone, Wallapse and San Diego. These down-link operations are pre-programmed in the KSC contact pass.

ASCA carries four identical X-ray telescopes (XRT: Serlemitsos et al. 1995) of 3.5 m focal length, which are equipped with four imaging spectroscopic detectors; two Gas Imaging Spectrometers (GIS: Ohashi et al. 1996; Makishima et al. 1996) and two Solid state Imaging Spectrometers (SIS: Burke et al. 1994).

The satellite attitude is controlled in three-axis with the stability of better than $10''$ and absolute pointing accuracy about $\simeq 30''$. To achieve them, *ASCA* is equipped with 4 gyros with an additional back-up, four reaction wheels, two CCD star cameras and 3 magnetic torquers, each with control electronics. The satellite attitude is limited to keep the direction of the solar paddle within 30° from the sun. The maneuver is performed by changing the angular momentum balance among the reaction wheels with the slew rate of $\simeq 0^\circ.2\ \mathrm{s}^{-1}$.

As the telemeter channel, *ASCA* uses X-band (down-link at KSC, 8.5 GHz) and S-band (up-link 2.1 GHz, down-link 2.3 GHz). The orbital elements are measured twice a day. The data from the detectors and on-board instruments are compiled by the data processor (DP), then stored in the bubble data recorder (BDR) of 134 Mbits capacity. The telemeter has three bit-rates, HIGH of 32 Kbits s^{-1}, MEDIUM of 4 Kbits s^{-1} and LOW of 1 Kbits s^{-1}; thus the recording time is 68, 545 and 2185 minutes, respectively. HIGH-bit-rate is mainly used in the contact orbits, and MEDIUM-bit-rate is in the remote orbits. LOW-bit-rate is used to save the BDR capacity in case that the detectors cannot observe the target, i.e., the satellite is in the South Atlantic Anomaly (SAA) or the target is behind the earth.

2.1.1 XRT

ASCA has four identical conical foil X-ray mirrors which are weight saved versions of similar mirrors flown earlier on the Broad Band X-Ray Telescope experiment (*BBXRT*) aboard Astro-1, which was one of the space shuttle mission developed by NASA. Since X-ray photons above a few keV are reflected only in a grazing incident angle, or the light pass is almost parallel to the mirror surface, the effective area of the X-ray reflector is largely limited; see in the case of paraboloid (Figure 2.2a), for example. To gain reflection area and to compensate aberrations,

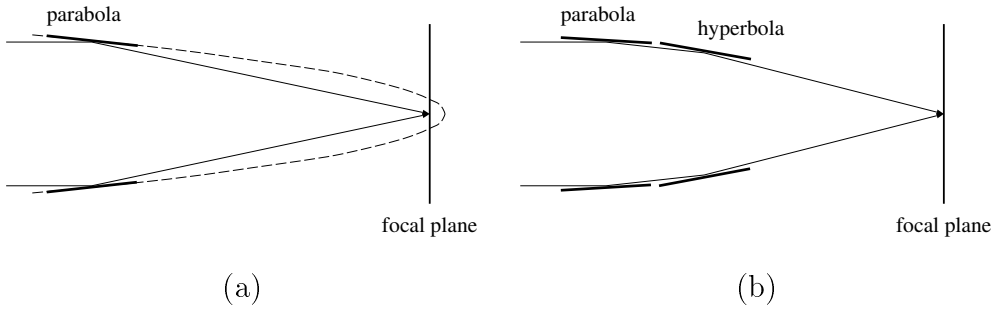

(a) (b)

Figure 2.2: The schematic figure of the X-ray telescope. (a) The primitive model. (b) Wolter type I geometry, which is used in *ASCA* XRT.

the X-ray mirror consists of multi-nesting tandem with aligned and co-focusing paraboloids and hyperboloids (Wolter type I geometry; Figure 2.2b). The *ASCA* XRT approximates this concept with a flat conical surfaces instead the parabolic and hyperbolic surface. This simplification is crucially practical, allowing us to construct the multiple-nesting of 119 thin foils for one XRT. Nearly flat pieces of the aluminum foil of 125μm thickness are first shaped into flexible conical segments having approximately the required curvature, then dipped in an acrylic bath to smooth the surface, deposited a $\sim$ 500 Å gold layer to increase X-ray reflectivity, then finally placed into a housing, constrained by supporting lags to fit the X-ray optics. One XRT with 119 foils aligned by $\sim$ 1 mm pitch has a 558 cm^2 effective area, more than 50% of the geometric open area. A trade-off of this large effective area by the thin foil mirrors is found in less spatial resolution than the ideal Wolter type 1 optics. The half-power diameter of XRT is about 3 arcmin. Table 2.1 gives the design parameters of XRT.

To maintain the best-performance of the mirror in orbit (i.e., to keep the reflecting surfaces free from contaminations and to minimize the mirror deformation by thermal stress), heaters and thin (0.22 and 0.54μm for the SIS and GIS, respectively) aluminized mylar covers were placed near and on the entire mirror aperture. Since X-ray reflectivity depends on the grazing angle and photon energy, the efficiency and point spread function (PSF) of XRT also depend on the source position and energy. The efficiency and PSF are calibrated on ground in several points (in energy, mirror position, and incident angle), but overall features are simulated with the ray-tracing with appropriate optical constant (complex refractive index) of the mirror foils, including the real XRT structures. The final response is supplied by the *ASCA* team with fine tunings to fit the standard sources: Crab for spectrum

Table 2.1: XRT design and performance parameters.

Design Parameters	
Mirror Substrate	0.125 mm aluminum foil
Surface	10μm Acrylic Lacquer + 500 ÅAu
Number of Nested Cones	120 (back-to-back layers)
Outer/Inner Diameter	345/120 mm
Focal Length	3500 mm
Grazing Angle Range	0.24–0.70 deg.
Geometric Area	558 cm^2 (each)
Field of View	24/16 arcmin (@1/7 keV)
Number of Telescopes	4
Mirror Weight	10 kg (each)
Performance Parameters	
Effective Area	$\simeq$ 300/$\simeq$ 150 cm^2@1.5/7 keV (each)
Size of Blur (Encircled Energy)	$\simeq$ 3 arcmin Half Power Diameter (no energy dependence)
Reflector Surface Roughness	$\simeq$ 3 Å

and Cyg X-1 for imaging. Figure 2.3 shows the energy dependence of the XRT effective area. The values used to plot the graph is an integrated flux within the 6 arcmin radius circular area from the image center.

The effective area decreases rapidly as the off-axis angle increases. At higher incident energy, since the grazing angle should be smaller, only inner foils remain effective. Accordingly, effective area decreases as incident photon energy increases. Figure 2.4 shows the effective area for each off-axis angle as a function of energy.

Possible residual deformation of the foils worsens the angular resolution. While the half power diameter (HPD) of XRT is expected to be about 0.3 arcmin in the ideal case, the real value is about 3 arcmin. Figure 2.5 shows the radial profile of the PSF. It can be approximated as a Gaussian in the central core of ($r < 1'$), followed by an exponential function outside. The quadrant mirror structure make the PSF to be the Maltese-cross shape (Figure 2.6). As the off-axis angle increases, the PSF is largely distorted. For the evaluation of the contamination of a bright source to the surrounding regions, the encircled energy function (EEF) which is defined as the ratio of photons flux in a circle with given radius from a

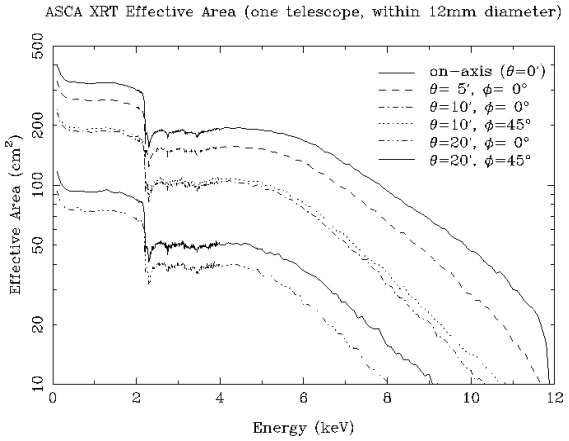

Figure 2.3: The energy dependence of the XRT effective area on-board *ASCA*.

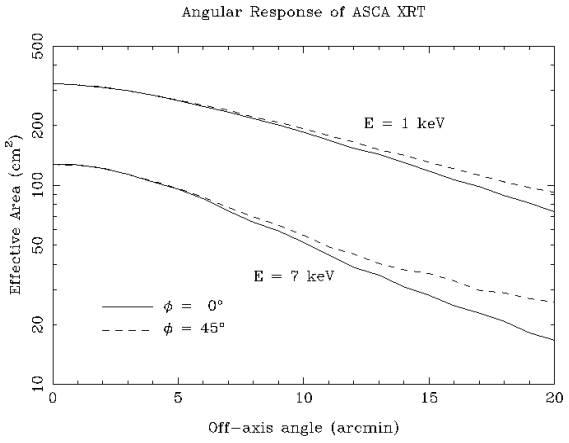

Figure 2.4: The off-axis angle dependence of the XRT effective area on-board *ASCA*.

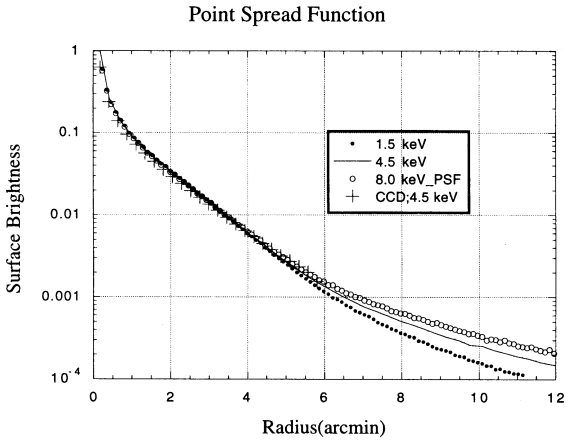

Figure 2.5: The point spread function of the *ASCA* XRT.

point source is useful. Figure 2.7 shows the EEF for different energies. It shows that about 80% of the flux drops within the circle of a 6 arcmin diameter. The difference of the encircled fraction between high and low energy become large as the increasing angular radius. Therefore, the apparent spectrum becomes harder as the accumulation radius increases.

Another practical problem of the XRT is stray lights from outside of the field of view (FOV). The XRT geometry does not allow photons reaching the focal plane without being intercepted by the foils; however, the photons scattered due to the surface roughness, single or more than 3 reflection, or back-side reflected photons may come in the focal plane. We call these photons as the stray light. Figure 2.8 shows the image of the stray light when the Crab nebula is 1° offset from the detector center. The stray light, if strong source is nearby, is crucial for a weak source or extended emission, like the cosmic X-ray background (CXB).

2.1.2 GIS

The GIS (Gas Imaging Spectrometer), which has been developed mainly by University of Tokyo, ISAS and Meisei Electric Co., Ltd., consists of two imaging scintillation proportional counters (GIS2 and 3) and a signal processing part (GIS-E). Also the radiation belt monitor (RBM) is equipped.

Compared with the SIS (see next subsection), the GIS has larger efficiency (by a factor of 2 at 7 keV) at high energy, higher temporal resolution, larger dynamic range in the source intensity and a four-times wider FOV ,however, it has a lower soft X-ray efficiency, a somewhat worse position resolution and poorer

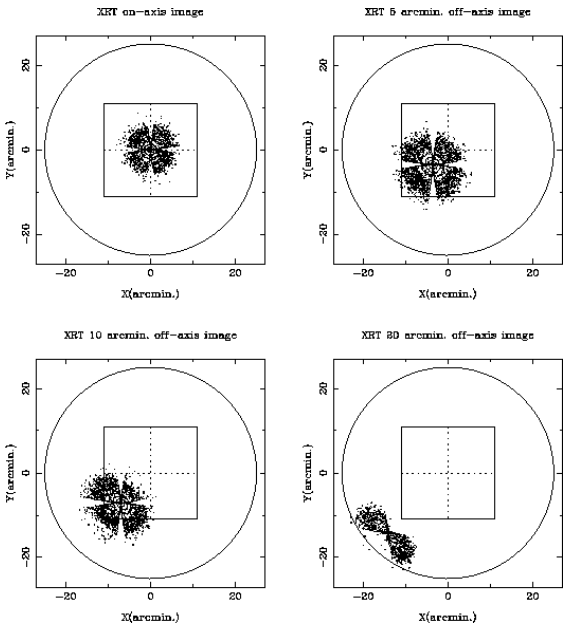

Figure 2.6: Point spread function of the *ASCA* XRT for four different off-axis angles. Approximate field of view is shown for GIS (circle) and SIS (square).

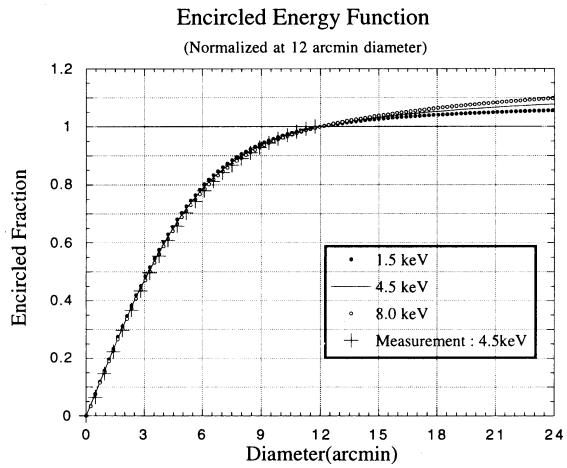

Figure 2.7: The encircled energy function of the XRT.

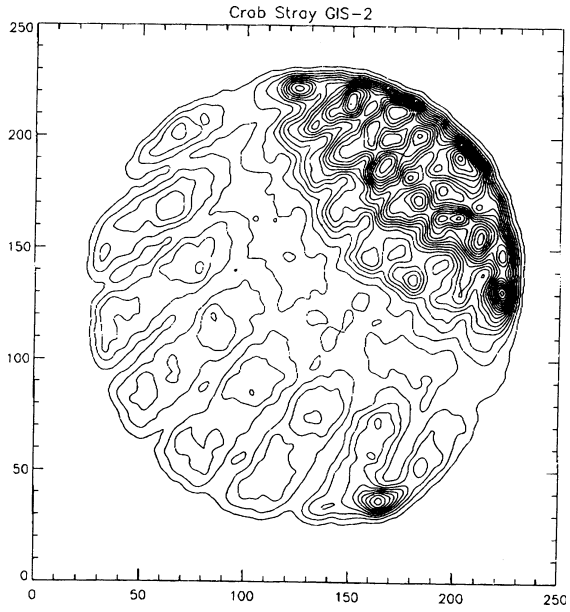

Figure 2.8: The stray light image of the Crab nebula at 1° offset from the detector center.

energy resolution by a factor 2–4 than those of SIS.

Each GIS-S consists of a gas cell, a position-sensitive photo-tube and high-voltage suppliers. Figure 2.9 shows the cross section of the GIS-S. The X-rays from the XRT are detected by the 25 mm-depth gas cell, which is filled with 96% of Xe and 4% of He to 1.20 atm pressure (at 0°C). The gas is sealed by a beryllium foil of a 10μm thickness and a 52 mm diameter, supported by a stainless grid and fine mesh. The gas cell is divided into two, the drift region just inside the Be window and the following scintillation region. Each region is biased by 1 kV cm^{-1} and 4 kV cm^{-1} electric fields. To intercept the non-X-ray backgrounds, the GIS has a hood coated by a 0.2–0.5 mm thickness tin foil and partially by a 0.1 mm thickness molybdenum foil.

The X-ray photon is photo-absorbed in the drift region and creates free electrons. The electrons drift into the scintillation region guided by the bias field, then accelerated by the stronger field. Xe atoms are excited by the electrons, then emit UV photons of wavelength of $\simeq$ 170 nm. This excitation and relaxation processes occur as the electrons pass the scintillation region in 2–3μs; thus, makes a scintillating light column. The number of UV photons becomes $\simeq 1.5 \times 10^5$ for a 6 keV X-ray photon. Since these process are not accompanied by the secondary-electron multiplication, the energy resolution is kept 2-3 times better than the proportional

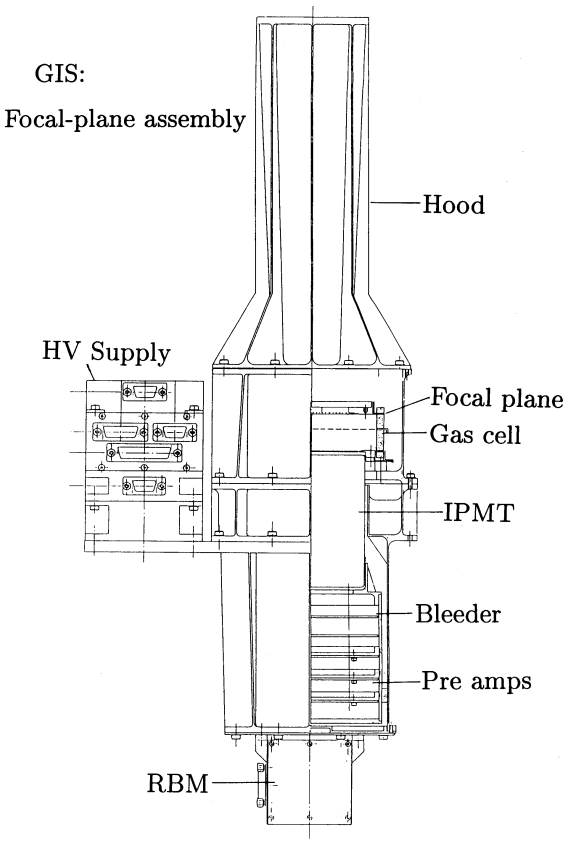

Figure 2.9: The cross section of the GIS-S.

counter. The scintillation UV photons are detected by a position-sensitive photo-tube set below the gas cell.

The energy information is obtained from the final dinode signal. The energy resolution is about 8.0% (FWHM) at 5.9 keV, which scales as inverse square root of the energy. X and Y positions of a detected photon are calculated using outputs from 32 (16 for X and 16 for Y) multi-wire anodes. The position resolution is about 0.5 mm (FWHM), which corresponds to about 30 arcsec, at 5.9 keV, and scales as inverse square root of the energy. The signals from the photo-tube are processed by GIS-E.

To eliminate non-X-ray backgrounds, only signals with the pulse shape (rise time) of the limited band are transferred to the on-board CPU. With this process, about 90% of backgrounds within the 2–10 keV band are eliminated. In addition, on-board CPU eliminates the event of which position is outer than the certain radius or the spatial distribution of multi-anode output is larger than the certain length. This discrimination method is called SPRD. Without SPRD, it is known that the strong source near the edge of the GIS, such as the calibration source, makes a ghost image at the inner area if the event position is determined with the Fast Lorentzian Fitting, used for the usual data processing. With these discriminations, 99% of the non-X-ray background is eliminated and the residual non-X-ray background in the 17 arcmin radius is 5×10^{-4} counts s^{-1} cm^{-2} keV^{-1} in the 2–10 keV band.

Since the telemetry capacity is limited, the GIS has four different telemetry modes:

PH (Pulse Height) For nominal observations, this mode is usually used. One event consists of the pulse-height, position, rise-time, event-spread and timing information packed to 31 bits. The commandable bit-share are 10, 8, 5, 8 and 10 bits in normal operation. In this mode, all the data are processed by on-board CPU.

PH PCAL (Position Calibration) This mode is prepared for the calibration of the position calculation done by on-board CPU. All information including 32 anode signals is transmitted. Thus the maximum source intensity and the temporal resolution are reduced much from the PH-mode. PCAL data, however, can be processed on ground in a failure mode of on-board CPU.

Table 2.2: The temporal resolutions and the maximum source intensities of the GIS.

mode	Bit rate	Temporal resolution Timing bits 0 bit	Timing bits 10 bits	Maximum Source Intensity [count s^{-1}]
PH	H	62.5 ms	61μs	256
	M	500 ms	488μs	32
	L	2 s	1.95 ms	8
PCAL	H	31.25 ms		32
	M	250 ms		4
	L	1 s		1
MPC	H	0.5 s	1.95 ms	128 Crab†
	M	4 s	15.6 ms	16 Crab
	L	16 s	62.5 ms	4 Crab

†: 1 mCrab $\sim$ 1 event s^{-1}

MPC (Multi-channel Pulse Count) This mode transmits only the pulse-height and timing information. The pulse-height converted data are accumulated in on-board memory in DP. The maximum number of spectral bin is 256, which can be reduced to increase time resolution. This mode can be used for an extremely strong source or in a failure made of on-board CPU.

Memory Check This mode dumps the RAM image (32 KB$\times$2) of on-board CPU. Usually, this mode is carried out once a day during the KSC contact to check whether on-board memory is correct or not.

Table 2.2 gives the temporal resolution and maximum source intensity of the GIS in each telemetry mode.

The gain of the GIS differs from position to position, hence the gain calibration by pointing Cas A in various positions has been performed. In addition, the gain changes with the pressure and the impurity of the counter gas and the photo-tube temperature. To correct these effects, the gain of the GIS is monitored by ^{55}Fe isotopes at the edges of the entrance windows of the each gas cell. These calibration data are accumulated by the *ASCA* team and distributed to the end users.

Figure 2.10 shows the effective area with the combination of XRT and GIS.

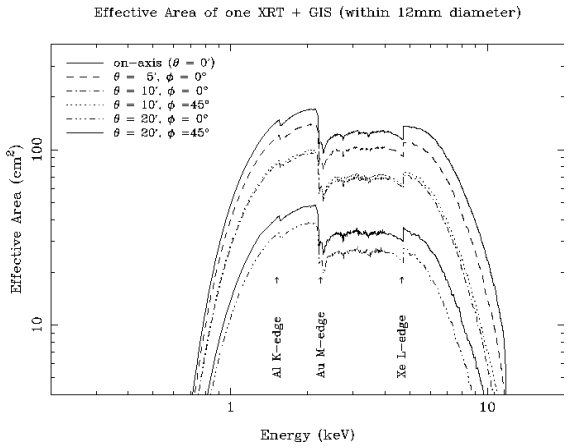

Figure 2.10: The effective area with the combination of XRT and GIS.

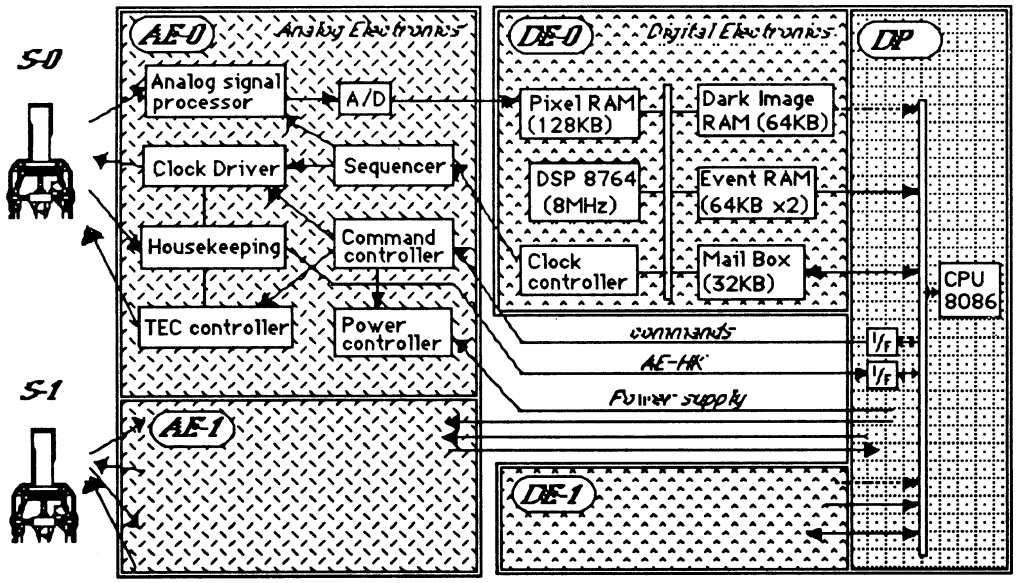

Figure 2.11: The signal block diagram of SIS.

2.1.3 SIS

The SIS (Solid state Imaging Spectrometer) consists of three components — two cameras (SIS0 and SIS1), each with four CCD chips, the analog electronics (SIS-AE) and the digital electronics (SIS-DE). SIS-DE is equipped in the DP body. The DP also has responsibility of a part of the SIS data processing. Figure 2.11 shows the signal block diagram of the SIS subsystem.

The CCD detector can be regarded as a cluster of solid state detectors (SSD) with a large number of square-aligned microscopic ($27 \times 27 \mu\mathrm{m}^2$ in case of SIS) electrodes called 'pixels'. The electron cloud induced by the X-ray photon are absorbed by the nearest pixels, then are carried by the driving external clock from

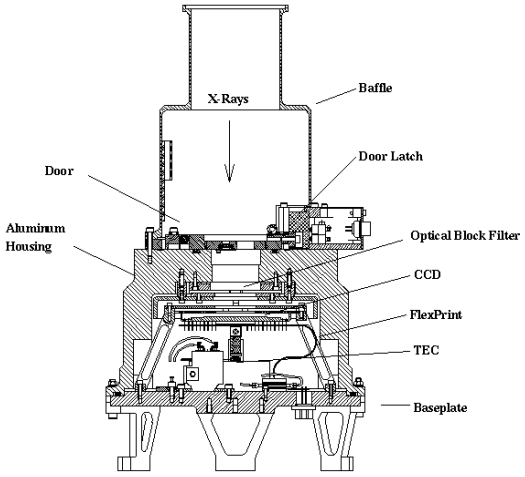

Figure 2.12: The cross section of the SIS camera.

pixel to pixel to the readout gate.

Since the charge is thus transferred from pixel to pixel, which have very small electric capacitance, the floating electric capacitance at the readout gate also very small. This extremely small capacitance makes a higher readout voltage than normal SSD, hence the readout noise can be very small. On the other hand, the temporal resolution is much lower than the normal single detector such as GIS, because the charges are read sequentially. In the case of SIS, the readout cycle of one chip is 4, 8 or 16 sec in 1-, 2- or 4-CCD-mode, respectively.

Figure 2.12 shows the cross section of the SIS camera, and Figure 2.13 shows the chip configuration of the SIS. In the normal operation, the CCD chip is cooled down to about $-60°$C by a Peltier device (TEC, thermal electric cooler) to reduce the dark current. The TEC dissipates the heat into the housing, which is cooled to -30–$40°$C with the radiator coupled to the heat pipe. The chip in the housing is covered by a multi-layer insulator and supported by Lexan columns in order to reduce the heat inflow. In front of the chip, a Lexan film of a 1000Å thickness coated with aluminum of a 400Å thickness at each side is placed to cut off the optical light.

The SIS-AE generates the chip driving clock, controls the TEC and converts the video signal from the SIS-S to the digital data (PH data). In contrast to GIS, SIS has no hardwired logic.

The SIS-DE receives the PH data from the SIS-AE and extracts the X-ray

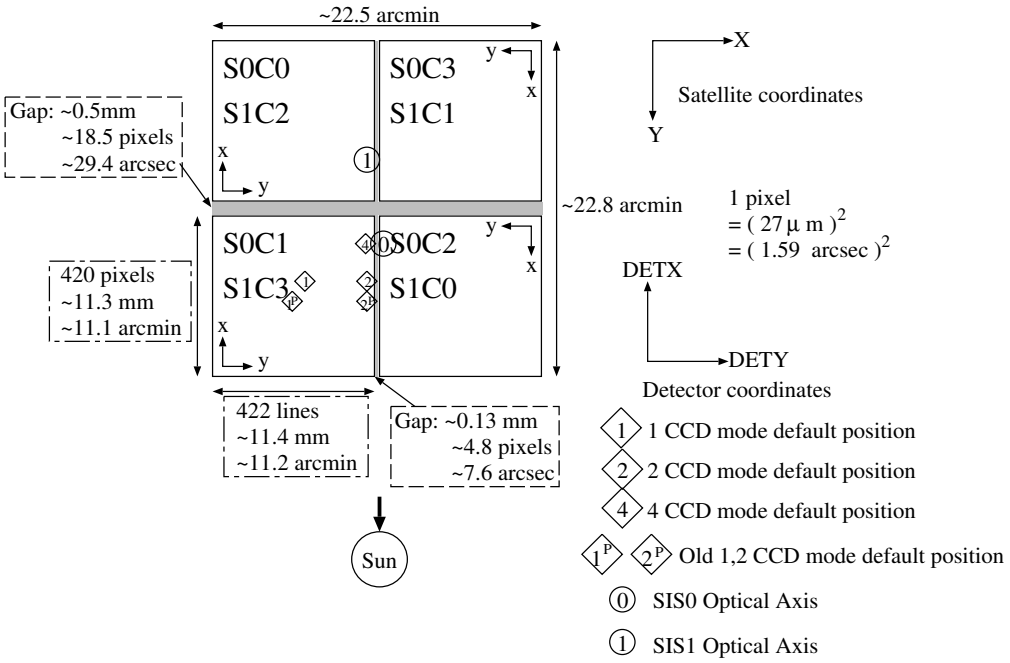

Figure 2.13: The chip configuration of the SIS.

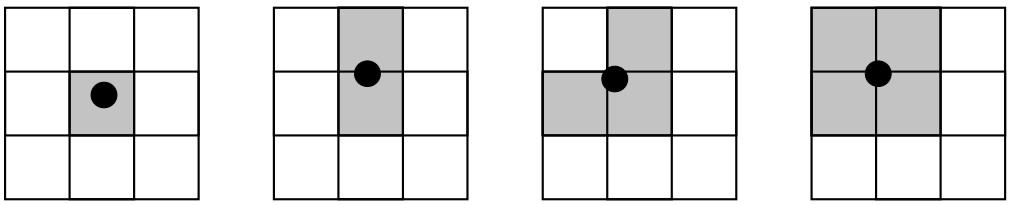

Figure 2.14: The X-ray event pattern of the CCD detector.

events. The X-ray photon of a 10 keV energy induces a primary electron cloud of a 1μm size by the photo-absorption process, with the size scaling as $E^{1.75}$ (Janesick et al. 1985). After drifting to the electrode of each pixel, the size is grown to be $\sim 5\mu$m. Since this size still smaller than the that of pixel, the electron cloud does not separate into larger than four pixels (Figure 2.14). On the other hand, charged particle events leave long tracks (long cloud). Using this difference of the cloud size, SIS-DE can eliminate the non-X-ray backgrounds. The energy of the X-ray event is calculated from 3×3 pixels around the local maximum pulse height pixel.

The dark current level consists of 'Dark level' and 'Bias level'. To save the on-board memory, the Dark level is taken from the average of the pixel group, which is typically in a $\frac{1}{16} \times \frac{1}{16}$ (default value) frame. This dark level is further time

averaged and is updated using the event-free pixel levels as:

$$\text{NewDarkLevel} = \text{OldDarkLevel} + \frac{\text{MeanPixelLevel}}{n} + 1, \tag{2.1}$$

where $n+1$ is the history parameter and set as 1, 4, 8 or 16 on command. The set of Dark level is called the dark frame. The Bias level is the DC offset of the dark current level. This is obtained from the PH data of the over-clock region, where there is no real electrode but only the driving clock is operated to these virtual pixels. Since the Dark level and the Bias level are the mean value in the grouped pixels, their possible variation within the group degrade the energy resolution essentially taken from multiple pixels. To take account or compensate this degradation, two approaches are currently used: (i) make the up-to-date response matrix including the long-term change of the resolution. This method can be applied for all the data, but needs the long term trend for pixel by pixel, which require a lot of work, hence has only been at a limited region. (ii) Since the dark level of each pixel is found to be rather constant in a short time scale (a few days), we can obtain the pixel-by-pixel dark template for the short time scale, by observing the night earth with the FRAME-mode or accumulating the event-free corner pixels of the FAINT-mode data (see below). With this template, we can adjust the pulse height on the ground. This method can be applied for the FAINT-mode data and the grade-0 BRIGHT-mode data.

The SIS has three observation modes (FAINT, BRIGHT and FAST) and four diagnostic modes (FRAME, DARK FRAME, HISTOGRAM and INTEGRATION):

FAINT The event information consists of the CCD ID, the addresses and 12 bit pulse heights of nine pixels. The size of each event is 16 bytes including the CCD ID. This mode can be used only for faint sources, but all the pulse heights relating with the event are obtained.

BRIGHT The pulse heights of 9 pixels are summed, and the summed PH data and the Grade information are transmitted. Table 2.3 gives the definition of the Grades. The event data has 4 bytes and consists of the Grade, addresses and the summed pulse height, which consists of 11 bit; the original 1024–2047 channels are binned by a factor of two and 2048–4095 by a factor of four.

FAST In this mode, the chip is driven to project all the charge onto one-dimensional array. Thus the spatial information is reduced to one dimension, but the

Table 2.3: The grade definitions of the BRIGHT-mode SIS events.

grade	name	split pattern
0	single	center
1	single+	center (+ detouched corner(s))
2	vertical split	center + top or bottom (+ detouched corner(s))
3	left split	center + left (+ detouched corner(s))
4	right split	center + right (+ detouched corner(s))
5	single-sided+ (+ detouched corner(s))	single-sided split + touched corner pixel(s)
6	L or square	L or square split (+ detouched corner(s))
7	Others	all others

scan period of a frame becomes faster than other modes. The event data has 2 bytes and consists of the Grade, the one-dimensional addresses and the pulse height with the same binning as that of the BRIGHT-mode. This mode is used for bright point sources of which each chip may be recorded by more than one X-ray photon event within the accumulation time of the other modes.

FRAME This mode sends the pulse heights of all pixels with 12 bit resolution.

DARK FRAME This mode sends a map of dark frame to ground with 8 bit resolution.

HISTOGRAM This mode makes the histogram of pulse heights of 4096 bins for all pixels and send to ground.

INTEGRATION This mode integrates the events in the chip for 160 s, read the resultant pulse heights and send them to ground with 12 bit resolution.

The SIS has three clocking mode for observation and FRAME-modes — 1, 2 and 4 CCD-modes. The exposure time for each clocking mode is 4, 8 and 16 s, respectively. Table 2.4 gives the summary of three observation modes.

As the SIS has no radio isotope, the relative gain between each chip was determined with the strong Fe-K emission line of supernova remnant W49B. It was pointed by all chips and the gains were determined within 0.5% errors. The absolute energy scale was determined with the strongest internal background emission

Table 2.4: Observation modes of the SIS.

	Faint	Bright	Fast
Temporal resolution†	4/8/16 s	4/8/16 s	16 ms
Maximum event rate‡	128/16/4	512/64/16	1024/128/32
PHA bits	12	11	11
Spatial bits	9×9	9×9	1 (and 3 timing bits)
Number of grade	—	8	2

†: In 1/2/4 CCD mode for Faint and Bright.

‡: In bit High/Med/Low. The unit is [events/s/2sensors].

line, Ni, which originate in the Kovar (an Fe-Ni alloy) frame-store shield.

In the charge transfer from pixel to pixel, a small fraction of the charge are lost with a rate called the charge transfer inefficiency (CTI). The CTI is periodically calibrated by pointing Cas-A at the each corner of chips. The calibration data are accumulated by the *ASCA* team and released to the end user.

Within the limited telemetry capability, we optimize the data acquisition by changing the event threshold and discrimination levels for the three items: the Level, Grade and Area discriminations.

The event threshold is a fundamental parameter of the on-board processing, and can be changed only by the agreement of the SIS team. After the initial check during the early part of the PV phase, the event threshold was set at 100 ADU for all chips until 1995 Dec 23, then after, the event threshold has been set to different ADU values for different chips such that they all correspond to the energy of 0.4 keV.

Level discrimination, when activated, plays a similar role (all events whose central pixel is below the threshold are discarded during on-board processing).

BRIGHT-mode has the eight grades (0-7), which are extensions of four basic groups: S (single), P (single-sided split; subdivided into Vertical, Left and Rights), L (L-shaped) and Q (square-shaped). The extensions arise because of the existence, in some events, of corner pixels which do not belong to the block since they touch the distributions only at the corners (so-called 'detached' corners). Usually, charges produced by an X-ray photon (less than, say, 5 keV) are split into 1 or 2 pixels, i.e., S events (grades 0-1) and P events (grades 2-5). However, grade-1 events, which consist of single events with one or more detached corners, should

be ignored because most are particle events (it is hard for an X-ray event to split the charges into diagonal two pixels). A sizable fraction of higher energy X-rays (5-10 keV), which tend to be absorbed deeper in the CCDs, are detected as L or Q (grade-6) events, while grade 7 events are dominated by particle events. Since each pixel included in the final PHA calculation contributes its own read-out-noise, grade 0 events have the best resolution and grade 6 the worst. The SIS team has concentrated on a combination of grades 0, 2, 3 and 4; this combination is therefore the best-calibrated. In particular cases, however, it may be better to add grade 6 events (to increase signal-to-noise at high energies) or to use only grade 0 events.

The CCDs that make up the SIS detector system are also sensitive to optical light. Since optical photons create an electron-hole pair, a large number of optical photons may raise the dark level. We found that parts of SIS0 Chip 2 and Chip 3 suffer from the 'light leakage': when the line of sight is close to the bright Earth, these regions produce many spurious 'detections', due to the optical lights entering SIS0 near these regions. They have effects similar to the flickering pixels, although the physical origins are different.

Chapter 3

Observations

3.1 Protostar Sampling

With *ASCA*, we executed X-ray survey of protostar candidates. As catalogs of protostars, we used four samples which Carkner et al. (1998) used: low temperature IR sources in five nearby star forming regions compiled by Chen et al. (1995, 1997), Herbig-Haro outflow sources from Reipurth (1994), CO outflow sources from Fukui et al. (1993) and the list of Class 0 objects from Bachiller (1996). In addition to the samples, in the ρ Oph region, we used samples of Class I candidates from Motte et al. (1998), and in the Orion Molecular Cloud 2–3, we used samples from Lis et al. (1998). For the classification, we rely on the bolometric temperatures obtained by Chen et al. (1995, 1997). We assumed that Class I sources typically have $70 < T_{bol} < 650$ K and Class 0 sources have $T_{bol} < 70$ K.

3.2 Observed Field

We list the observed fields in Table 3.1. All the fields are nearby dark clouds of distances less than about 500 pc.

3.3 Observation Mode

All the observations were executed with SIS 0, SIS 1, GIS 2, and GIS 3, hence four independent data-sets were provided. The data were filtered as following subsections. The net observing time for each detector is listed in Table 3.3.

3.3.1 GIS

Each of the GIS was operated in the Pulse Height mode with the standard bit assignment that provides time resolutions of 62.5 ms and 0.5 s for high and medium bit rates, respectively. The data were post-processed to correct for the spatial gain non-linearity. Data taken at geomagnetic rigidities lower than 6 GV and during passage through the South Atlantic Anomaly were rejected. We also rejected the data at elevation angles less than the value listed in Table 3.3.

3.3.2 SIS

Each of the SIS was operated in the mode as listed in Table 3.2. If the observations were made in the 4-CCD mode (high bit-rate) and 2-CCD mode (medium bit-rate), we used only the 4-CCD mode data. The data were corrected for spatial and gain non-linearity, residual dark distribution, dark frame error, and hot and flickering CCD pixels using standard procedures. Data were rejected during the South Atlantic Anomaly and at elevation angles less than the value listed in Table 3.3. In order to avoid contamination due to light leaks through the optical blocking filters, we excluded data taken when the satellite viewing direction of the bright rim of the Earth was within the angles listed in Table 3.3.

3.4 Images

For each observed field, we made X-ray images with two energy-bands (soft: 0.7–2 keV, hard: 2–10 keV) combining SIS 0 + 1, because SIS has better spatial resolution than GIS. We compared the SIS peak positions of bright X-ray sources in 0.7–2 keV band to the more accurately known IR/optical positions. This procedure (in this paper, we call it "the attitude fine tuning") is performed for each of the SIS field, if proper X-ray sources and their accurate optical positions are available. Then the absolute position error (the attitude determination error) of the SIS sources is reduced to as much as $\sim$5 arcsecs from $40''$ of the general errors (Gotthelf 1996), depending on the number of the reference sources and its X-ray flux and relative position in the SIS map. The sources we used for the attitude fine tuning and the offset of initial SIS image are listed in Table 3.4.

All the figures and tables we show are thus position-corrected ones. In the

figures, protostar candidates are indicated by crosses (Class I and some young Class II) and asterisks (Class 0). The contour levels are background-subtracted values.

3.5 Detection Criteria

Typically, the source data were extracted from $1'.2$ square region in the SIS images, then extracted the background data taken from a source-free box region. However the region size for the background varies from field to field depending on the source density and CCD chip mode. The background regions are indicated by solid-lined-box in images in the later chapters. After subtracting the background, we correct the count rates with the Point Spread Function and vignetting. For the sources of which the counts do not exceed a $5\times RMS$ signal-to-noise (S/N) criterion where the noise is based on the background Poisson statistics, we show only the upper limits of the count rates.

If we detect protostars, we executed further analysis for each of the protostars.

Table 3.1: Observed fields

Field	Field center		Date(UT)	Exposure
	RA(1950)	Dec(1950)	dd/mm/yy	ksec
RhoOphCore (PV)	16h 23.8m	$-24^\circ\ 22'$	20/08/93	40
RhoOphCore (AO6)	16h 24.4m	$-24^\circ\ 27'$	02/03/97	100
RhoEast (AO4, March)	16h 29.6m	$-24^\circ\ 21'$	20/08/93	20
RCrA (AO4, 1st day)	18h 58.0m	$-37^\circ\ 4'$	04/04/94	40
RCrA (AO4, 2nd day)	18h 59.0m	$-37^\circ\ 10'$	08/04/94	40
RCrA2 (AO6)	18h 58.8m	$-36^\circ\ 59'$	05/04/96	80
B209 (AO2)	4h 11.0m	$+28^\circ\ 10'$	16/02/95	40
B209 (AO3, 1st day)	4h 11.3m	$+28^\circ\ 7'$	16/09/95	30
B209 (AO3, 2nd day)	4h 10.9m	$+28^\circ\ 2'$	13/02/96	20
TMC1	4h 36.5m	$+25^\circ\ 47'$	13/02/96	40
IC359	4h 15.7m	$+28^\circ\ 18'$	02/09/95	40
L1551	4h 29.1m	$+18^\circ\ 0'$	23/02/94	40
Lupus 3	16h 5.5m	$-39^\circ\ 0'$	02/02/96	40
Serpens	18h 27.1m	$+1^\circ\ 15'$	15/04/97	100
NGC1333	3h 26.1m	$+31^\circ\ 12'$	30/08/95	100
L1448	3h 22.3m	$+30^\circ\ 29'$	30/08/95	100
NGC1977	5h 33.1m	$-5^\circ\ 0'$	30/04/93	20
Orion Nebula (PV)	5h 33.1m	$-5^\circ\ 20'$	30/04/93	20
Orion Nebula (AO5, 1st day)	5h 33.1m	$-5^\circ\ 21'$	23/09/97	50
Orion Nebula (AO5, 2nd day)	5h 33.0m	$-5^\circ\ 21'$	30/09/97	10
L1641North	5h 33.5m	$-6^\circ\ 33'$	13/03/94	40
HH212	5h 41.1m	$-1^\circ\ 9'$	28/02/98	30
HH91	5h 38.9m	$-1^\circ\ 18'$	01/03/98	30
L1582B	5h 29.3m	$+12^\circ\ 47'$	22/02/98	40

Table 3.2: SIS Mode

Field	HIGH Bit-rate		MEDIUM Bit-rate	
	Obs. mode	CCD mode	Obs. mode	CCD mode
RhoOphCore (PV)	FAINT	0123/2301	BRIGHT	0123/2301
RhoOphCore (AO6)	FAINT	0123/2301	FAINT	1212/3030
RhoEast (AO4, March)	FAINT	1111/3333	FAINT	1111/3333
RCrA (AO4, 1st day)	FAINT	0123/2301	BRIGHT	0123/2301
RCrA (AO4, 2nd day)	FAINT	0123/2301	BRIGHT	0123/2301
RCrA2 (AO6)	FAINT	1111/3333	FAINT	1111/3333
B209 (AO2)	FAINT	0123/2301	BRIGHT	0123/2301
B209 (AO3, 1st day)	FAINT	0101/2323	BRIGHT	0101/2323
B209 (AO3, 2nd day)	FAINT	0101/2323	BRIGHT	0101/2323
TMC1	FAINT	0123/2301	BRIGHT	0123/2301
IC359	FAINT	0123/2301	BRIGHT	0123/2301
L1551	FAINT	0123/2301	BRIGHT	0123/2301
Lupus 3	FAINT	0123/2301	BRIGHT	0123/2301
Serpens	FAINT	0123/2301	FAINT	1212/3030
NGC1333	FAINT	0123/2301	FAINT	0123/2301
L1448	FAINT	1111/3333	BRIGHT	1111/3333
NGC1977	FAINT	0123/2301	BRIGHT	0123/2301
Orion Nebula (PV)	FAINT	0123/2301	BRIGHT	0123/2301
Orion Nebula (AO5, 1st day)	FAINT	1111/3333	BRIGHT	1111/3333
Orion Nebula (AO5, 2nd day)	FAINT	1111/3333	BRIGHT	1111/3333
L1641North	FAINT	1111/3333	FAINT	1111/3333
HH212	FAINT	1111/3333	FAINT	1111/3333
HH91	FAINT	1111/3333	FAINT	1111/3333
L1582B	FAINT	1111/3333	FAINT	1111/3333

Table 3.3: Data selection and net observing time

Field	GIS			SIS			
	(1)	(2)	(3)	(4)	(5)	(6)	(7)
	[°]	[ks]	[ks]	[°]	[°]	[ks]	[ks]
RhoOphCore (PV)	10	38	38	5	40	27	27
RhoOphCore (AO6)	5	94	94	5	20	61†	63†
RhoEast (AO4, March)	5	20	20	5	20	21	21
RCrA (AO4, 1st day)	5	40	40	10	20	36	37
RCrA (AO4, 2nd day)	5	37	37	10	20	34	34
RCrA2 (AO6)	5	32	68	10	20	61	61
B209 (AO2)	5	43	43	10	20	38	39
B209 (AO3, 1st day)	5	25	25	10	20	22	22
B209 (AO3, 2nd day)	5	16	16	10	20	13	13
TMC1	5	41	41	10	20	36	37
IC359	5	39	39	10	20	24	24
L1551	5	42	42	10	20	40	40
Lupus 3	5	41	41	10	20	37	38
Serpens	5	89	89	10	20	48†	48†
NGC1333	5	94	94	10	20	76	81
L1448	5	53	53	10	20	49	49
NGC1977	5	17	17	10	20	16	16
Orion Nebula (PV)	5	20	20	10	20	18	19
Orion Nebula (AO5, 1st day)	5	50	50	10	20	45	0
Orion Nebula (AO5, 2nd day)	5	8	8	10	20	8	8
L1641North	5	37	37	10	20	34	34
HH212	5	33	33	10	20	31	31
HH91	5	26	26	10	20	24	25
L1582B	5	40	40	10	20	38	38

Column(1)(4): elevation angles from the Earth for GIS and SIS, respectively.

Column(2)(3)(6)(7): net observing time (GIS2, GIS3, SIS0, and SIS1, respectively).

Column(5): lower limit from the bright rim of the Earth.

†: net observing time during 4-CCD mode.

Table 3.4: Reference sources for the attitude fine tuning

Field	ref. sources	initial SIS offset		reference
		RA (s)	Dec ($''$)	
RhoOphCore (PV)	DoAr21, ROX7	-1.8	$+10.3$	(1)
RhoOphCore (AO6)	ROXs21, ROXs31	$+0.18$	-7.4	(2)
RhoEast (AO4, March)	IRAS16293-2424	-0.6	$+0.6$	(1)
RCrA (AO4, 1st day)	CrA1, HR7169, CrA2	-1.0	-2.6	(3)
RCrA (AO4, 2nd day)	CrA1, CrA2	$+1.0$	$+2.3$	(3)
RCrA2 (AO6)	CrA1	-0.8	-8.3	(3)
B209 (AO2)	V773 Tau, Anon 1	-3.3	-0.2	(4)
B209 (AO3, 1st day)	V773 Tau	$+4.6$	$+2.1$	(4)
B209 (AO3, 2nd day)	V773 Tau, Anon 1	-2.8	$+16.4$	(4)
TMC1	IRAS04369+2539, GN Tau	-0.09	-2.8	(5)
IC359	V410 Tau, Elias 1, Hubble 4	-0.06	-14.9	(4)
L1551	V826 Tau, L1551-51, 55	-1.3	-3.4	(4)
Lupus 3	Sz96	-1.9	-10	(4)
Serpens	EC95	$+3.1$	-4.7	(6)
NGC1333	source 10, source 19	$+1.6$	-2.7	(7)
L1448	—	—	—	—
NGC1977	—	$+1.8$	$+11$	(4)
Orion Nebula (PV)	HBC452, 463	$+1.8$	$+12$	(4)
Orion Nebula (AO5, 1st day)	Trapezium	-0.8	$+12$	(8)
Orion Nebula (AO5, 2nd day)	Trapezium	-1.6	$+3.0$	(8)
L1641North	HD37131	$+0.6$	-3.1	(8)
HH212	—	—	—	—
HH91	—	—	—	—
L1582B	—	—	—	—

References– (1):André & Montmerle 1994, (2): Barsony et al. 1997, (3): Digitized Sky Survey, (4): Herbig Bell Catalogue, (5): Jones & Herbig 1979 (6): Eiroa & Casali 1992, (7): Preibisch 1997, (8): data of PV phase, (9): Tycho Reference Catalogue

Chapter 4

Rho Ophiuchi ($D = 165$ pc)

The ρ Oph dark cloud is one of the nearest well-known star-forming regions, located at $(l, b) = (353, +16)$ with a distance of 165 pc from our solar system, hence about 35 pc above the Galactic plane (see Figure 1.1 and 1.2), and extending to 10°. The total mass of the molecular gas was estimated to be $3\times10^4 M_\odot$, which is typical among the Galactic dark clouds (Dame et al. 1987).

In the early observations with H_2CO (Loren et al. 1983), two concentrations of dense gas, named core A (near Lynds 1686) and core B (near Lynds 1681), were identified. These observations indicate that the peak densities of cores A and B are 10^5 cm^{-3} and 10^6 cm^{-3}, respectively. About 20 objects, including T Tauri-like variables, were found in the visual band in the vicinity of the main body. Their spectral types range from B2 V to G2 V (Chini 1981). From near-infrared observations, these cores show a high visual extinction $A_V = 50$–100 mag (Wilking & Lada 1983; Vrba et al. 1975; Vrba et al. 1976; Chini 1981). From the $C^{18}O$ observation in this region (Wilking & Lada 1983), the size and total mass were estimated to be 1×2 pc^2 and $\sim600 M_\odot$, respectively.

About 100 infrared objects were identified as YSOs in the main body of the ρ Oph dark cloud, and 80% of them were classified into infrared Class 0 to III; the ratio is 10%, 50%, and 40% for Class I, Class II, and Class III objects, respectively, and only two Class 0 sources are recognized (André & Montmerle 1994). From these populations of YSOs, the star-forming efficiency (SFE) was estimated to be $> 22\%$ in the ρ Oph core, which is much higher than the $> 2\%$ found in the Taurus complex (Wilking 1989).

Observations of individual objects in the infrared band have been made and

discussed by many authors (Wilking et al. 1989; Elias 1978a: Vrba et al. 1975; Simon et al. 1987; Adams et al. 1987; Wilking & Lada 1983; André & Montmerle 1994; Greene et al. 1994) and the main body is thought to be a progenitor of a bound open cluster, while the Taurus complex is thought to produce field stars.

The *Einstein* satellite found that Class II and III sources were bright and variable in the soft X-ray band (Montmerle et al. 1983). Their X-ray spectra were fitted by a thin thermal model with a temperature of about 1 keV, with absorption column densities in the range 10^{20}–10^{21} cm^{-2}. These X-ray sources show flickering in the soft X-ray band, referred to as an *X-ray Christmas Tree*. The overall distribution of the normalized amplitude of the variations is reproduced by a power law with an index of 1.4, which is similar to that of solar flares (Montmerle et al. 1983). Thus, the flickering phenomenon was explained by solar-like flare activities. No X-ray was found from any Class I sources. Casanova et al. (1995) with the deep *ROSAT* observation, reported 55 reliable detections of X-ray sources in the 1.0–2.4 keV energy band. Seven Class I sources (GSS 30–IRS 1/LFAM 1, GY 224, WL6/GY256, IRS43, IRS44/IRS46, IRS54, and IRS48) lie within the error circles of X-ray peaks. They noted, however, that these Class I identifications are marginal due to source confusion in the crowded region. Then, X-rays from one of the Class I sources were confirmed with the following HRI observation (Grosso et al. 1997). Neither *Einstein* satellite nor *ROSAT* detected X-rays from the Class 0 source VLA 1623.

The hard X-ray band (> 4 keV), on the other hand, has been studied by non-imaging instruments; hence, only spatially averaged information of each molecular core with a typical size of a square degree was available. The hard X-ray spectra of star-forming regions obtained by the Japanese X-ray satellites Temma and Ginga found that the cloud shows a higher temperature of $kT \sim 4$ keV with $N_H \sim 10^{22}$ cm $^{-2}$ and Fe abundance of 0.3–0.4 cosmic (Koyama 1987, Koyama et al. 1992). The temperature determined with hard X-rays arises a big question on the X-ray origin from the dark cloud. Another unresolved question is whether or not Class 0 and I sources are X-ray emitters.

Throughout this section, we assume the distance to the ρ Oph core to be 165 pc (Dame et al. 1987).

4.1 Core region (PV phase)

We show the two band contour maps of ρ Oph main cloud obtained with SISs in Figure 4.1.

In the hard band image, we detected several X-ray sources from the central region of the cloud (it lies near the center of the SIS field of view), while in the soft band image, we can see no X-ray from the region. We show the count rate of each source in Table 4.1. At least, we detected five Class I sources with $> 5\ \sigma$. In the following subsection, we concentrate on the bright Class I sources EL29 and WL6.

4.1.1 EL 29

No other IR candidate within the error region around EL 29 is found, hence we can firmly identify this point source to be EL 29, an infrared variable (Elias 1978a), Class I object located close to the CO peak (Wiliking & Lada 1983) near Lynds 1681. From this source, a hard X-ray flare in the 2–10 keV energy band was found. The light curve and the parameters are shown in Figure 4.2 and Table 4.2.

More detailed comparison of the flare and the quiescent states are given in Table 4.3. We note that the flare spectrum showed a significantly higher absorption ($N_H \sim 2 \times 10^{23}$ cm^{-2}) than that found in the quiescent spectrum ($N_H = 4 \times 10^{22}$ cm^{-2}). EL 29 shows a deep silicate absorption feature in the IR band (Hanner et al. 1995), may be due to a circumstellar disk (e.g. Kenyon et al. 1993). Simon (1987) found that the circumstellar envelope has spatial extension of 100 AU. We can therefore infer that the excess absorption during the X-ray flare arises through the dense disk along the line of sight, while the quiescent X-rays are produced over the region of the stellar surface, which do not suffer disk extinction. This flare phenomenon is similar to that of a large flare found from the Weak-lined T Tauri star V 773 Tau (Tsuboi et al. 1998). At the flare peak of V 773 Tau, high absorption was shown and it decreased as the flare decayed, although V773 Tau has no significant circumstellar disk. Some unknown process may possibly work during the flare event.

4.1.2 WL 6

This source exhibited sinusoidal variability during the observation (Figure 4.2). No significant difference in the plasma temperature and absorption between the high- and low-state spectra was found (Table 4.3). These characteristics differ from flare properties (e.g. EL 29). We suspect that the energy-independent and sinusoidal modulation of this source is due to a modulation of the X-ray emitting region along with possible stellar rotation. The period of the sinusoidal curve was about 0.97 day. A fast stellar rotation causes a high X-ray luminosity, as in RS CVn stars (Rosner et al. 1985). If the flux variation of this source is due to stellar rotation, this would be the first discovery of fast spin from a protostar.

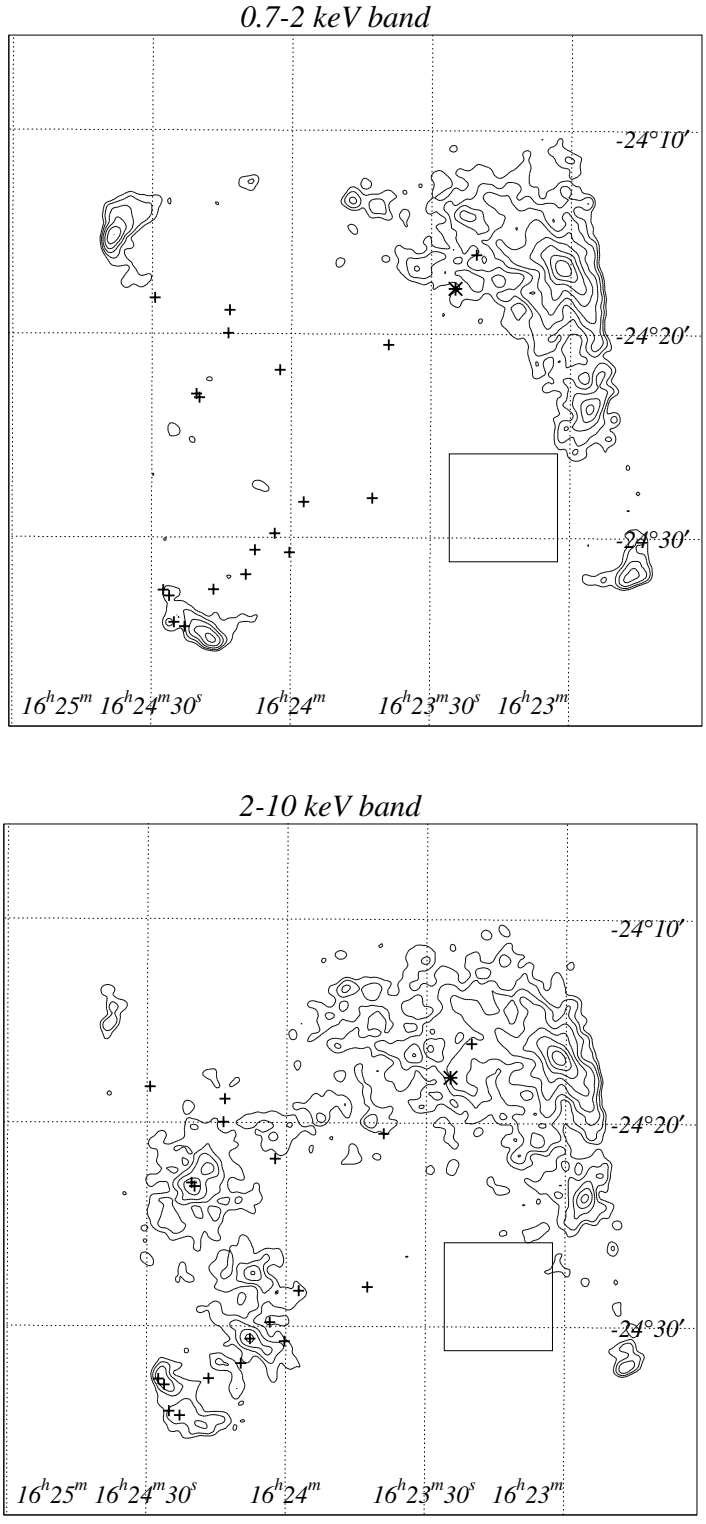

Figure 4.1: X-ray images of the ρ Oph cloud main body (PV phase), obtained with SISs. The contour levels for both band maps, in units of (10^{-3}counts/SIS/ks/pixel), are : 0.3, 0.5, 0.9, 1.4, 2.4, 3.9, 6.4, and 10.5.

Table 4.1: Protostar candidates in Rho Oph Core (PV)

Name	RA (1950)	Dec (1950)	0.7–2 keV (cts ks^{-1} SIS^{-1})	2–10 keV (cts ks^{-1} SIS^{-1})	Class
WL12	16 23 42.5	−24 28 4	≤0.5	≤1.1	I
IRS27=WL22	16 23 57.3	−24 28 15	≤1.3	4.8±1.2	II?†
WL16	16 24 0.3	−24 30 44	≤1.4	8.6±1.8	II?†
IRS29=WL1	16 24 2.4	−24 21 46	≤0.7	≤1.8	I
EL29	16 24 7.7	−24 30 37.2	≤0.7	22.0±2.6	I
IRS34	16 24 13.6	−24 19 58	≤0.7	3.3±0.8	II†
IRS43=YLW15	16 24 25.1	−24 34 9.9	≤5.2	≤8.6	I
IRS44	16 24 26.2	−24 32 53	≤5.8	8.2±2.3[c]	I
IRS46	16 24 27.4	−24 32 36	≤4.0	8.5±2.3[c]	I
WL6	16 24 19.8	−24 23 8	≤1.8	22.5±2.1	I
LFAM1	16 23 20.3	−24 16 6.6	—[a]	—[a]	I
WL19	16 24 9.7	−24 31 49	≤4.3	5.9±1.7	II–IID†
RhoOphB	16 24 13.3	−24 18 50	≤0.4	≤1.3	I
GY245=CRBR72	16 24 16.6	−24 32 34	≤3.8	≤3.7	I
GY284	16 24 29.4	−24 18 15	≤0.6	≤0.5	I
CRBR42=GY91	16 23 39.1	−24 20 32	≤0.3	≤1.5	I
CRBR85	16 24 22.8	−24 34 23	—[b]	12.6±2.8[d]	I
LFAM26	16 24 03.5	−24 29 48.1	≤0.7	6.9±1.6	I
YLW256=GY256	16 24 20.4	−24 22 58	≤2.4	—[e]	I
VLA1623	16 23 25.0	−24 17 47	—[a]	—[a]	0

a: contaminated by X-rays from a complex of many unresolved T Tauri stars.

b: contaminated by X-rays from T Tauri star ROXs 31.

c: IRS44 and IRS46 may contaminate each other.

d: CRBR85 is unresolved from IRS43.

e: contaminated by WL 6.

†: classification by André & Montmerle (1994).

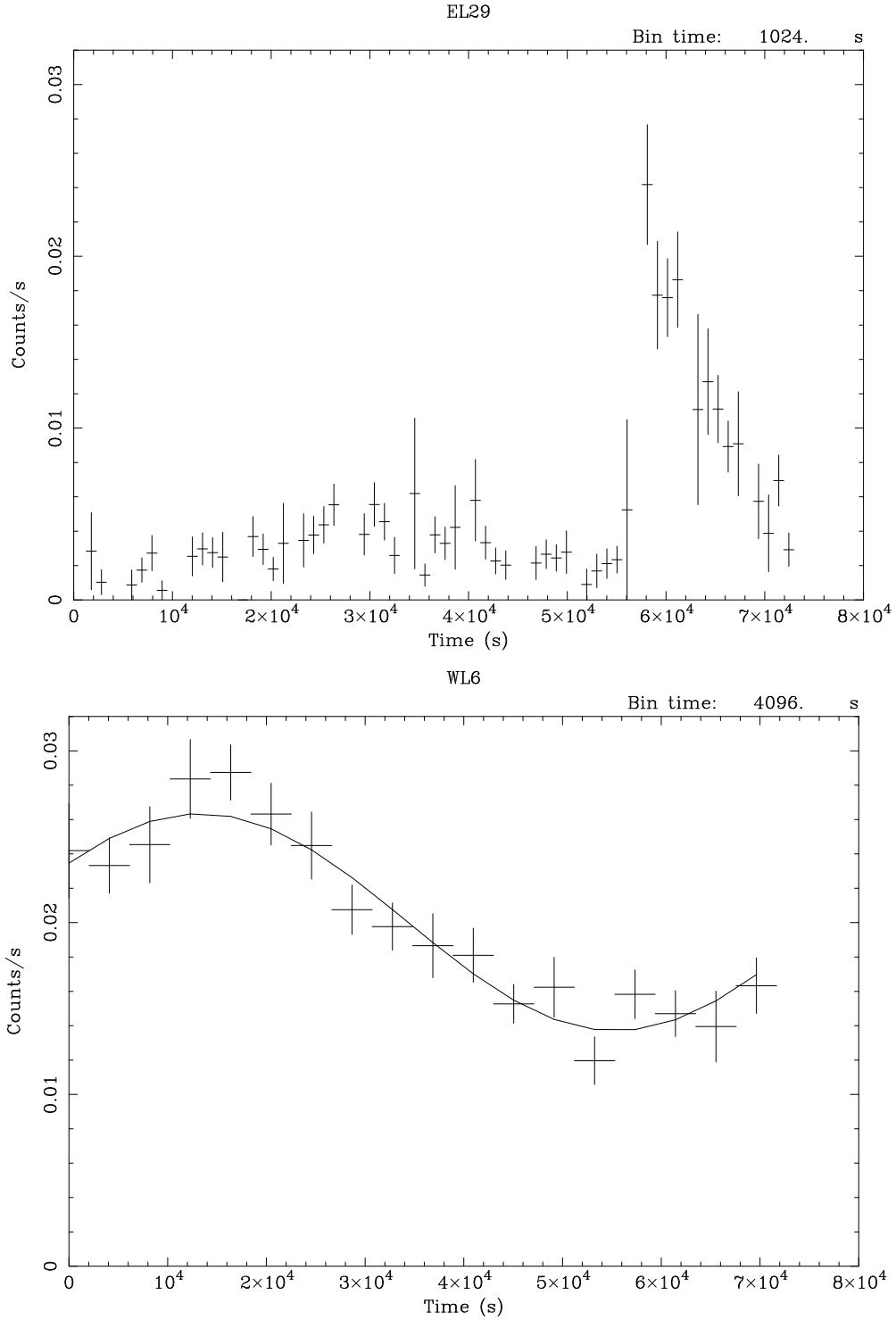

Figure 4.2: X-ray light curves of EL29 and WL 6. Background is not subtracted. The X-ray data of EL29 Were extracted from a 1-arcmin radius circle centered on the EL29, while those of WL 6 were extracted from a 3-arcmin radius circle centered on the Wl6. The data obtained by SIS 0, 1 and GIS 2, 3 are averaged.

Table 4.2: The minimum and maximum luminosities of Class I sources

Source	$L_{x\ max}$ (2–10 keV) [10^{30} erg s^{-1}]	$L_{x\ min}$ (2–10 keV) [10^{30} erg s^{-1}]	Variability probability† (0.7–10 keV)	ASCA Flare
EL 29	54.1±9.9	3.3±2.3	>99.9%	yes
WL 6	13.9±5.1	2.5±1.7	>99.9%	not but sinusoidal
IRS 44/46	10.5±4.4	2.5±1.5	90.8%	

†: Comments are for flare or quiescent component and high or low state.

Table 4.3: Best-fit parameters to spectra of EL29 and WL6.

Source	kT [keV]	Fe abundance [solar]	$N_{\rm H}$ [10^{22}cm^{-2}]	χ^2 [d.o.f]	Comment
EL 29	$4.0^{+4.6}_{-2.3}$	$1.2^{+2.6}_{-0.6}$	19^{+11}_{-6}	1.94 (53)	Flare
EL 29	3.0 (fixed)	$0.37^{+1.19}_{-0.37}$	$3.8^{+1.5}_{-1.3}$	1.94 (53)	Quiescent
WL 6	$2.2^{+0.5}_{-0.4}$	0.3 (fixed)	$4.6^{+1.0}_{-0.6}$	1.55 (56)	High state
WL 6	$2.2^{+1.0}_{-0.6}$	0.3 (fixed)	$5.0^{+1.4}_{-1.1}$	0.88 (56)	Low state

These parameters are obtained using SISs & GISs. The errors and upper limits are at 90% confidence level.

4.2 Core region (AO6)

We executed the second ASCA observation of the main body of ρ Ophiuchi 3.5 years after the first observation to detect further time variability of protostars. Towards the end of this observation, we detected an enormous flare from T Tauri star ROXs31 which is located close to YLW15 (see §3.1, source 6 in Figure 4.3. The peak flux of ROXs31 is about 1 count s $^{-1}$, which is 1–2 orders of magnitude larger than YLW15 (see chapter11), and its broad point spread function contaminates YLW15 during the flare. Therefore, we excluded the GIS and SIS data taken during the flare of ROXs31 in all analysis of YLW15.

Figure 4.3 shows X-ray images of the main body of this cloud. After the attitude fine tuning, remaining excursions (the absolute position error) between the X-ray and IR positions are 5.5″ (rms), which is consistent with the SIS position uncertainty for point sources (Gotthelf 1996). Then we take the systematic positional error to be 5.5″.

In the 2–10 keV band image (Figure 4.3, right panel), we can see several X-ray sources from the center of this cloud. The brightest X-ray source in the 2–10 keV band is an unresolved source at $\alpha(1950) =$ 16h 24m 25.1s and $\delta(1950) = -24^\circ$ 34′ 10.3″. We derived this peak position by two-dimensional fitting in the 2–10 keV band using the Display45 analysis software package (Ishisaki et al. 1998). Since the statistical error is 1″, the overall X-ray error (including the absolute position error) is ±6″.

The closest IR source is YLW15 with the VLA position of $\alpha(1950) =$ 16h 24m 25.0s and $\delta(1950) = -24^\circ$ 34′ 9.8″ (±0.5″; Leous et al. 1991), hence is located away from the nominal position of the X-ray source by only 1.5″, and within the error region. The next nearest source is GY263 with IR position of $\alpha(1950) =$ 16h 27m 24.7s and $\delta(1950) = -24^\circ$ 40′ 4.9″ (±1.3″; Barsony et al. 1997). The source is located 5.5″ from the X-ray position, which is on the border of the X-ray position error circle. Thus we conclude that the hard X-rays are most likely due to the Class I source YLW15.

The other detected hard X-ray sources (with a criterion of S/N $\geq 5\sigma$) are two older Class I sources, IRS51 (source 2) and EL29 (source 3), which have flat SEDs. L29 (source 3) and WL6 (source 4) are faint, though both of them emitted strong X-rays in the first *ASCA* observation made in August 1993 (for comparison, see

Figure 4.1.

4.2.1 YLW15

Lightcurves

We extracted a lightcurve from a 3′ radius circle around the X-ray peak of YLW15 (see Figure 4.3). Before the enormous flare from T Tauri star ROXs31, which occurred in the last phase of this observation, we detected another large flare from Class II source SR24N, located about 7′ away from YLW15 in the GIS field of view. To subtract the time variable contamination from the SR24N in the extended flux of YLW15, we selected a 3′ radius background region (dotted circle in Figure 4.3), equidistant from SR24N and YLW15. On the other hand, using such a background, we cannot exclude the contamination from ROXs21 (source 5 in Figure 4.3), which is 2 arcmin apart from YLW15. Since the X-rays from ROXs21 are dominant below 2 keV (see the next subsection), we examine time variability only in the hard X-ray band (> 2 keV) in which the flux is dominated by YLW15.

Figure 4.4 (upper panel) shows the background-subtracted lightcurve in the 2–10 keV band with the sum of the SIS (SIS 0 and 1) and GIS (GIS 2 and 3). The light curve shows a saw-tooth pattern with three flares. The peak fluxes of the flares become successively less luminous. Each flare exhibits a fast-rise and an exponential decay with an e-folding time of 31±1 ks ($\chi^2/d.o.f. = 61/46$), 33±3 ks (80/47), and 58^{+24}_{-13} ks (33/24), for the first, second, and the third flares, respectively. We show the best fit lightcurves for the second and the third flares with dashed lines, and show the best-fit quasi-static model (see chapter 11) for the first flare with a solid line in Figure 4.4 upper panel.

Time-Sliced Spectra

To investigate the origin of the quasi-periodic flares, we made time-sliced spectra for the time intervals given in Figure 4.4. We extracted the source and background data for each phase from the same regions as those in the light curve analysis. We found that all the spectra show a local flux minimum at ≈1.2 keV. For example, we show the spectra obtained with SISs at phases 1 and 8 in Figure 4.5. This suggests that the spectra have two components; one is hot with heavy absorption and the other is cool with less absorption.

Then we examined possible contamination from the bright, soft X-ray source ROXs21 (source 5 in Figure 4.3). We extracted the spectrum of ROXs21 from a $2'$ radius circle around its X-ray peak. We extracted the data during phase 1, in order to be free from contamination from the flare on SR24N, which occurred during phases 4–6 (see above paragraph of the light curve analysis). The background data for ROXs21 were extracted from a $2'$ radius circle at the same distance from ROXs21 as that of YLW15, when YLW15 was in the flare phase 1. After the subtraction of the background, the spectrum of ROXs21 is well reproduced by an optically thin thermal plasma model with $\chi^2/d.o.f. = 17/23$. The best-fit temperature is about 0.6 keV at the fixed absorption of $N_{\rm H}$ =1.3×10^{21} cm^{-2} , which is estimated from $A_V = 0.6$ mag (Bouvier and Appenzeller 1992). The flux of the soft component of YLW15 is about 30% of the flux of ROXs21, which is nearly equal to the spill-over flux from ROXs21. Thus the soft X-ray component found in the YLW15 spectra is due to the contamination from the nearby bright source ROXs21.

Having obtained the best-fit spectrum of ROXs21, we fitted the spectrum of YLW15 in each phase with a two-temperature thermal plasma model. The cool component is set to the contamination from ROXs21, and the hot component is from YLW15. For YLW15, free parameters are temperature (kT), emission measure (EM), absorption ($N_{\rm H}$) and metal abundance. For ROXs21, EM is the only free parameter and the other parameters are fixed to the best-fit values obtained in phase 1. We found no significant variation in the absorption of YLW 15 from phase to phase, hence, we fixed the absorption column to the best-fit value at phase 1. The resulting best-fit parameters of YLW15 for each time interval are shown in Table 4.5. The best-fit spectra of phases 1 and 8 are illustrated in Figure 4.5, and the time evolution of the best-fit parameters are shown in Figure 4.4.

The physical condition and origin of the triple flare are discussed in chapter 11.

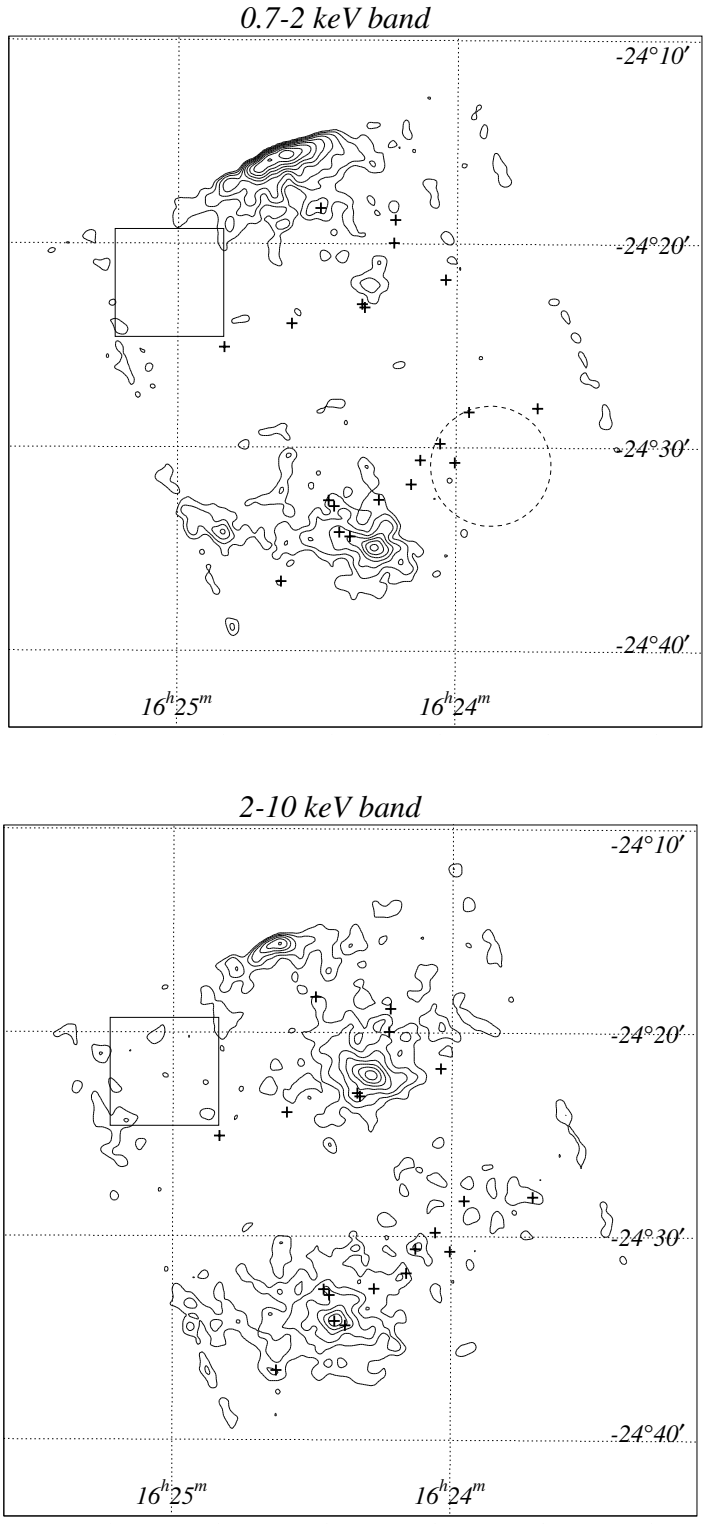

Figure 4.3: X-ray images of the ρ Oph cloud main body (AO6), obtained with SISs. The contour levels, in units of (10^{-3}counts/SIS/ks/pixel), are: 0.3, 0.7, 1.1, 1.6, 2.3, 3.2, 4.4, 6.0, 8.0, and 10.6 for the soft band, 0.3, 0.8, 1.5, 2.4, 3.5, 5.0, 6.9, 9.4, 12.7, and 17.0 for the hard band. The background region for YLW15, which was used in the lightcurve and spectral analysis, is shown by a dotted circle.

Table 4.4: Protostar candidates in Rho Oph Core (AO6)

Name	RA (1950)	Dec (1950)	0.7–2 keV (cts ks^{-1} SIS^{-1})	2–10 keV (cts ks^{-1} SIS^{-1})	Class
WL12	16 23 42.5	−24 28 4	≤1.4	≤9.1	I
IRS27=WL22	16 23 57.3	−24 28 15	≤1.0	≤3.5	II?†
WL16	16 24 0.3	−24 30 44	≤1.2	≤2.2	II?†
IRS29=WL1	16 24 2.4	−24 21 46	≤0.8	≤1.1	I
EL29	16 24 7.7	−24 30 37.2	≤1.1	8.5±1.8	I
IRS34	16 24 13.6	−24 19 58	≤0.8	—^{d}	II†
IRS43=YLW15	16 24 25.1	−24 34 9.9	—^{a}	93.0±3.9	I
IRS44	16 24 26.2	−24 32 53	—^{a}	—^{c}	I
IRS46	16 24 27.4	−24 32 36	—^{a}	—^{c}	I
IRS48	16 24 35.5	−24 23 55	≤0.6	≤0.9	I
IRS51	16 24 37.6	−24 36 35	≤4.7	17.4±3.1	I
IRS54	16 24 50	−24 25 5	≤0.9	≤1.2	I
WL6	16 24 19.8	−24 23 8	≤2.3	—^{d}	I
WL19	16 24 9.7	−24 31 49	≤1.2	≤8.6	II–IID†
RhoOphB	16 24 13.3	−24 18 50	≤2.6	≤6.3	I
GY245=CRBR72	16 24 16.6	−24 32 34	≤3.8	≤5.0	I
GY284	16 24 29.4	−24 18 15	—^{b}	≤5.4	I
CRBR85	16 24 22.8	−24 34 23	—^{a}	—^{c}	I
LFAM26	16 24 03.5	−24 29 48.1	≤1.0	≤2.2	I
YLW256=GY256	16 24 20.4	−24 22 58	≤1.7	—^{d}	I

a: contaminated by X-ray from T Tauri star ROXs21/SR12A-B.

b: contaminated by X-ray from T Tauri star ROXs29.

c: contaminated by X-ray from IRS43.

d: contaminated by X-rays from T Tauri stars GY244, 246, and 247.

†: classification by André & Montmerle (1994).

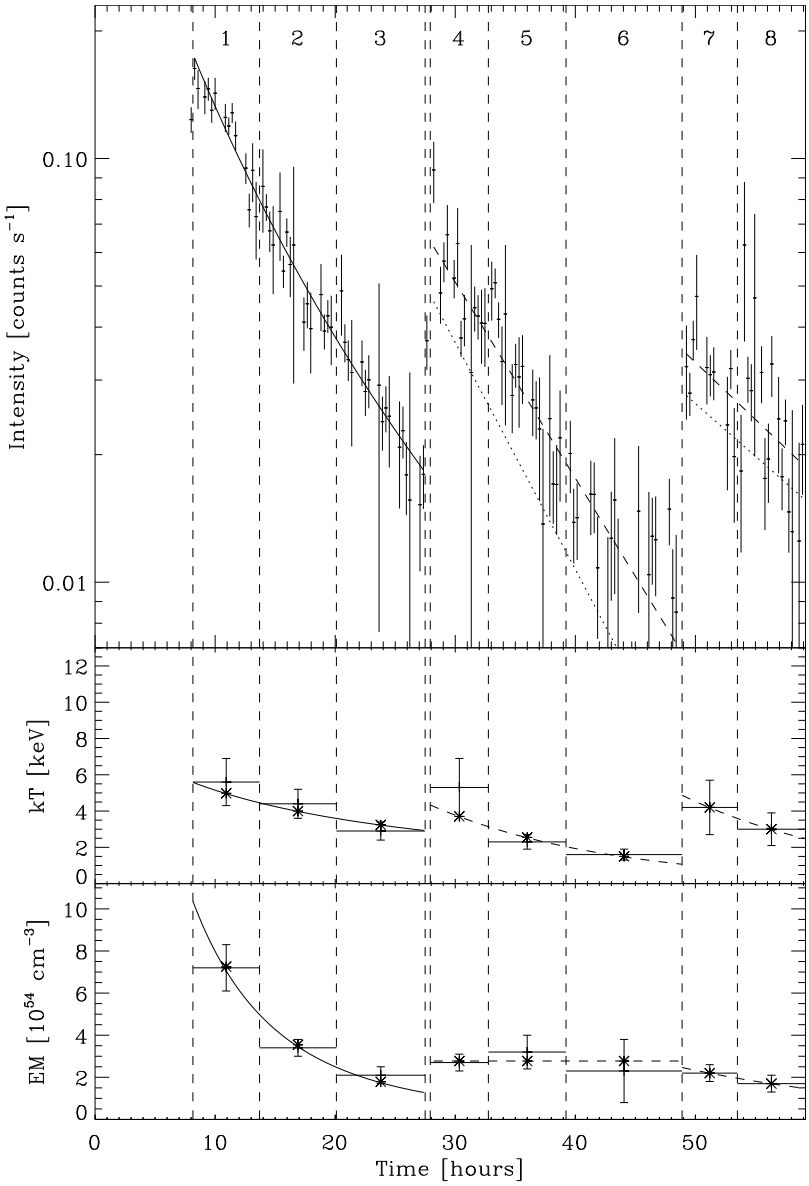

Figure 4.4: Upper panel: Background-subtracted lightcurve of YLW15 obtained with all the detectors (SIS 0 + SIS 1 + GIS 2 + GIS 3) in the 2–10 keV band. All time bins are 1024 s wide. Middle panel: Time profile of the best-fit temperature. The error bars indicate 90% confidence. Lower panel: Same as the middle panel, but for the best-fit emission measure. The solid lines during Flare I are the best-fit quasi-static model, and the dashed lines during Flare II and III are the best-fit exponential model. One reheating plasma loop is assumed in both cases. Dotted lines during Flare II and III in the upper panel show each flare component without the contribution of the other flares, under assumption that the three flares occurred independently (see chapter11). Asterisks show the average of the model during one time bin. The time axis starts at 00:00:00.0 UT (1997 March 2).

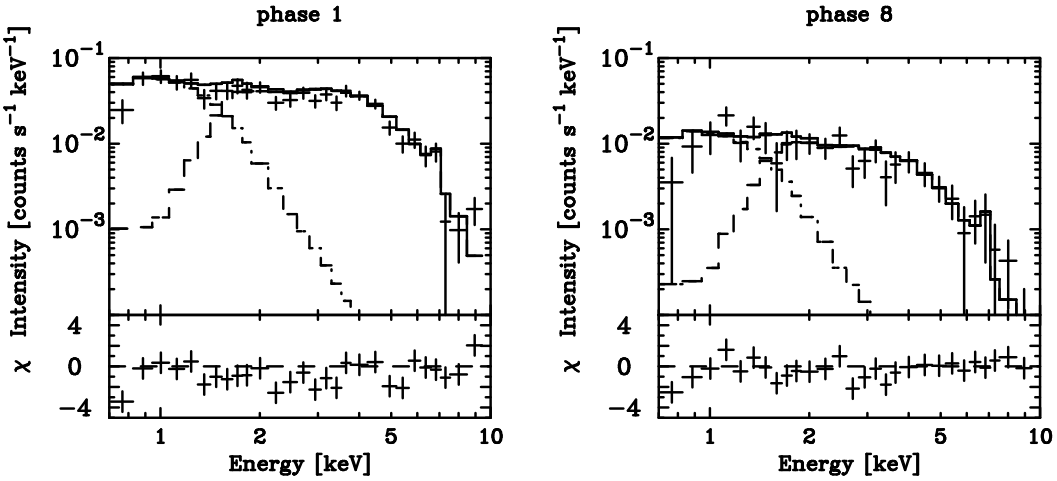

Figure 4.5: The SIS (SIS 0 + 1) spectra of YLW15 at phase 1 and 8 (see Figure 4.4). The solid lines show the best-fit two-temperature coronal plasma model derived from simultaneous fitting of GIS and SIS data. Lower panel shows the residuals from the best-fit model.

Table 4.5: Best-fit parameters to spectra of YLW15[a].

Phase[b]	kT	Abundance	EM[c]	$L_{\rm X}$[d]	$\chi^2/d.o.f$
	(keV)	(solar)	(10^{54}cm^{-3})	(10^{31}ergs s^{-1})	
1	$5.6^{+1.3}_{-1.0}$	$0.4^{+0.2}_{-0.1}$	$7.2^{+1.1}_{-0.8}$	15±1	181/106
2	$4.4^{+0.8}_{-0.7}$	$0.4^{+0.2}_{-0.2}$	$3.4^{+0.4}_{-0.3}$	6.0±0.7	191/164
3	$2.9^{+0.5}_{-0.3}$	$0.7^{+0.5}_{-0.4}$	$2.1^{+0.4}_{-0.3}$	3.4±0.7	80/84
4	$5.3^{+1.6}_{-1.1}$	$0.6^{+0.4}_{-0.4}$	$2.7^{+0.4}_{-0.3}$	5.6±1.0	55/52
5	$2.3^{+0.4}_{-0.3}$	$0.5^{+0.6}_{-0.4}$	$3.2^{+0.8}_{-0.7}$	4.4±1.2	163/138
6	$1.6^{+0.3}_{-0.3}$	<1.3	$2.3^{+1.5}_{-1.2}$	2.5±1.8	46/40
7	$4.2^{+1.5}_{-0.9}$	<0.4	$2.2^{+0.4}_{-0.3}$	3.5±0.5	153/139
8	$3.0^{+0.9}_{-0.5}$	$0.7^{+1.3}_{-0.5}$	$1.7^{+0.4}_{-0.4}$	2.9±0.6	59/65

The errors and upper limits are at 90% confidence level. The distance of YLW15 is assumed to be 165 pc.

[a] Absorption column density, fixed to the best-fit value for phase 1, or 3.3×10^{22} cm^{-2}.

[b] see Figure 4.4

[c] Volume Emission Measure, $\int n_e^2 dV$ (n_e: electron density, V: emitting volume).

[d] Absorption-corrected X-ray luminosity in the 0.1 – 100 keV band.

4.3 East region (AO4: 1996 Mar 3)

We observed the east region of the Rho Ophuchi cloud on Aug 20 1993. This region, includes IRAS16293−2422, one of the most famous Class 0 objects, which exhibits molecular outflow complex (Mizuno et al. 1990).

Figure 4.6 shows the SIS image of the cloud. The position of the Class 0 source IRAS16293–2424 is shown by asterisk, but we see no X-ray from the source in both the energy bands.

Table 4.6: Protostar candidates in Rho Oph East region

Name	RA (1950)	Dec (1950)	0.7–2 keV (cts ks^{-1} SIS^{-1})	2–10 keV (cts ks^{-1} SIS^{-1})	Class
IRAS16293−2422	16 29 20.9	−24 22 13	≤0.4	≤0.6	0

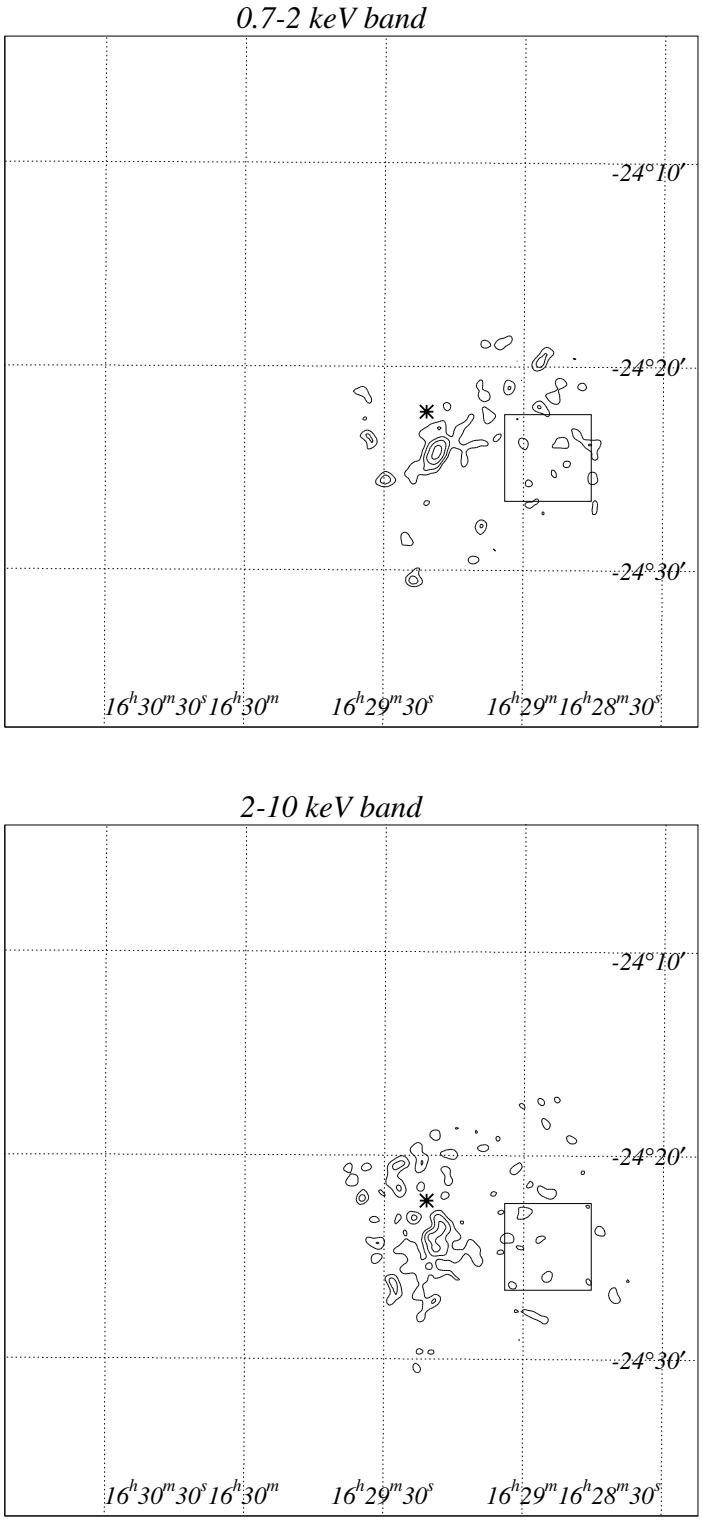

Figure 4.6: X-ray images of the ρ Oph East region, obtained with SISs. The contour levels, in units of (10^{-3}counts/SIS/ks/pixel), are : 0.1, 0.2, 0.3, and 0.6 for the soft band, 0.1, 0.3, and 0.5 for the hard band.

Chapter 5

Coronae Australis ($D = 130$ pc)

The Coronae Australis cloud is one of the closest star forming region, located at $(l, b) = (0, -17 \sim -22)$ with a distance of 130 pc from our solar system (Marraco & Rydgren 1981). Due to the high Galactic latitude (see Figure 1.1), it appears to be free of foreground or background dust and molecular gas. The total mass of the cloud was estimated to be about 7000 $M_{\odot}$ (e.g. Cappa de Nicolau & Pöppel 1991).

This cloud is separated to three large molecular condensations embedded in neutral hydrogen (Cappa de Nicolau & Pöppel 1991). The most massive of the clouds ($\sim$4300 $M_{\odot}$), which is lying closest to the Galactic plane $b = -18°$, coincide with the cloud A in Rossano's (1978) extinction map. This cloud is usually called the R CrA cloud according to the well-known variable star in the cloud center.

The highest density region of the R CrA core is distinctly seen in the millimeter-wave continuum and the CS (5–4) and (7–6) emission covering a $2'$ diameter region centered on the embedded source IRS 7 (also known as R1; Henning et al. 1994; Saraceno et al. 1996). The total visual extinction through the densest part of the core is estimated from the $C^{18}O$ column density to be $A_V \sim$35 mag (Wilking et al. 1992).

The R CrA cloud contains many variable stars (Taylor & Storely 1984). The brightest star in the cloud is Herbig Be star TY CrA, which has almost reached the zero-age main- sequence, whereas the stars S CrA, T CrA, VV CrA and R CrA are still before the zero age main sequence (Knackle et al. 1973). Bibo (1992) classified R and T CrA as members of the Herbig Ae/Be stellar group as well as TY CrA. A compact embedded cluster of 15 objects, dubbed the Coronet, was

found surrounding the star R CrA in an infrared survey of the core (K<14 mag; Taylor & Storey 1984). Further IR observations by Wilking et al. (1986, 1992) revealed more IR sources and showed that five among the sources detected by Taylor & Storey (1984) have an IR spectral index of $\alpha > 0.2$. These five sources are therefore classified as Class I objects (see Wilking et al. 1984). Wilking et al. (1997) performed a deep near-IR (NIR) imaging survey of the R CrA core. Their sample of 692 K-band sources can be expected to reveal the complete population of Class I and II sources in the core.

Koyama et al. (1996) presented the results of a deep (80 ks) ASCA observation of the Coronet region. In their X-ray image, they found five peaks which seem to coincide with the positions of the five Class I protostars. Neuhäuser and Preibisch (1997) analyzed archival ROSAT data of the CrA star forming region, and confirmed the X-ray emission from three of the five infrared Class I protostars.

After the first observation with ASCA (AO 4: Koyama et al. 1996), we executed the follow-up observation in AO 6. In this section, we mainly report the new results obtained in the AO 6 observation, comparing those in AO 4.

5.1 Core region 1 (AO 4 the 1st day)

We observed the center of the Coronet cluster on April 4 1994. We show the two energy-band images obtained with SISs in Figure 5.1.

As Koyama et al. (1996) noticed, we see a bright complex structure around the cloud core (the Coronet clusters) in the hard X-ray band, while in the soft X-ray band image, we see the X-rays from T Tauri stars and Herbig Ae/Be stars (e.g. Cr A 1, HD 176386, TY CrA) which are distributed in less obscured region of this cloud.

We show the count rate of each protostar in Table 5.1. Since IRS 7 and IRS 9 are unresolved each other, we show the sum of the count form IRS & and IRS 9. In the region (IRS 7 + IRS 9), the Herbig Ae star R CrA is also included, however, considering the large absorption of the spectrum (Koyama et al. 1996), R CrA can be excluded as the origin of the X-rays.

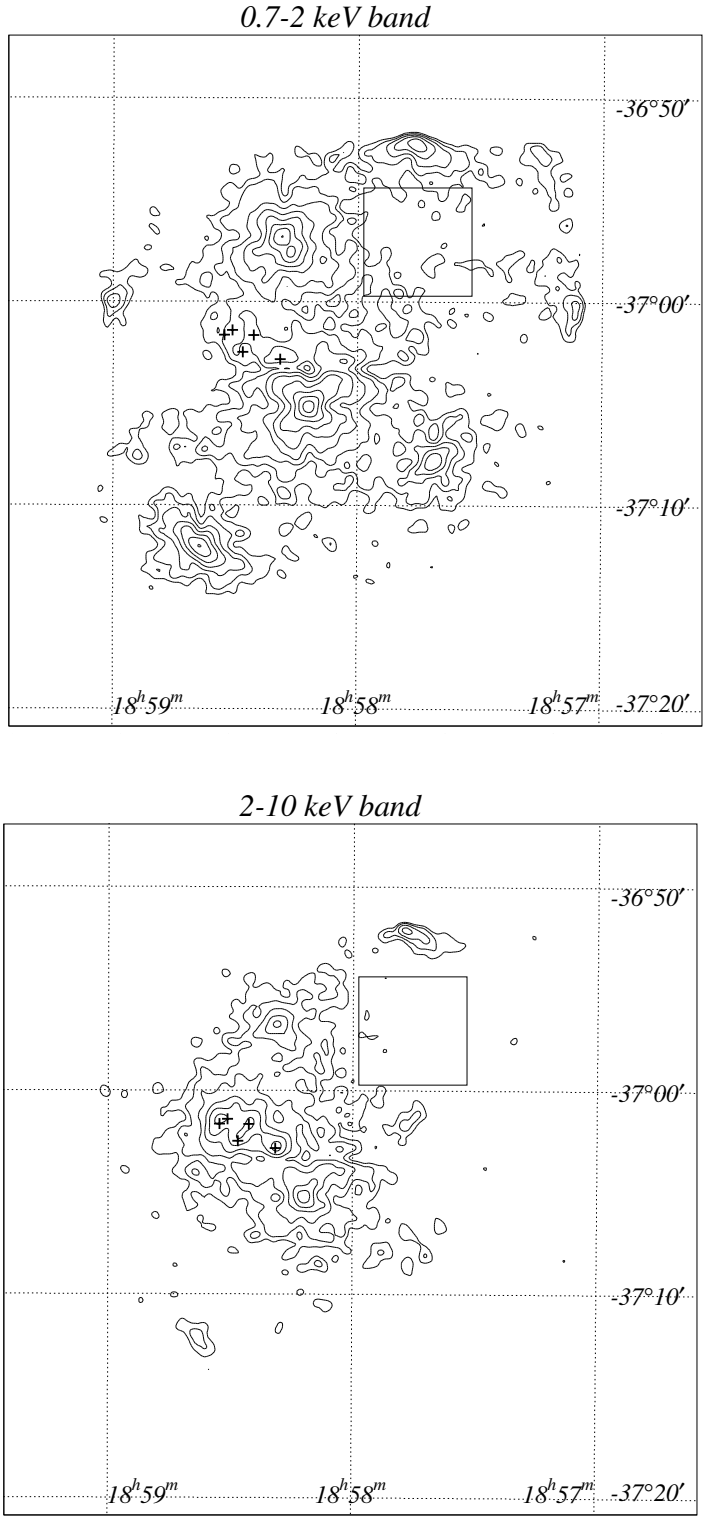

Figure 5.1: X-ray images of the R CrA cloud core (AO4, the first day), obtained with SISs. The contour levels for both of the band maps, in units of (10^{-3}counts/SIS/ks/pixel), are : 0.3, 0.5, 0.9, 1.6, 2.7, 4.3, 7.0, 11.2, and 17.8.

Table 5.1: Protostar candidates in the R CrA region (AO4, the first day)

Name	RA (1950)	Dec (1950)	2–10 keV (cts ks^{-1} SIS^{-1})	Class
IRS 2=TS 13.1	18 58 19	−37 2 50	26.2±1.6	I
IRS 5=TS2.4	18 58 25.5	−37 1 39	32.1±1.8	I
IRS 1=TS2.6	18 58 28.2	−37 2 29	25.3±1.7	I
IRS 7 + IRS 9[a]	(18 58 31.7	−37 1 31.5)	41.5±2.5	I
IRS 9=R2	18 58 30.7	−37 1 24		I
IRS 7=R1	18 58 32.7	−37 1 39		I

In the soft band (0.7–2 keV), all of the protostar candidates are contaminated by a bright source T Tauri star CrA 1.

a: This region also includes Herbig Ae star R CrA: α(B1950) = 18h 58m 31.6s, δ(B1950) = -37° $01'$ $30''$, however, with the large absorption of the spectrum (Koyama et al. 1996), R CrA is excluded as the origin of the X-ray.

5.2 Core region 1 (AO 4 the 2nd day)

We observed 10′ east from the center of the Coronet cluster on 1994 April 8. We show two energy-band X-ray images obtained with SISs in Figure 5.2.

The soft X-ray band image is similar to the image obtained on 1994 April 4. However, in the hard X-ray band, we see an X-ray enhancement at the position of R1, which is largely different from the observation on 1994 April 4. This X-ray enhancement is likely due to the X-ray flare from R1 (Koyama et al. 1996).

We show the count rate of each protostar in Table 5.2. Here also, we show those of IRS 7 and IRS 9 by the sum of the counts, however, as Koyama et al. (1996) mentioned, we can conclude the largest contribution to the hard X-ray is due to R1, because R1 is the closest to the hard X-ray peak, and within the error circle of hard X-ray peak, no other cataloged source is found.

Table 5.2: Protostar candidates in R CrA region (AO4, the second day)

Name	RA (1950)	Dec (1950)	0.7–2 keV (cts ks^{-1} SIS^{-1})	2–10 keV (cts ks^{-1} SIS^{-1})	Class
IRS 2=TS 13.1	18 58 19	−37 2 50	—[a]	43.2±2.7	I
IRS 5=TS2.4	18 58 25.5	−37 1 39	—[a]	34.8±2.4	I
IRS 1=TS2.6	18 58 28.2	−37 2 29	—[a]	41.5±2.5	I
IRS 7 + IRS 9[b]	(18 58 31.7	−37 1 31.5)	—[a]	61.1±3.0	I
IRS 9=R2	18 58 30.7	−37 1 24			I
IRS 7=R1	18 58 32.7	−37 1 39			I
IRAS32	18 59 35.8	−37 11 53	≤0.5	≤0.6	I

a: In the soft band (0.7–2 keV), all of the protostar candidates but IRAS32 region are degraded by T Tauri star CrA 1.
b: Herbig Ae star R CrA: α(B1950) = 18h 58m 31.6s, δ(B1950) = −37° 01′ 30″, however, with the large absorption of the spectrum (Koyama et al. 1996), R CrA is excluded for the origin of the X-ray.

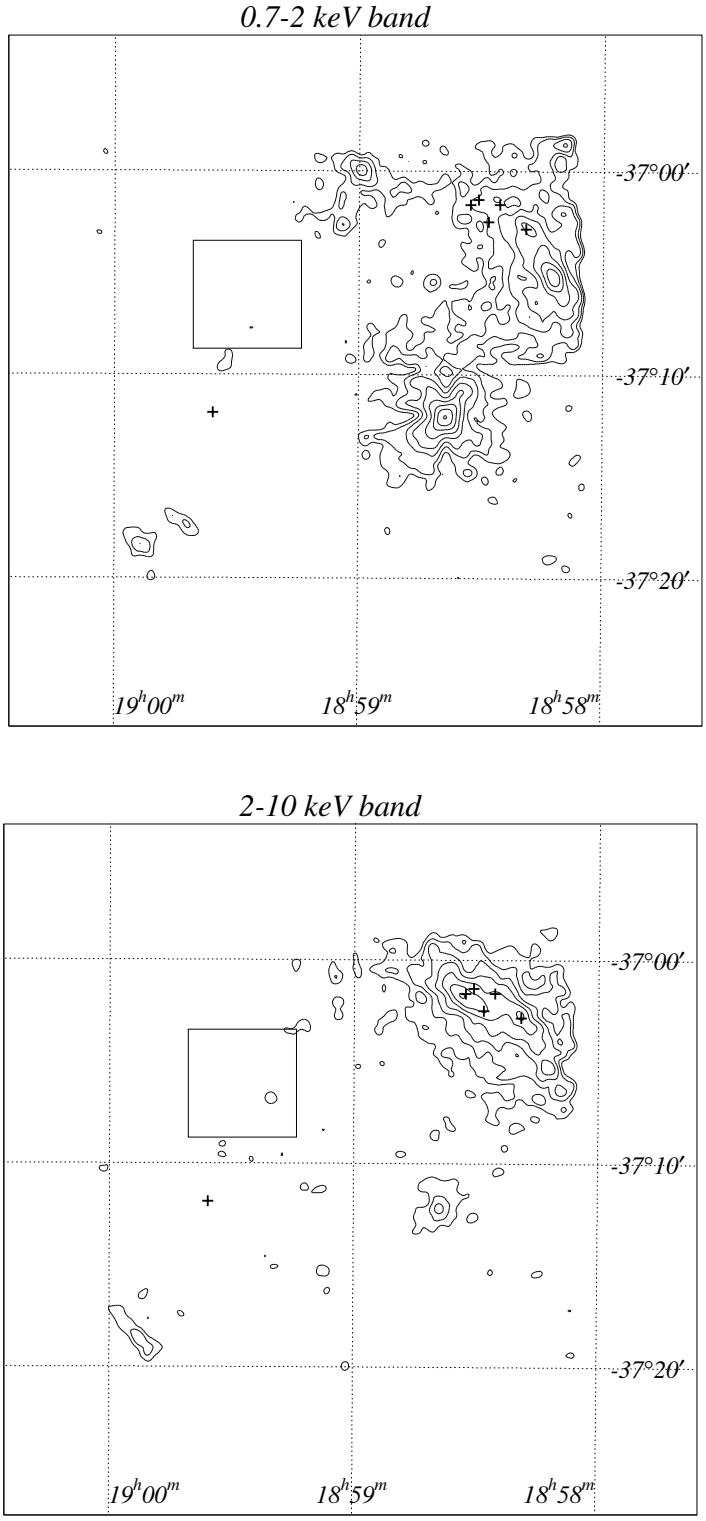

Figure 5.2: X-ray images of the R CrA cloud core (AO4, the second day), obtained with SISs. The contour levels for both of the band maps, in units of (10^{-3}counts/SIS/ks/pixel), are : 0.4, 0.6, 1.0, 1.7, 2.8, 4.4, 7.1, and 11.3.

5.3 Core region 2 (AO 6)

We executed the follow-up observation of the center of the Coronet cluster on April 5 1996. We show the two-energy band X-ray images obtained with SISs in Figure 5.3.

In the soft X-ray band image, we see almost same X-ray distribution as the previous two observations. However, in the hard X-ray band, we see that X-rays from a complex of R2 and R1 are apparently decreased. Moreover, we can see the hard X-ray peak around the complex moved near to IRS 9 (R2) from IRS 7 (R1). Thus X-rays from the flare source IRS 7 (R1) shows long-term decrease as is seen in Table 5.3, 5.2, and 5.1, which refers the PSF and vignetting corrected flux.

Table 5.3: Protostar candidates in R CrA region (AO6)

Name	RA (1950)	Dec (1950)	2–10 keV (cts ks^{-1} SIS^{-1})	Class
IRS 2=TS13.1	18 58 19	−37 2 50	45.3±2.2	I
IRS 5=TS2.4	18 58 25.5	−37 1 39	52.3±2.2	I
IRS 1=TS2.6	18 58 28.2	−37 2 29	44.3±2.0	I
IRS 7 + IRS 9[a]	(18 58 31.7	−37 1 31.5)	24.5±1.5	I
IRS 9=R2	18 58 30.7	−37 1 24		I
IRS 7=R1	18 58 32.7	−37 1 39		I

In the soft band (0.7–2 keV), all of the protostar candidates are contaminated by a bright T Tauri star CrA 1.

a: This region also includes Herbig Ae star R CrA: α(B1950) = 18h 58m 31.6s, δ(B1950) = -37° $01'$ $30''$.

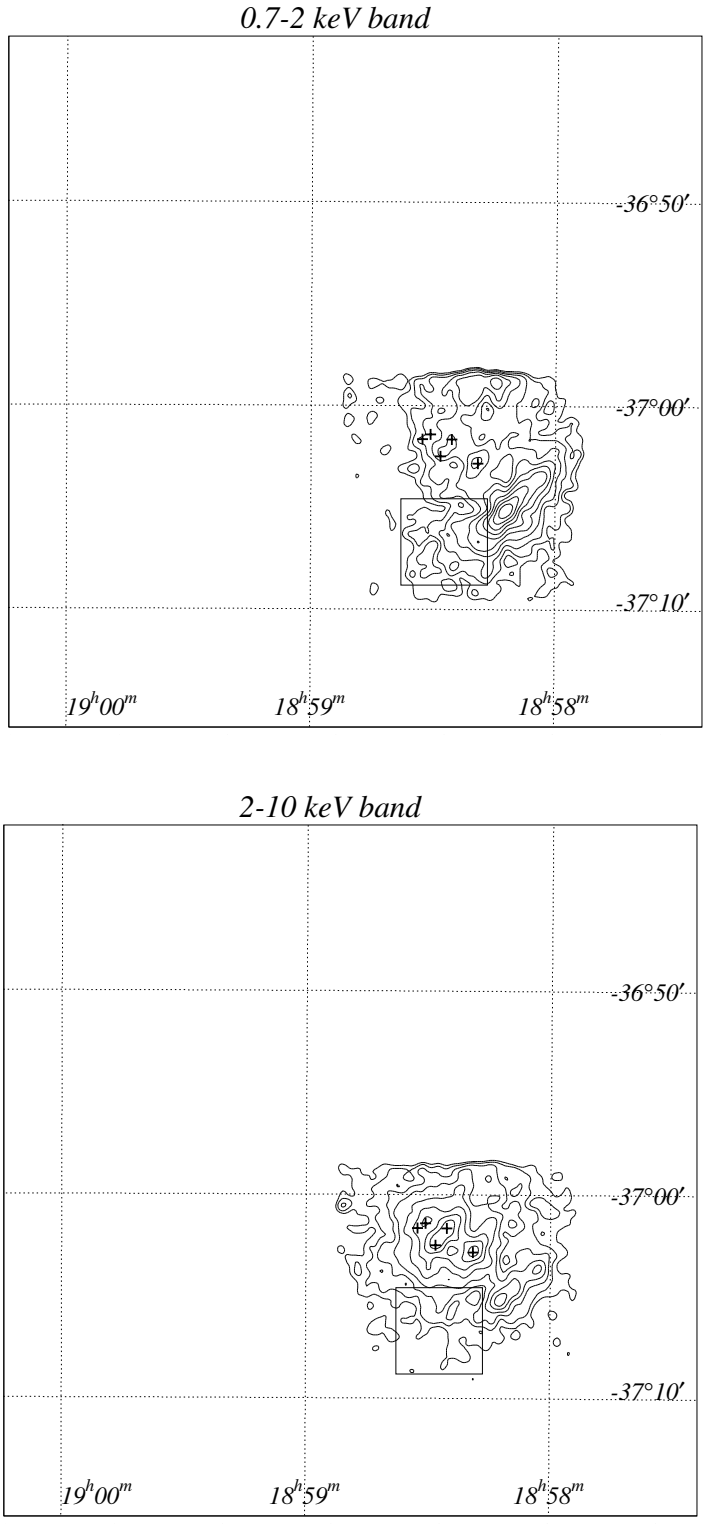

Figure 5.3: X-ray images of the R CrA cloud core (AO6), obtained with SISs. The contour levels for both of the band maps, in units of (10^{-3}counts/SIS/ks/pixel) are: 0.1, 0.2, 0.6, 1.3, 2.4, 4.0, 6.7, 10.9, 17.5, and 28.0 for the soft band, and are : 0.2, 0.4, 0.8, 1.5, 2.6, 4.2, 6.9, 11.1, 17.7, and 28.2 for the hard band.

Chapter 6

Taurus ($D = 140$ pc)

The Taurus dark cloud complex is one of the closest low mass star forming region, located at (l, b) = (170, -12) with a distance of 140 pc (Elias 1978c). Due to the reasonable angular distance from the Galactic plane, suitable declination, and proximity to the sun, the cloud complex has been extensively studied by near-infrared survey (e.g. Elias 1978c), far-infrared survey using *IRAS* satellite (e.g. Beichman et al. 1986), optical spectroscopy (e.g. Herbig, Vrba, & Rydgren 1986), and X-ray observations (e.g. Zickgraf et al. 1998). The complex contains many small dark clouds and numerous T Tauri stars (Cohen & Kuhi 1979), which indicate that the Taurus region is the recent star formation site.

The surveys by several molecular lines have revealed structures of different density gases. The most extensive ^{12}CO ($J = 1-0$) line observations, tracing gas with n(H_2) $\sim 10^2$ cm^{-3}, were made by Ungerechts & Thaddeus (1987). They covered the whole Taurus region and revealed the overall distribution of the molecular cloud. ^{13}CO observations, which trace gas with n(H_2) $\sim 10^3$ cm^{-3} were made by Mizuno et al. (1995). They observed $\sim$40 deg^2 with a grid spacing of 2′. C^{18}O ($J = 1-0$) observations, which trace gas with n(H_2) $\sim 10^4$ cm^{-3}, were carried out by Ohashi (1992), Hayashi et al. (1994), and Onishi et al. (1998).

Most of the YSOs in Taurus are found in the vicinity of molecular cores with typical mass of 1 $M_\odot$, densities of 10^4 to 10^5 cm^{-3}, temperatures of $\sim$10 K, and visual extinctions of 5 mag to 10 mag (Myers 1985, and references therein, Myers et al. 1987). Only 8 associated B stars are observed within a 12 pc projected radius of the cloud center (Elias 1978c, Walter & Boyd 1991), and there is no evidence for the formation of massive stars in the radio continuum search by Gimore

(1980). The molecular cores, and hence the YSOs, are distributed throughout a low-extinction, filamentary molecular complex covering about 2400 pc^2 (Ungerechts & Thaddeus 1987). These young stellar populations are the important differences between Taurus and Rho Oph in spite of both have similar mass of 3.5 $\times 10^4 M_\odot$ (Ungerechts & Thaddeus 1987) and the number of low-mass stars. The Rho Oph cloud lies in the Upper Scorpions subgroup of the Sco-Cen OB association, and has about 20 B or A0 stars within a four times smaller area (radius $\sim$6 pc), with the B2V star (HD 147889) and a B3–B5 V star (source 1) embedded in the western edge of the complex (Elias 1978c, De Geus et al. 1989). As a result, warmer dust and gas temperatures are observed in Rho Oph relative to Taurus (e.g. Greene & Young 1989, Jarrett et al. 1989, Snell et al. 1989).

In order to investigate the differences in X-rays between this cloud and the other near clouds (especially Rho Oph), we executed ASCA observations of this region.

6.1 B209 region (AO2)

ASCA observed the Barnard 209 dark cloud on February 16–17 1995. In this observation, large flare from V 773 Tau was detected. The report focused on the flare has been written by Tsuboi et al. (1998). In Figure 6.1, we show two energy-band X-ray images obtained with SISs. The X-ray data were extracted from pre-flare phase of V773 Tau (Tsuboi et al. 1997).

We see an X-ray enhancement around Class I source IRAS04108+2803B in the hard band, but it is only 4.0 σ level. Class II source CW Tau is hidden by the large emission from V 773 Tau (see Table 6.1).

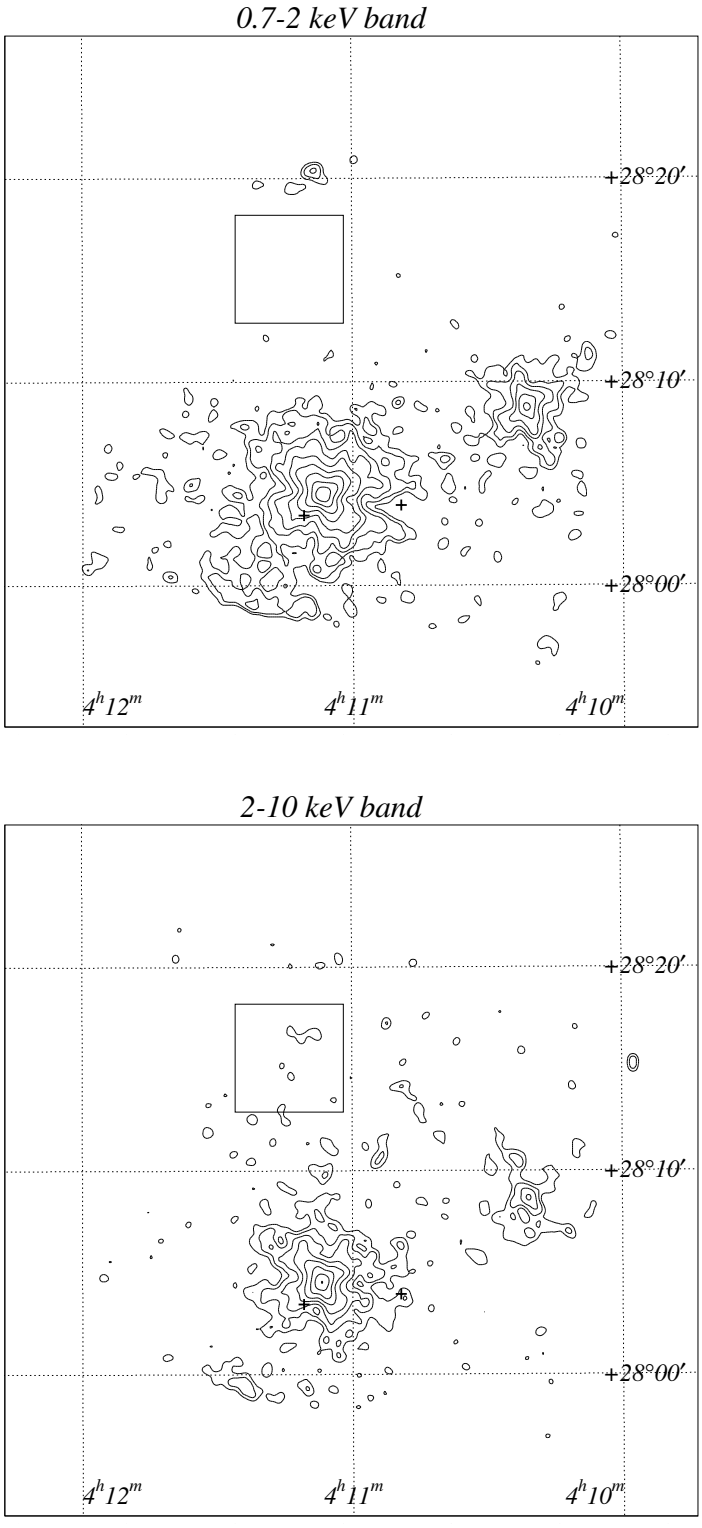

Figure 6.1: X-ray contour maps of B209 region (AO2), obtained with SISs. The contour levels in units of (10^{-3}counts/SIS/ks/pixel) are: 0.2, 0.4, 0.7, 1.2, 1.9, 3.1, 4.9, 7.9, and 12.5 for the soft band, 0.1, 0.3, 0.6, 1.1, 1.8, 3.0, 4.8, 7.8, and 12.4 for the hard band.

Table 6.1: Protostar candidates in B209 region (AO2)

Name	RA (1950)	Dec (1950)	0.7–2 keV (cts ks^{-1} SIS^{-1})	2–10 keV (cts ks^{-1} S IS^{-1})	Class
IRAS04108+2803B	4 10 49.3	+28 3 57	$\leq$2.5	$\leq$5.7	I
CW Tau	4 11 10.9	+28 3 27	—[a]	—[a]	II[†]

†: Prusti et al. 1992

a: contaminated by V773 Tau.

6.2 B209 (AO3, the 1st day)

ASCA observed the Barnard 209 dark cloud on Sep 16–17 1995. In this observation, another large flare from V 773 Tau was detected. The report mainly on the flare has been written by Skinner et al. (1997). In Figure 6.2, we show two energy-band contour maps obtained with SISs, together with protostar candidates indicated by crosses.

Due to the large flare from V 773 Tau (Skinner et al. 1997), IRAS04108+2803B and CW Tau are not found. We see no significant X-ray from IRAS04113+2758, neither (see Table 6.2).

Table 6.2: Protostar candidates in B209 region (AO3, the first day)

Name	RA (1950)	Dec (1950)	0.7–2 keV (cts ks^{-1} SIS^{-1})	2–10 keV (cts ks^{-1} S IS^{-1})	Class
IRAS04108+2803B	4 10 49.3	+28 3 57	—[a]	—[a]	I
IRAS04113+2758	4 11 20.9	+27 58 30	—[a]	$\leq$7.9	II
CW Tau	4 11 10.9	+28 3 27	—[a]	—[a]	II[†]

†: Prusti et al. 1992

a: contaminated by V773 Tau.

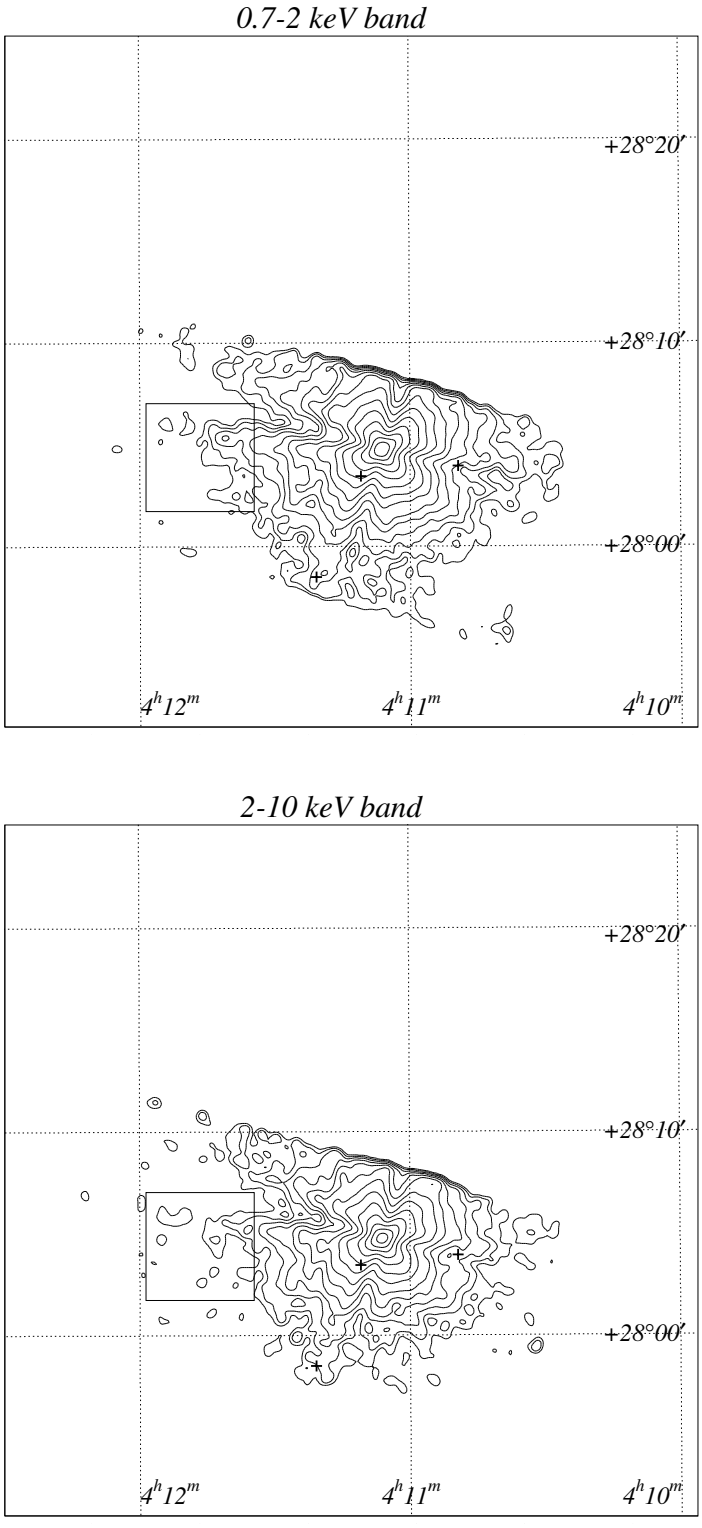

Figure 6.2: X-ray images of B209 region (AO3, 1st day), obtained with SISs. The contour levels in units of (10^{-3}counts/SIS/ks/pixel), are : -0.1, 0.1, 0.4, 0.9, 1.6, 2.8, 4.6, 7.6, 12.2, 19.6, 31.3, 49.8, and 79.2, for the soft band, and 0.0, 0.2, 0.5, 1.0, 1.7, 2.9, 4.6, 7.7, 12.3, 19.7, 31.4, 49.9, and 79.3 for the hard band.

6.3 B209 (AO3, the 2nd day)

ASCA observed the Barnard 209 dark cloud on Feb 13 1996. In Figure 6.3, we show two energy-band X-ray images obtained with SISs.

We see X-ray enhancement around Class I source IRAS04108+2803B again, but it is only 4.6σ level. We detected no significant X-ray from Class II source CW Tau.

Table 6.3: Protostar candidates in B209 (AO3, the second day)

Name	RA (1950)	Dec (1950)	0.7–2 keV (cts ks^{-1} SIS^{-1})	2–10 keV (cts ks^{-1} S IS^{-1})	Class
IRAS04108+2803B	4 10 49.3	+28 3 57	$\leq$0.6	$\leq$4.1	I
CW Tau	4 11 10.9	+28 3 27	—^{a}	—^{a}	II†

†: Prusti et al. 1992

a: contaminated by V773 Tau.

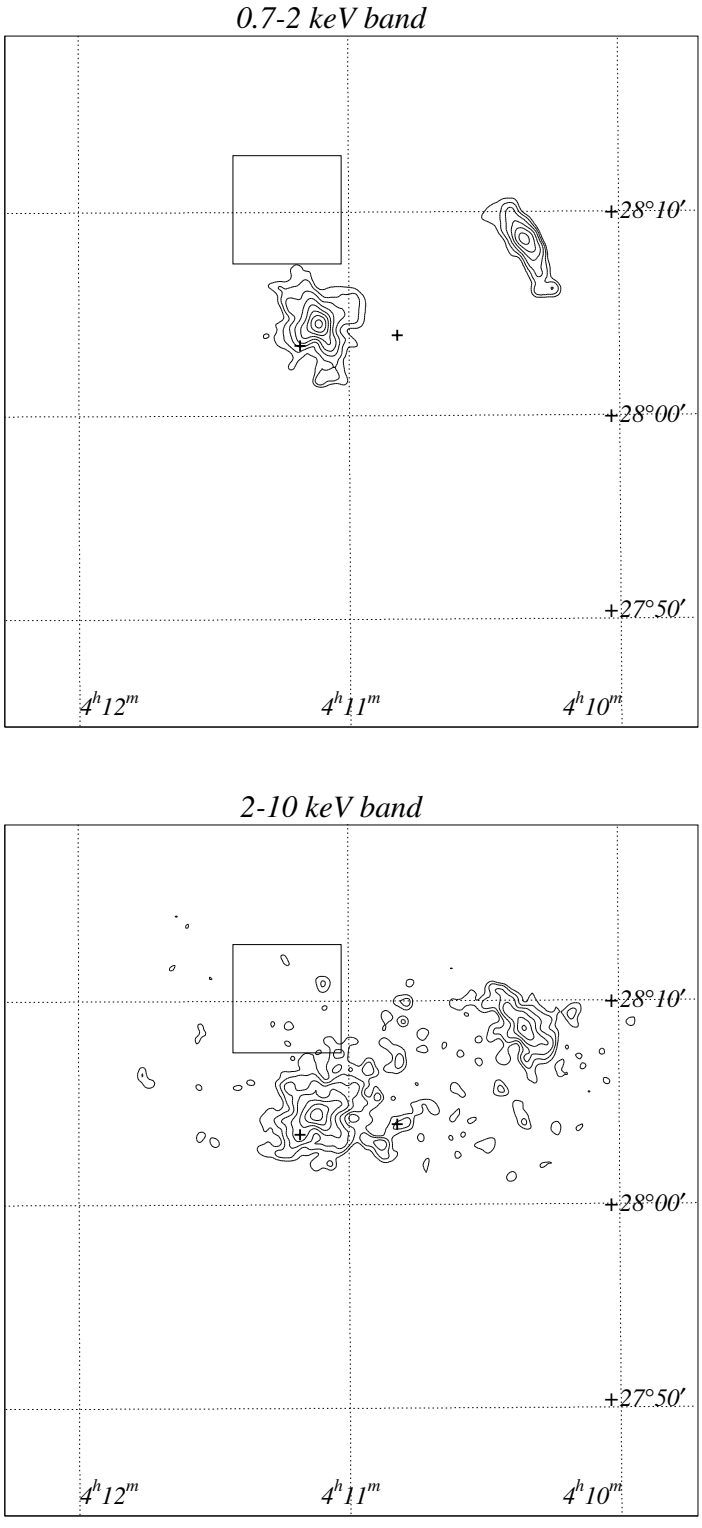

Figure 6.3: X-ray images of B209 region (AO3, 2nd day), obtained with SISs. The contour levels for both of the band maps, in units of (10^{-3}counts/SIS/ks/pixel), are : 0.2, 0.3, 0.7, 1.2, 1.9, 3.1, 4.9, and 7.9.

6.4 TMC1

ASCA observed the TMC1 region on Feb 13 1996. In Figure 6.4, we show two energy-band contour maps obtained with SISs.

We detected no significant X-ray from the protostar candidates.

Table 6.4: Protostar candidates in TMC1 region

Name	RA (1950)	Dec (1950)	0.7–2 keV (cts ks^{-1} SIS^{-1})	2–10 keV (cts ks^{-1} S IS^{-1})	Class
IRAS04361+2547	4 36 9.4	+25 47 27	$\leq$0.2	$\leq$0.3	I
IRAS04365+2535	4 36 31.0	+25 35 52	$\leq$0.5	$\leq$0.98	I
IRAS04368+2557	4 36 49.5	+25 57 16	$\leq$0.2	$\leq$0.3	0
IRAS04369+2539	4 36 54.6	+25 39 17	—^{a}	—^{a}	II†

†: Kenyon et al. 1990

a: contaminated by B5 star IC2087

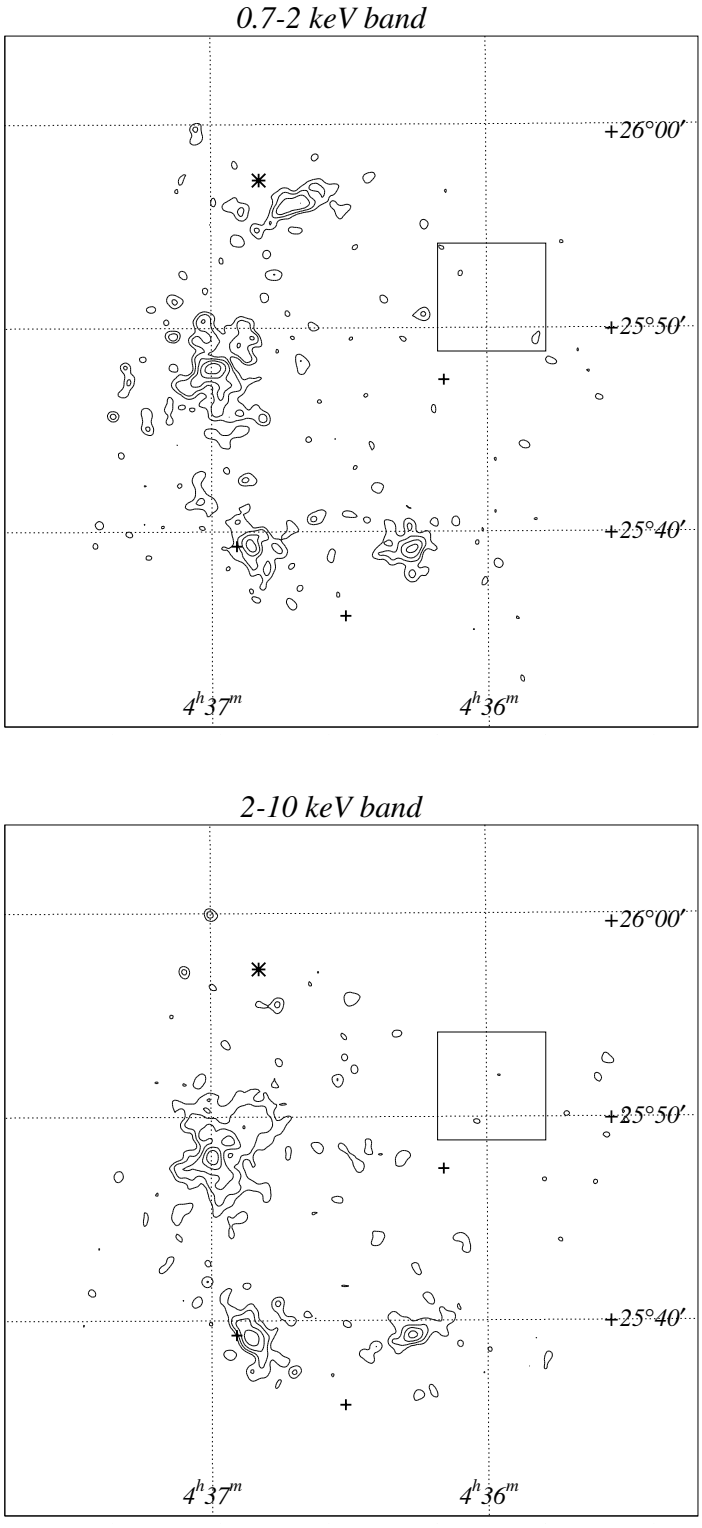

Figure 6.4: X-ray images of TMC1 region, obtained with SISs. The contour levels, in units of (10^{-3}counts/SIS/ks/pixel), are: 0.1, 0.2, 0.3, 0.4, 0.7, and 1.1 for the soft band, 0.1, 0.2, 0.3, 0.5, and 0.9 for the hard band.

6.5 IC359

ASCA observed the IC359 region on September 2–3 1995. In Figure 6.5, we show the two energy-band X-ray images obtained with SISs.

IRAS04154+2823 and CoKu Tau-1 are contaminated by WTTS V410 Tau and WTTS Hubble 4, respectively.

Table 6.5: Protostar candidates in IC359 region

Name	RA (1950)	Dec (1950)	0.7–2 keV (cts ks^{-1} SIS^{-1})	2–10 keV (cts ks^{-1} S IS^{-1})	Class	ref
IRAS04154+2823	4 15 25.6	+28 23 59	—^{a}	—^{a}	I	
CoKu Tau-1	4 15 45.46	+28 13 14	—^{b}	—^{b}		1

Reference for the coordinate – (1) Strom & Strom 1994

a: contaminated by Weak line T Tauri star V410 Tau. *b*: contaminated by Weak line T Tauri star Hubble 4.

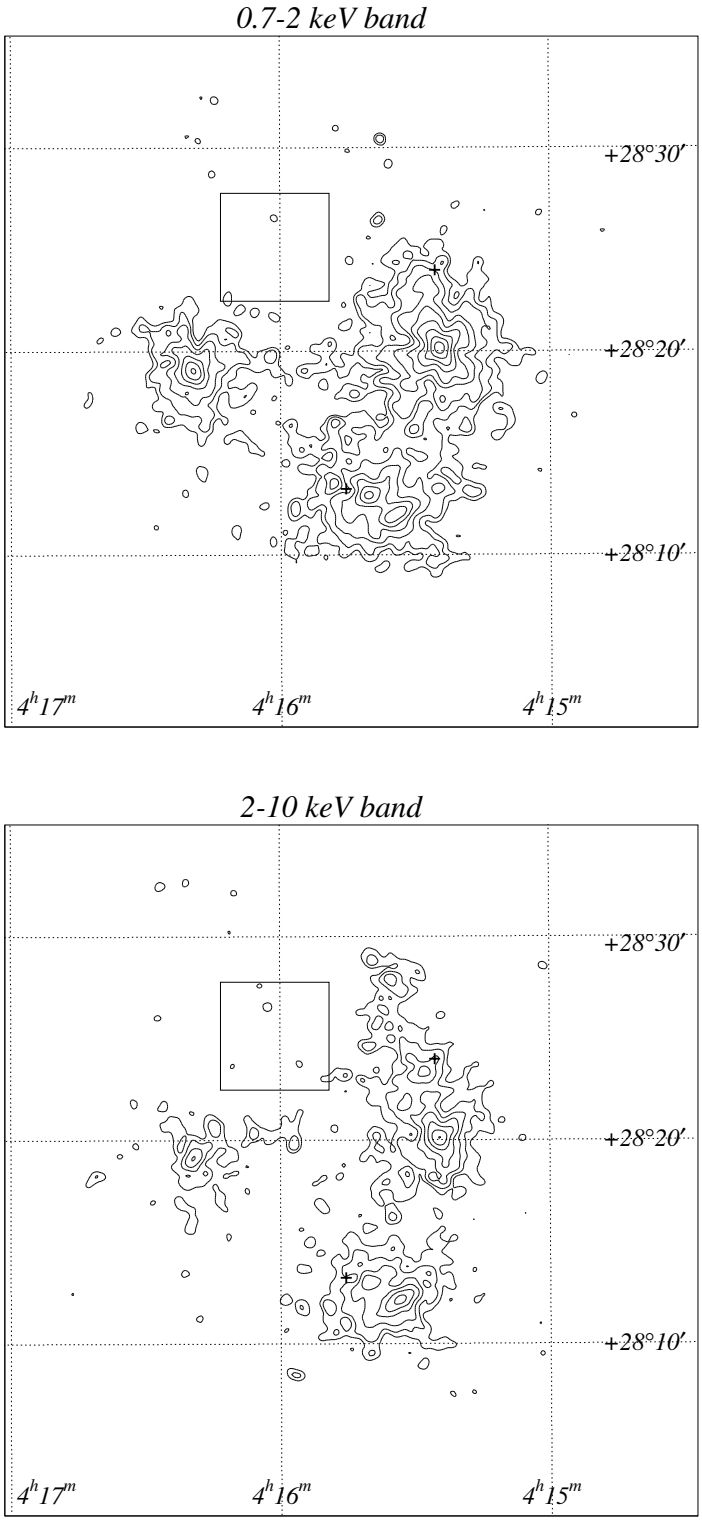

Figure 6.5: X-ray images of IC359 region, obtained with SISs. The contour levels for both of the band maps, in units of (10^{-3}counts/SIS/ks/pixel), are : 0.1, 0.3, 0.5, 0.8, 1.4, 2.3, 3.7, 5.9, 9.4, and 14.9, from the lower level.

6.6 L1551

ASCA observed the L1551 region on February 23–24 1994. The comprehensive report has been represented by Carkner et al. (1993). In Figure 6.6, we show the two energy-band X-ray images obtained with SISs.

We detected no significant X-ray from protostars.

Table 6.6: Protostar candidates in L1551 region

Name	RA (1950)	Dec (1950)	0.7–2 keV (cts ks^{-1} SIS^{-1})	2–10 keV (cts ks^{-1} SIS^{-1})	Class	ref
L1551IRS5	4 28 40.2	+18 1 41.3	$\leq$0.78	$\leq$0.87	I	
HLTau	4 28 44.4	+18 7 36.2	—[a]	—[a]	II	
L1551NE	4 28 50.8	+18 2 10.8	$\leq$0.28	$\leq$0.89	I	
HH30IRS	4 28 43.3	+18 6 02	—[a]	—[a]		1

Reference for the coordinate – (1) Carkner et al. 1998

a: contaminated by Classical T Tauri star XZ Tau.

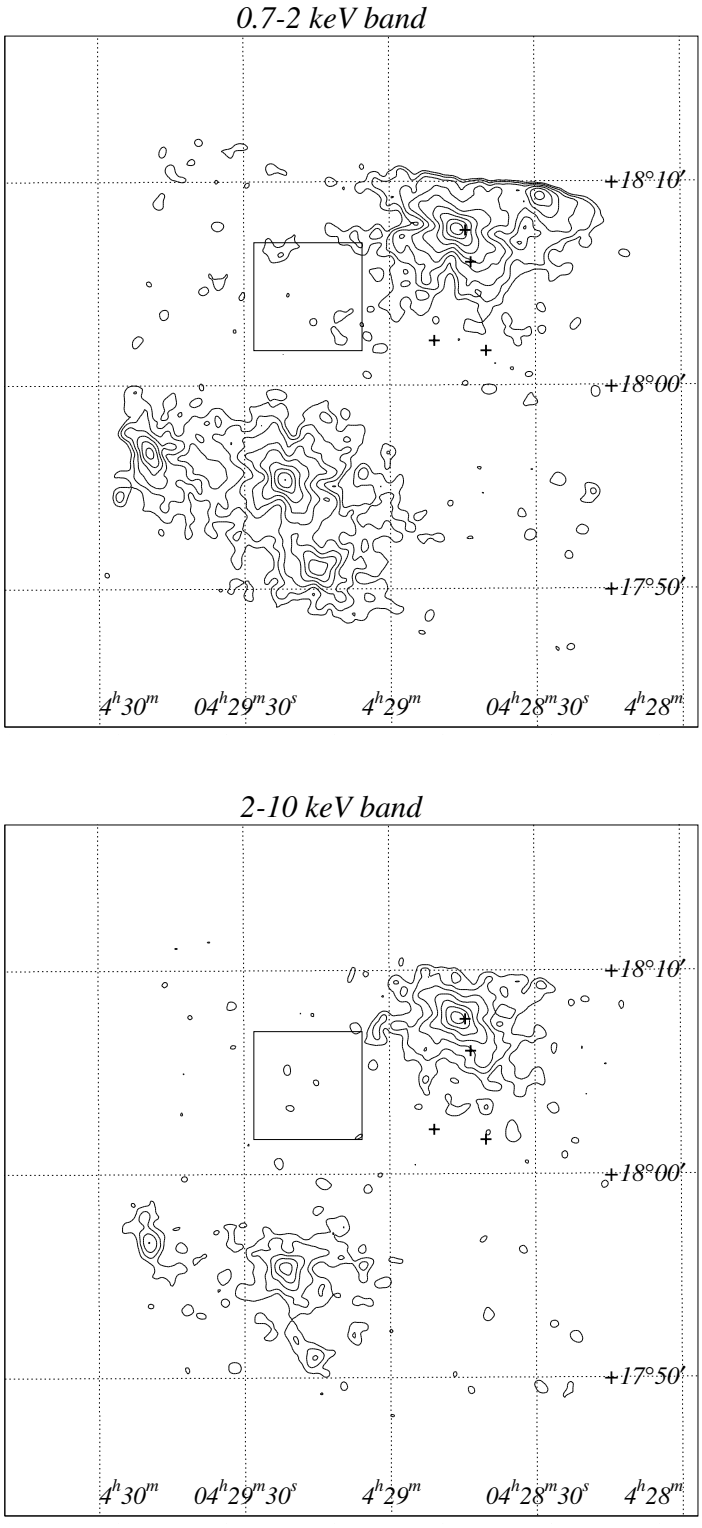

Figure 6.6: X-ray images of the L1551 region, obtained with SISs. The contour levels for both of the band maps, in units of (10^{-3}counts/SIS/ks/pixel), are : 0.1, 0.3, 0.5, 0.8, 1.4, 2.3, 3.7, 5.9, and 9.4.

Chapter 7

Lupus ($D = 140$ pc)

The Lupus dark cloud is located at the distance of 140 pc, which is derived by photometries of the field stars in Lupus (Huges et al. 1993), and then one of the most nearby low mass star forming region. The cloud is near the Sco OB association and extends within $l \sim 335° - 348°$ and $b \sim 0° - 25°$ consisting of four subgroups designated to be Lupus 1 (B228), 2, 3 and 4.

Since the Lupus cloud is located in the southern sky of $\sim -30°$ in declination, this cloud draw only a little attention until 1980's. However, recently improved observing facilities in the southern hemisphere leads to many extensive investigations with optical (e.g. Huges et al. 1994) infrared (e.g. Huges et al. 1992), and radio (e.g. Tachihara et al. 1996) wavelengths. On the other hand, X-ray observations (e.g. Krautter et al. 1997) increased the population of the Weak line T Tauri stars in the cloud surroundings, which are less obscured regions.

The Lupus cloud has some similarities to the Taurus and Chamaeleon clouds; it consists of low mass stars and no OB star, many famous T association exists (70 or more), and total mass of the molecular cloud ($3 \times 10^4 M_\odot$: Krautter 1991) is nearly the same as that of the Taurus dark cloud ($3.5 \times 10^4 M_\odot$: Ungerechts and Thaddeus 1987). However, in the Lupus dark cloud, M stars (i.e., M $\leq$ 0.5 $M_\odot$) are formed selectively (Krautter and Kelemen 1987, Appenzeller et al. 1983) compared with the other star forming region. Strom et al. (1988) and Krautter (1991) proposed that the abnormal star mass distribution in the cloud is due to a sub-critical star formation.

Lupus 1 is a part of extremely thick molecular cloud B228, and shows a filamentary structure with the major axis perpendicular to the Galactic plane. The total

mass is estimated to be $\sim$ 3600 $M_\odot$. Thirteen YSOs are associated in this molecular cloud. The optical polarization vectors (Strom et al. 1988) indicates that the magnetic field lines lie perpendicular to the filament. From the IRAS point source 15398−3359 associated with this molecular cloud, molecular outflow is discovered for the first time in the Lupus cloud (Tachihara et al. 1996). On the other hand, Heyer and Graham (1989) discovered shock excited nebulosity near this object. Thus the nebulosity would be due to the excitation by the outflow from the central core. The authors proposed that the molecular outflow may be physically related to HH 185. The dynamical age of the outflow is estimated as $\sim$2000 yr, suggesting that star formation is on-going, because the molecular outflow would be associated with low-mass protostars (e.g. Fukui et al. 1993).

The Lupus 2 dark cloud is a small molecular cloud of $\sim$400 $M_\odot$. A Herbig Haro object HH55 and a luminous T Tauri star RU Lup are associated near the peak of the integrated flux of ^{13}CO. However, no molecular outflow has been found from this cloud (see Gahm et al. 1993).

The Lupus 3 dark cloud has a mass of $\sim$1000 $M_\odot$. The line profiles of this cloud indicate the presence of a few components with different velocity The magnetic field line is perpendicular to the filament (Myers & Goodman 1991). T Tauri stars associated with this cloud are low-mass ($\leq$0.5 $M_\odot$). Most of them have ages of $\sim 10^7$ yr, older than those in Lupus 1 and 2 (Huges et al. 1994).

A cloud of ring-like structure with a velocity gradient along the ring was discovered by Tachihara et al. (1996), and is designated as Lupus 5. The peak velocity changes from 3.5 km s^{-1} at the south-west side of the ring to 6.0 km s^{-1} at the south-east side. No optical source has been cataloged in the literature so far. The total mass is estimated to be $\sim$2100 $M_\odot$ (Tachihara et al. 1996).

7.1 Lupus3

We observed the center of the Lupus 3 dark cloud on February 2–4 1996. We show the two energy-band X-ray images obtained with SISs, together with protostar candidates in Figure 7.1.

Th28 is an optically visible star, but has a group of HH flows and highly opaque disk-like material (Krautter 1991). In this observation, the Th28 is buried by the strong emission around HD144667 and CD-38 10894B, and no excess is seen in

both the X-ray band maps.

Table 7.1: Protostar candidates in the Lupus 3 region

Name	RA (1950)	Dec (1950)	0.7–2 keV (cts ks^{-1} SIS^{-1})	2–10 keV (cts ks^{-1} SIS^{-1})	Class	ref
Th28	16 5 8.3	−38 55 16	—[a]	—[a]		1

Reference to the coordinate – (1) Tachihara et al. 1996

a: contaminated by HD144667 or CD-38 10894B.

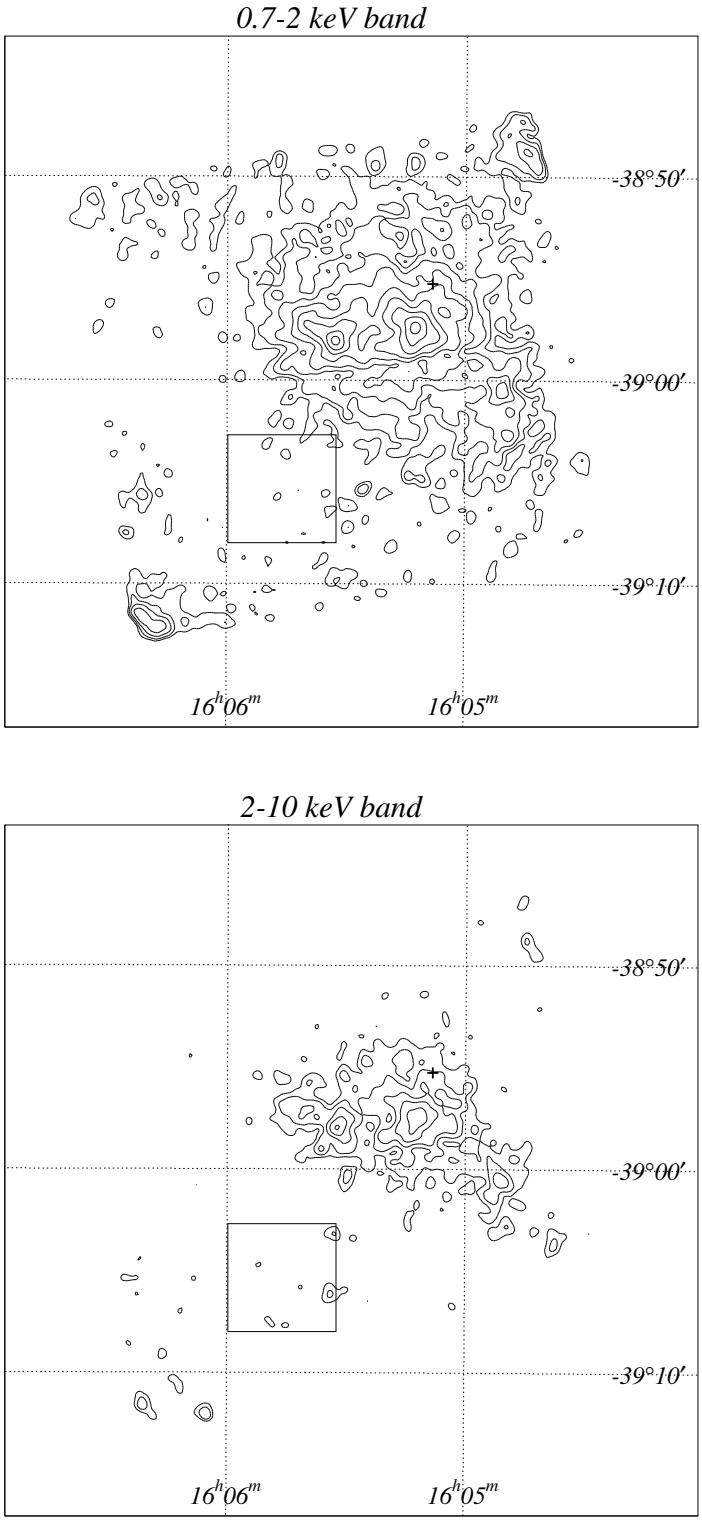

Figure 7.1: X-ray images of the Lupus 3 region, obtained with SISs. The contour levels for both of the band maps, in units of (10^{-3}counts/SIS/ks/pixel), are : 0.1, 0.3, 0.5, 0.8, 1.4, 2.3, 3.7, 5.9, and 9.4.

Chapter 8

Serpens ($D = 310$ pc)

The Serpens dark cloud is a nearby ($d = 310$ pc; de Lara et al. 1991), very active star forming region (for a review see Eiroa 1991), located at (l, b) = (32, +5), and extending about $1^\circ \times 2^\circ$.

The Serpens dark cloud was first recognized as a potential site of star formation through the identification of embedded IR objects and associated reflection nebulae (Strom et al. 1974, 1976). The core of the cloud was first found in the NH_3 map, which shows two dense condensations separated by $3'$ (Ungerechts & Güsten 1984). One of the condensations is located to the south-east of the Serpens Reflection Nebula (SRN) and the other is to the north-west. The recent submillimeter and radio observations revealed much smaller structures; seven condensations in the core region. Five of the seven peaks have characteristics of Class 0 protostars (Casali et al. 1993, McMullin et al. 1994, White et al. 1995, Hurt et al. 1996, Hurt & Barsony 1996). The Serpens cloud shows further signatures for an early phase of star formation: Herbig Haro objects (Reipurth & Eiroa 1992) and molecular outflows (Eiroa et al. 1992).

On the other hand, after the early detection of 20 infrared sources by Strom et al. (1976), recent infrared imaging surveys by Eiroa & Casali (1992) and Giovannetti et al. (1998) have revealed the presence of more than 150 near-infrared (NIR) sources in this region. Some 50 of these objects are most probably associated to the cloud, but a large fraction of them have no optical counterpart. The optically invisible source 4 of Strom et al. (1976) (SVS 4, hereafter) could be resolved into a small cluster of at least 11 individual NIR sources by Eiroa & Casali (1989). These sources are surrounded by nebulosity, show extremely red color, and exhibit

a moderate NIR excess. Thus, they are believed to be YSOs deeply embedded in the molecular cloud core. With a stellar mass density of $\approx 10^5$ $M_\odot$ pc^{-3}, SVS 4 constitutes one of the densest clusterings of YSOs (Eiroa & Casali 1989).

Recently, Preibisch (1998) detected strong X-ray emission from an optically invisible infrared source EC95, which is deeply embedded ($A_V \approx 34$ mag) in the SVS 4. The quiescent, i.e. non-flaring, soft X-ray luminosity is about (6–18) $\times$ 10^{32} erg s^{-1}, ranking this source to be the most X-ray luminous YSO ever detected.

8.1 Core region

We observed the central region of the Serpens cloud on April 15–16 1997. We show the two energy-band X-ray images obtained with SISs together with protostars indicated by asterisks (Class 0) and a cross (FU Ori) in Figure 8.1.

We detected no significant X-ray from low-mass protostars, SMM 1, 2, 3, 4, 9, and the FU Ori (see Table 8.1). However, we detected intense X-rays from the EC95 (source 3; Preibisch 1998) in both soft and hard band. Preibisch (1998) proposed that EC95 is a very young object, probably not older than a few 10^5 yrs ($\sim$ Class I), while Giovannetti et al. (1998) reported that the source has a small NIR excess. From NIR spectrum, the mass of EC95 is estimated to be 2–3 $M_\odot$, hence would be a "proto-Herbig Ae/Be star" (Preibisch private communication).

In addition to the X-rays from EC 95, we detected unidentified source in the north direction from the HRI source 2, but we here concentrate on the X-rays from EC 95.

8.1.1 EC95

Lightcurve

We accumulated X-ray photons from EC95 by co-adding the SIS0 + 1, GIS 2 + 3 events in a $3'$ radius circle around the source. For the background, we used the events from an annulus with $5'$ inner radius and $8'$ outer radius centered on EC95. We excluded the events within the $2'$ radius circles around the source 2 of Preibisch 1998 from the background. The background subtracted light-curve of EC95 in the 2–10 keV band is shown in Figure 8.2. This light curve shows no strong flare event but rather small amplitude flux variability. In fact, fitting with constant flux model

is rejected with $\chi^2/d.o.f. = 174.2/92$. This variability would be due to integrated emissions of many small flares.

Spectrum

We accumulated each of the data and background from the same regions as those used in the timing analysis. The background subtracted spectrum with the best-fit thin thermal model and their parameters are given in Figure 8.3 and Table 8.2, respectively. We found that the EC95 has rather high temperature of about 5 keV, which is higher than the typical temperature of YSOs in quiescent state, and than the assumed temperature (1–3 keV) by Preibisch (1998). The temperature of the thin thermal plasma is mainly determined from the energy of exponential fall-off (Rybichi & Lightman 1979). In our case, the energy ($\sim$ 5 keV) is included in the hard X-ray band which is almost free from absorption and free from contamination of most of the soft X-ray sources (see Figure 8.1). Therefore we can conclude our derived temperature and emission measure are reliable. The best-fit absorption of $N_H \sim 2 \times 10^{22}$ cm^{-2} is much smaller than $N_H \sim 8 \times 10^{22}$ cm^{-2}, the value estimated from NIR data (Preibisch 1998). The intrinsic X-ray luminosity in the total X-ray band (0.1–100 keV) is 6×10^{31} ergs s^{-1}, which is 1–2 order of magnitude smaller than that derived by Preibisch (1998). These apparent discrepancies can be explained by the difference between the assumed spectral parameters (temperature and absorption) in Preibisch (1998) and our best-fit parameters, i.e., there is no flux change in the ROSAT band. Our derived X-ray luminosity is still larger than typical luminosities ($\sim 10^{30}$ ergs s^{-1}) in the quiescent state of YSOs.

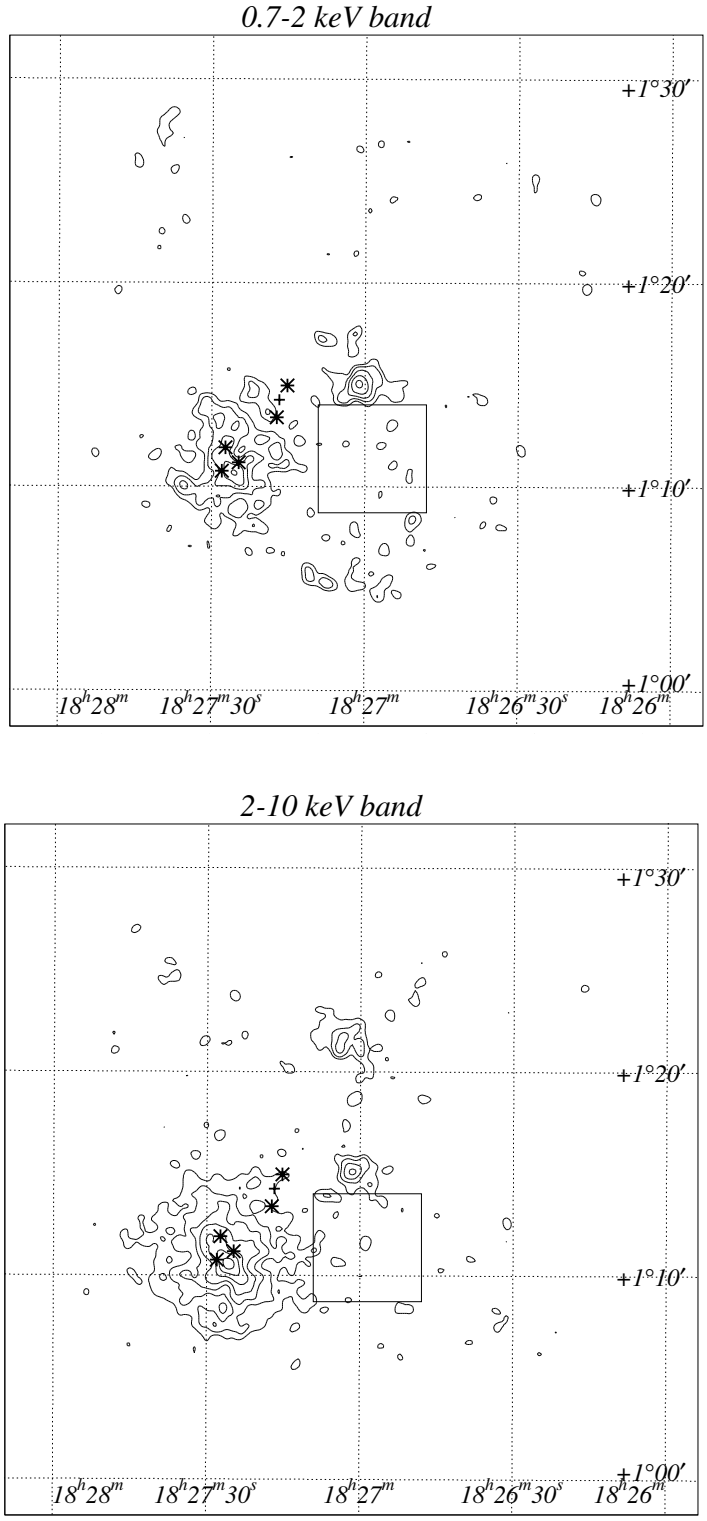

Figure 8.1: X-ray images of the Serpens cloud main body, obtained with SISs. The contour levels for both the bands, in units of (10^{-3}counts/SIS/ks/pixel) are : 2.8, 4.4, 7.1, 11.3, 17.9, 28.4, and 45.1.

Table 8.1: Protostar candidates in Serpens Core

Name	RA (1950)	Dec (1950)	0.7–2 keV (cts ks^{-1} SIS^{-1})	2–10 keV (cts ks^{-1} SIS^{-1})	Class
SMM9=S68N	18 27 15.2	+1 14 57	$\leq$0.2	$\leq$1.4	0
SMM1=FIRS1	18 27 17.3	+1 13 23	$\leq$1.4	$\leq$2.2	0
SMM3	18 27 27.3	+1 11 55	—[a]	—[a]	0
SMM4	18 27 24.7	+1 11 10	—[a]	—[a]	0
SMM2	18 27 28.0	+1 10 45	—[a]	—[a]	0
FUOri	18 27 16.8	+1 14 15	$\leq$1.4	—[a]	0 or I
EC95	18 27 25.6	+1 10 42			I?

a: contaminated by X-ray from EC 95 (see text).

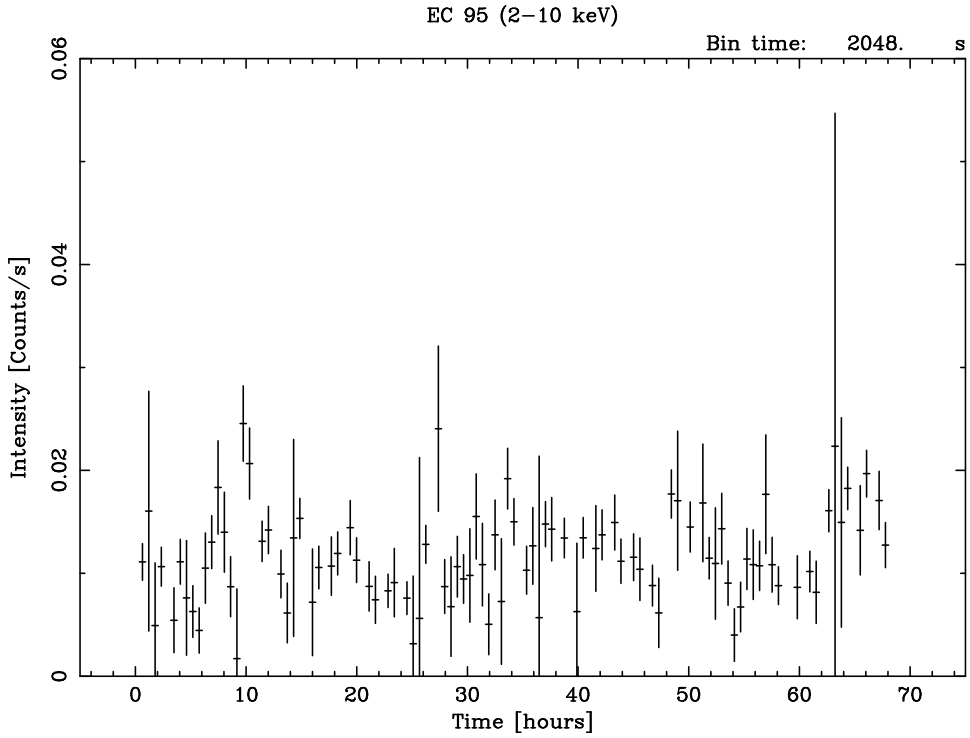

Figure 8.2: The lightcurve of EC95 in 2–10 keV band. All the SIS data and GIS data are averaged, and background is subtracted.

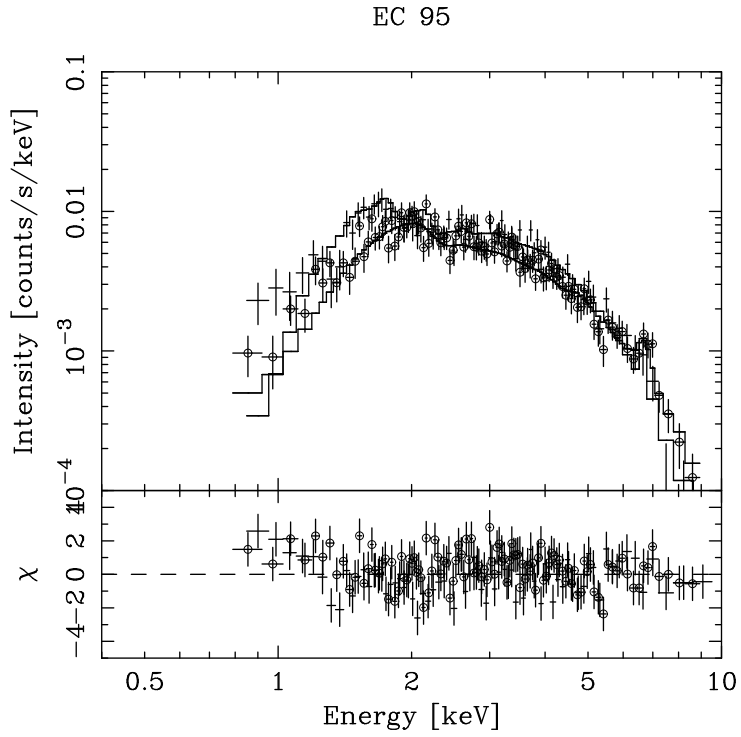

Figure 8.3: The SIS (cross: SIS 0 and 1, averaged) and GIS (open circle: GIS 2 and 3, averaged) spectra of X-ray spectrum of EC95. The solid lines show the best-fit one-temperature coronal plasma model. Lower panel shows the residuals from the best-fit model.

Table 8.2: Best-fit parameters to spectrum of EC95.

Name	kT (keV)	Abundance (solar)	EM^a (10^{54}cm^{-3})	$N_{\rm H}$ (10^{22}cm^{-2})	$L_{\rm X}{}^b$ (10^{31}ergs s^{-1})	$\chi^2/d.o.f$
EC 95	$4.6^{+0.7}_{-0.6}$	0.2±0.1	3.4±0.3	$2.0^{+0.2}_{-0.1}$	6	221.6/184

The errors are at 90% confidence level. The distance of CR95 is assumed to be 310 pc.

[a] Volume Emission Measure.

[b] Absorption-corrected X-ray luminosity in the 0.1 – 100 keV band.

Chapter 9

Perseus (D = 200–350 pc)

The Perseus molecular complex is a conglomeration of regions of high visual extinction extending over some 9 by 9 degrees at a Galactic longitude of $\sim$160° and latitude $\sim -19°$. Its high Galactic longitude and its low local sidereal time (LST) velocity determined from CO (Sargent 1979) and ^{13}CO (Bachiller & Cenicharo 1986) suggest that it is within a few hundred parsecs from the sun. After the several debates for the distance, the current consensus is that the NGC 1333 cloud lies between 220 pc (Cernis 1990) and 350 pc (Borgman & Bllauw 1990), the value adopted by most of the authors.

The Perseus complex lies $\sim$10° away from Taurus. The spatial distance between the Perseus and Taurus complex is probably 100–200 pc (the uncertainty is mainly due to the inaccurate determination of the Perseus distance). From an extensive survey of this complex in several molecular lines and star counts, Bachiller & Cernicharo (1986) showed that the molecular cores in Perseus have densities and temperatures similar to those of the Taurus clumps.

The Perseus complex contains two active sites of star formation, IC348 and NGC1333, connected by a chain of colder dark clouds (e.g. B1, B1E) with strong molecular emission. These two active regions contain newly-formed intermediate-mass stars of spectral type B, as well as a cluster of low mass YSOs.

9.1 NGC1333

The NGC1333 star forming region has been extensively studied in the millimeter and centimeter molecular lines and in the IR continuum emission. The mass was

derived to be $10^3 M_\odot$ by Lada et al. (1974).

Several far infrared sources within the NGC1333 region are listed in the IRAS Point Source Catalog. Harvey et al. (1984) and Jennings et al. (1987) performed more sensitive far infrared surveys and detected a number of compact dust cores. In some of these cores, especially in IRAS 1 (see Knee et al. 1990), IRAS 2 (see Ward-Thompson et al. 1996), IRAS 4 (see Sandell et al. 1991), many protostar candidates have been found.

In X-ray wavelength, Preibisch (1996) executed a deep ROSAT HRI observation of this region, and detected 20 sources, 16 of which were assumed to be the members of the cluster of pre-main sequence stars. They detected X-rays from a Class I source SVS16 with the X-ray luminosity of 2.8×10^{32} erg s^{-1}.

We executed observations of the NGC1333 dark cloud on 1995 August 30 – September 2. We show the two energy-band X-ray images obtained with SISs, together with protostars in Figure 9.1. Around a protostar candidate SVS12, which is optically visible, we detected diffuse X-ray emission in both the soft and hard bands . However, we detected no significant X-ray from the other protostar candidates.

Table 9.1: Protostar candidates in NGC1333

Name	RA (1950)	Dec (1950)	0.7–2 keV (cts ks^{-1} SIS^{-1})	2–10 keV (cts ks^{-1} SIS^{-1})	Class	ref
NGC1333IRAS2	03 25 49.9	+31 04 16	—^{a}	—^{a}	0	
NGC1333IRAS4A	03 26 04.8	+31 03 13	—^{a}	$\leq$2.0	0	
NGC1333IRAS4B	03 26 06.5	+31 02 51	—^{a}	$\leq$1.4	0	
SVS12	03 25 55.4	+31 10 05	3.6$\pm$0.5^b	2.1$\pm$0.4^b		1

Reference for the coordinate – (1) Morinari et al. 1993

a: contaminated with SVS19

b: not point like but diffuse emission

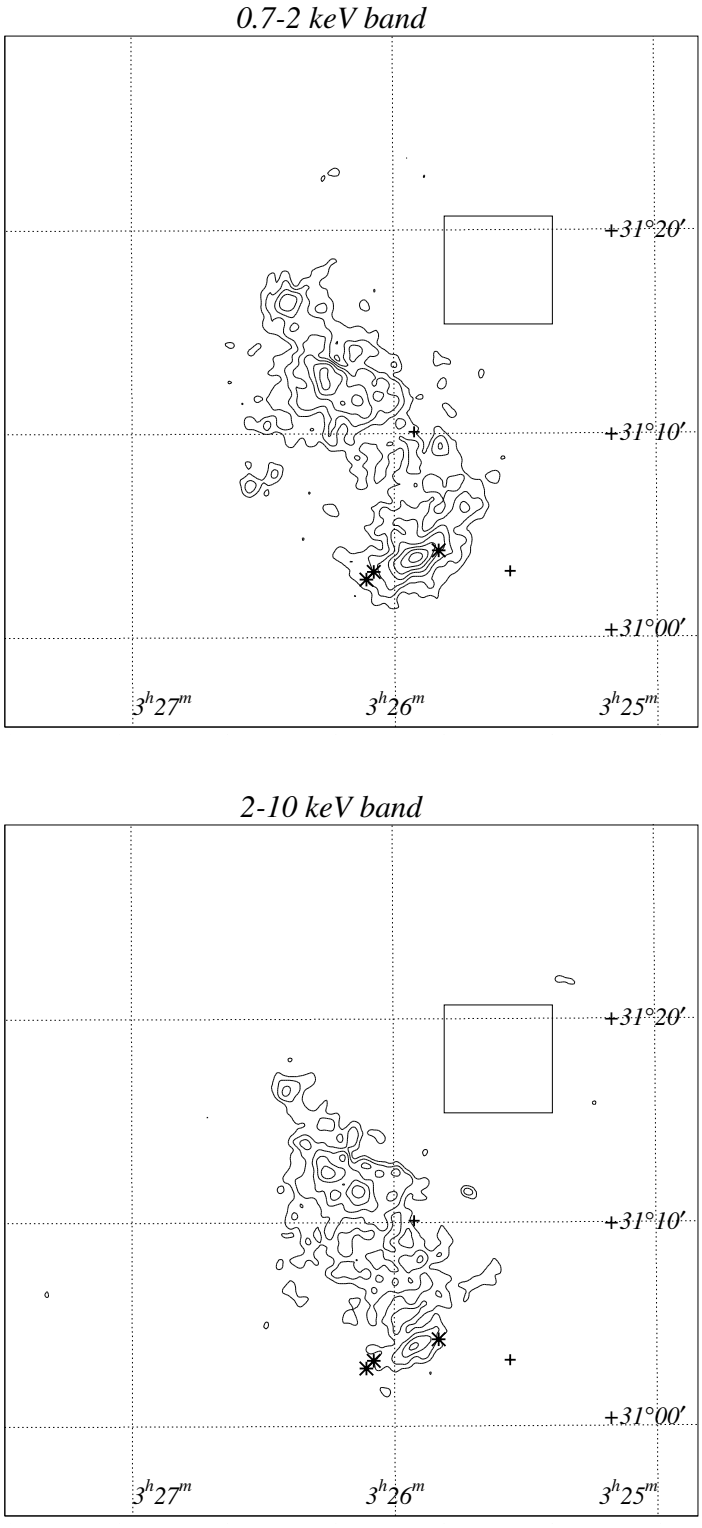

Figure 9.1: X-ray contour maps of the NGC1333 cloud core, obtained with SISs. The contour levels for both of the band maps, in units of (10^{-3}counts/SIS/ks/pixel), are : 0.1, 0.2, 0.3, 0.5, 0.7, 1.0, and 1.4.

9.2 L1448

L 1448 is a dense globule located $\sim 1^\circ$ south-west from NGC 1333 at a distance of about 300 pc (Cernis 1990, Herbig & Jones 1983).

This dark globule was well determined in the ^{13}CO and ($J = 1 - 0$) moderate resolution maps carried out with the Bordeaux radio telescope (Bachiller and Cernicharo 1986a). The NH_3 (1, 1) and (2, 2) maps of L 1448 with $\sim 1'.5$ resolution were presented by Bachiller and Cernicharo (1986b). These observations showed the existence of a dense core of about 50 $M_\odot$ with a kinetic temperature $T_K = (12 \pm 1)$ K and central density n(H_2) $\sim$ a few 10^4 cm^{-3}.

L 1448 contains at least four young stellar objects (YSOs). IRAS 03220+3035 (L1448 IRS 1) is a Class II YSO associated with a red reflection nebula RNO 13 (Cohen 1980). Ladd et al. (1993) estimated that the luminosity in the 2.2–35 μm range (the K_{135} luminosity) is about 5 $L_\odot$. Levreault (1988) found a low-velocity outflow with blue-shifted molecular gas extending east of the infrared source. IRAS 03222 + 3034 (L 1448 IRS 2) is an embedded object located several arc-minutes to the east of IRS 1. It has K_{135} luminosity of about 8 $L_\odot$. The SED shows steep rise toward the low frequency side, hence is most likely from a Class 0 YSO. IRAS 03225 + 3034 (L1448 IRS 3) is a Class I YSO that lies at the peak of the ^{13}CO emission from the L 1448 cloud core. It is associated with a small reflection nebula, an H_2O maser, and is a compact source in the radio (centimeter wavelength) continuum, with K_{135} luminosity of about 18 $L_\odot$. This source had been regarded as the driving source of the molecular outflow found in L 1448 until the discovery of L 1448C (Curiel et al. 1990, Bachiller et al. 1991a).

L 1448C, lying about $90''$ south of IRS 3, is a Class 0 YSO buried in the parent cloud core, hence is barely detected with wavelengths less than 100 μm (Bachiller et al. 1991b). L 1448C is one of the youngest ($\sim$3000 yr) known YSOs, and drives the L 1448 outflow, a highly collimated molecular jet seen in the CO, SiO, and H_2 emissions (Bachiller & Cernicharo 1990, Guilloteau et al. 1992, Bally et al. 1993, Bachiller et al. 1995). Near-infrared observations of Bally et al. (1993) and Davis et al. (1994) reveal a spectacular H_2 jet in the blue-shifted lobe of the L 1448C molecular outflow. Clumps of the CO and SiO emission ("bullets") are associated with bright knots of 2.122 μm H_2 emission. Chernin et al. (1994) interpreted that the 2.122 μm H_2 emission is due to cooling layers behind the bow shocks at the

surfaces of the H_2 jet. Bally et al. (1997) detected one HH object associated with L 1448C, and another HH object to the southeast of L 1448C.

We observed the L1448 dark cloud on 1995 August 30 – September 2. In Figure 9.2, we show the two energy-band X-ray images obtained with SISs, together with protostars indicated by crosses (Class I) and asterisks (Class 0). We see no significant X-ray emission from the protostars in both the soft and hard band images (see Table 9.2).

Table 9.2: Protostar candidates in L1448 region

Name	RA (1950)	Dec (1950)	0.7–2 keV (cts ks^{-1} SIS^{-1})	2–10 keV (cts ks^{-1} SIS^{-1})	Class
L1448C	3 22 34.3	+30 33 35	$\leq$0.4	$\leq$1.1	0
L1448IRS3	3 22 31.5	+30 34 49	$\leq$0.6	$\leq$0.4	I

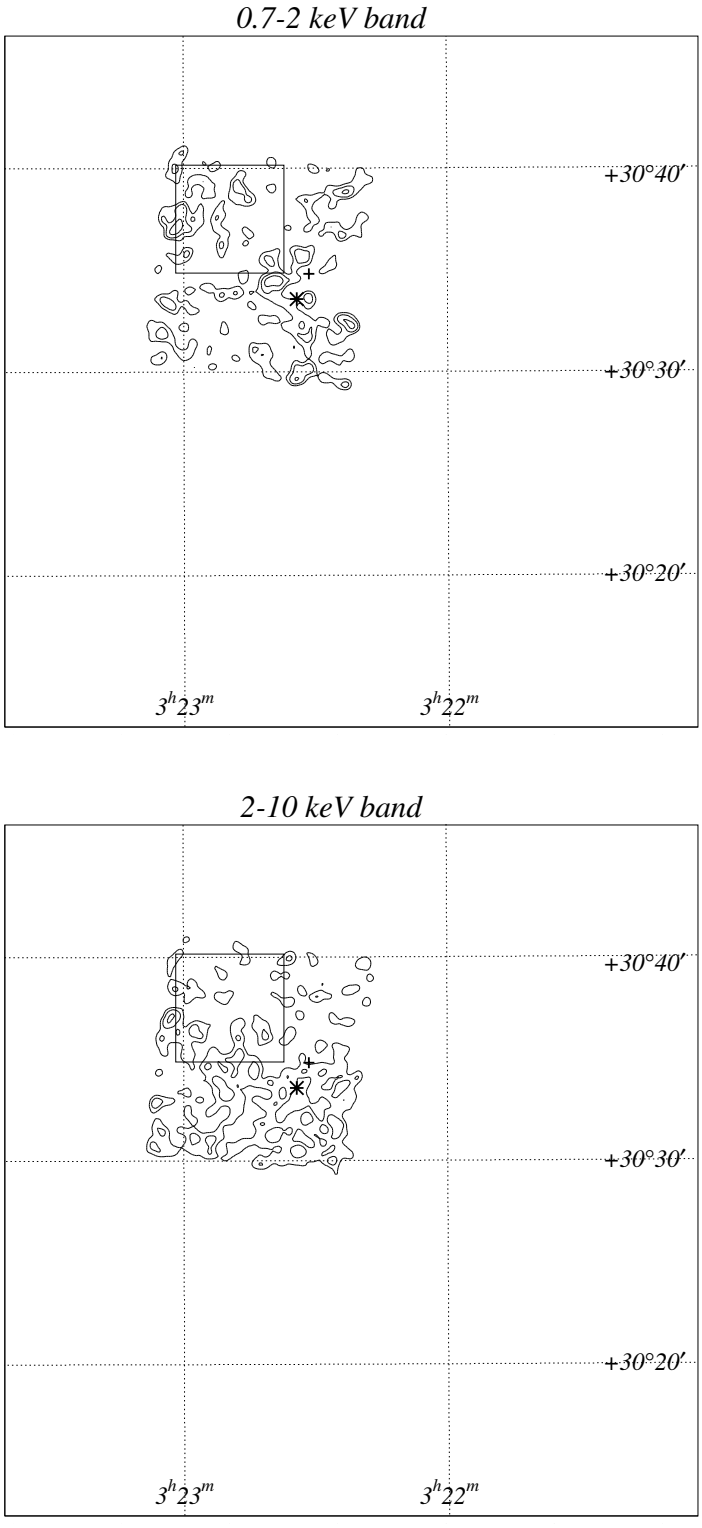

Figure 9.2: X-ray contour maps of the L1448 region, obtained with SISs. The contour levels, in units of (10^{-3}counts/SIS/ks/pixel), are: 0.01, 0.05, and 0.11 for the soft band, 0.1, 0.2, and 0.3 for the hard band.

Chapter 10

Orion ($D = 450$ pc)

The Orion cloud complex is the nearest (d =450 pc; e.g. Genzel & Stutzki 1989) giant star-forming complex (GMC) from the sun, located at (l, b) = (208, -17). It consists of the Orion A (L 1641 and 1647) and Orion B (L 1630/L 1627) clouds. The Orion A cloud extends to the south from the Orion Nebula by about 6 deg, while the Orion B cloud extends to the north from the Horsehead Nebula by about 4 deg. The total mass of the molecular gas in Orion A and B are estimated to be 1.0×10^5 $M_\odot$ and 0.8×10^5 $M_\odot$, respectively (Maddalena et al. 1986). Both of the clouds have very clumpy and filamentary structures as well as the nearby Taurus and Ophiuchi clouds. They posses an HII region, an OB association, embedded infrared sources, and a large number of YSOs.

The first systematic survey of the molecular cores in the Orion A cloud was made in the NH_3 inversion lines (Ho et al. 1979). A higher resolution survey was next made with the Bonn 100 m telescope by Batrla et al. (1983), which covered the Orion KL, Orion-S and Orion Molecular Cloud 2 regions (hearafter OMC 2); a total of eight cores were cataloged. The detailed distribution of high-density gas, which were warmed by newly formed stars around Orion KL, has been extensively investigated on $\sim1''$ to $10''$ scales using interferometric techniques (see, Chandler & Wood 1997, Wilson et al. 1996, Wright et al. 1996, Blake et al. 1996, Wiseman & Ho 1996, Umemoto et al. 1994, Tatematsu et al. 1993b, Murata et al. 1990, Migenes et al. 1989). However, for regions outside the OMC 2, Orion KL, Orion-S regions, less data are available. The high-density molecular cloud cores in the Orion A cloud have been studied with single-dish telescopes for NH_3 (Harju et al. 1991, 1993; Cesaroni & Wilson 1994) and CS (1–0) (Tatematsu et al. 1993a). Tatematsu

et al. (1993a) have found 2−7 CS (1–0) cores with an average size of ∼0.1 pc for each the ^{13}CO (1–0) clump.

On the other hand, with the 1.3 mm band, Chini et al. (1997a) obtained a high-resolution (∼11″) dust continuum map of the OMC 2/3 region in Orion A, and found 11 and 10 embedded sources from OMC 3 and OMC 2, respectively. Six sources in OMC 3 were firmly identified to be Class 0 sources. They suggested that we can trace the protostellar evolution from the north (OMC 3: younger) to the south (Class I: relatively older). Recently, Lis et al. (1998) obtained 350 μm continuum emission maps of the OMC 2/3 and OMC 1 regions, which have comparable angular resolution to the 1.3 mm map obtained by Chini et al. (1997a). In the OMC 2/3 clouds, 33 compact dust sources are detected, including all the sources except OMC 3 MMS10 detected by Chini et al. (1997a). From the ratio of 60 and 100 μm fluxes obtained with IRAS, Lis et al. (1998) estimated the upper limits for the dust temperatures to be $\sim$ 25 K and 29 K for OMC 3 and 2, respectively. In addition, using the 1300 μm flux by Chini et al. (1997a), Lis et al. (1998) derived the flux ratio of 350/1300 μm. This flux ratio indicates that the temperatures of most sources in OMC 2/3 are much lower than 70 K which implies the boundary temperature between Class 0 and I (Chen et al. 1995, 1997) The average value is $\sim$ 17 $\pm$ 4 K, for optically thin dust emission with β = 2 (grain emissivity exponent), and 11.5 $\pm$ 2 K for β = 2.5. Thus these dust continuum sources are most likely Class 0 protostars. The presence of several molecular outflows (Castets & Langer 1994) and the discovery of nearly a dozen collimated H_2 outflows from YSOs embedded in this dust filament (Yu et al. 1997) indicate the OMC 2/3 region is one of the most active sites of on-going low- and intermediate-mass star forming regions.

The Orion B (L 1630) molecular cloud complex is associated with four centers (NGC 2023, 2024, 2068, 2071). The first unbiased survey of the cores in Orion B cloud was made with the CS (J = 2–1) emission (Lada et al. 1991). Then Gibb et al. (1995) observed six out of 42 interstellar molecular cloud cores found with the high spatial resolution (60 arcsec) observation by Lada et al. (1991). Many young T Tauri stars in these areas were found to be a faint red emission line sources (Herbig 1963, Wiramihardja et al. 1989). Reipurth (1985) surveyed the Orion B cloud on the deep red Schmidt plates and found many small nebulae, most of which have subsequently turned out to be HH objects (Reipurth 1989, 1993). The

energy spectra of HH objects often show steeply rising slopes, hence would mostly be Class I sources and Class 0 for some cases.

10.1 NGC1977

We observed the region containing the reflection nebula NGC1977 on Aug 30 1993. The comprehensive report in this observation has been already represented by Yamauchi et al. (1996). Here, we focus on the X-rays from protostars. In Figure 10.1, we show the two energy-band X-ray images obtained with SISs, together with Class 0 protostars (Lis et al. 1998, Chini et al. 1997a) indicated by asterisks. The count rate of each protostar is listed in Table 10.2.

Although sources which exceed 5 σ level are small number (only CSO2 and possibly CSO 11/12), we see the hard X-ray distribution along with the "islands" of the dust continuum peaks in OMC3, while no excess in the soft X-ray band (0.7–2 keV) is found from this region. Thus the hard X-rays would be coming from deep inside the molecular core, because the column density of the OMC3 core of larger than 4×10^{22} cm^{-2} (Chini et al. 1997a) absorbs most of the soft X-rays. In OMC 2, rather strong X-rays (e.g. source 24 in Yamauchi et al. 1996) with relatively small absorption (hence, these would be point sources lying in front of the molecular core) make it difficult to see X-rays from inside the core. Still some hints are found, showing hard X-ray arc along the dust "islands". We thus have good hint for the hard X-ray emission from inside the cores (350 μm and 1.3 mm peaks) in OMC2 and OMC3, where Class 0 protostars are lying.

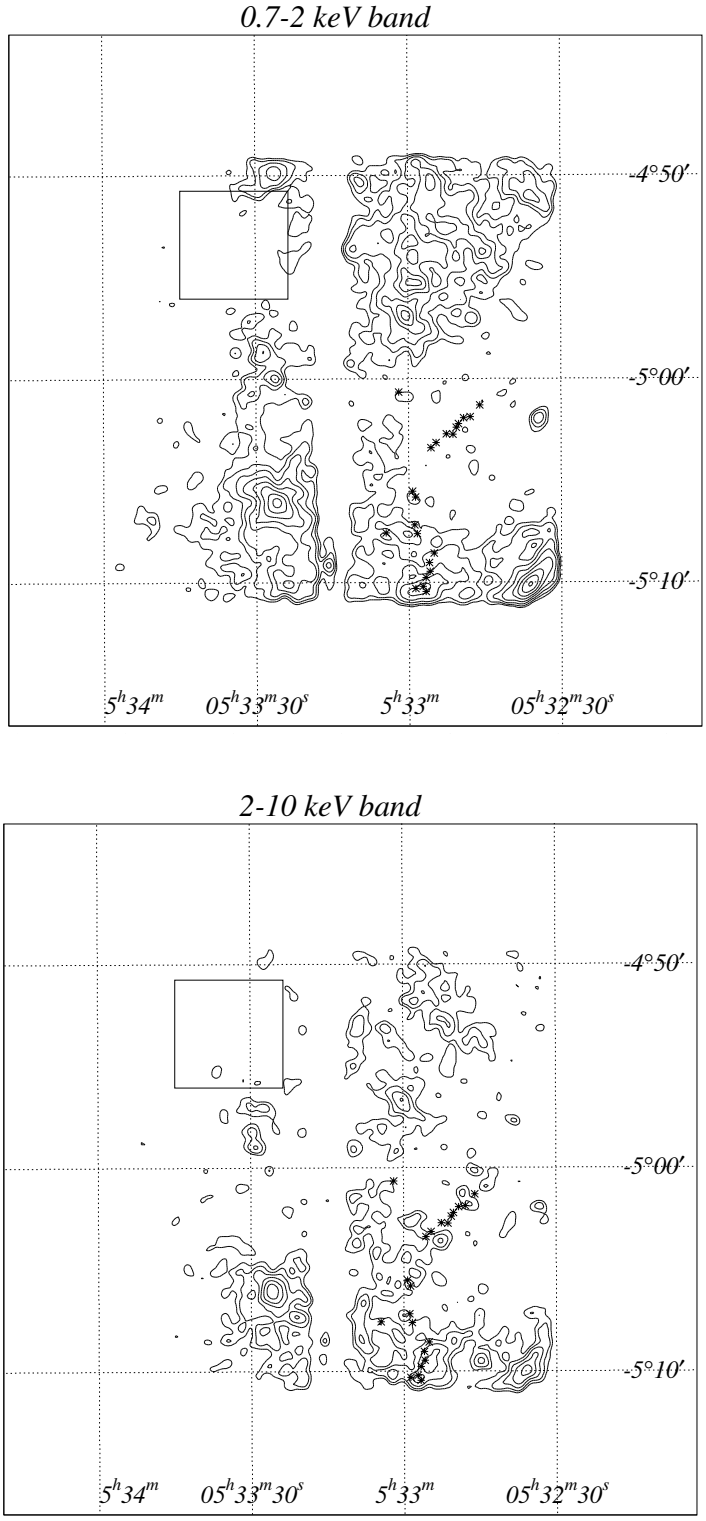

Figure 10.1: X-ray contour maps of the NGC1977 region, obtained with SISs. The contour levels, in units of (10^{-3}counts/SIS/ks/pixel), are : 0.2, 0.4, 0.8, 1.3, 2, 3, 5, and 7 for the soft band, and are: 0.2, 0.4, 0.6, 1.0, 1.4, and 2.1 for the hard band.

Table 10.1: Protostar candidates in NGC1977 region

Name	RA (1950)	Dec (1950)	0.7–2 keV (cts ks^{-1} SIS^{-1})	2–10 keV (cts ks^{-1} SIS^{-1})	Class
CSO1	5 33 01.9	−5 00 39	≤3.5	≤3.8	0
CSO2	5 32 46.0	−5 01 18	≤3.2	4.3±1.4	0
CSO3	5 32 47.9	−5 01 52	≤1.9	≤4.2	0
CSO4	5 32 49.2	−5 01 56	≤1.5	≤2.8	0
CSO5=MMS1	5 32 50.2	−5 02 13	≤1.8	≤1.9	0
CSO6=MMS2	5 32 50.6	−5 02 23	≤1.5	≤2.8	0
CSO7=MMS3?	5 32 51.3	−5 02 44	≤1.2	≤3.5	0
CSO8=MMS4	5 32 52.6	−5 02 43	≤1.3	≤2.8	0
CSO9=MMS5	5 32 54.6	−5 03 08	≤1.1	≤4.7	0
CSO10=MMS6	5 32 55.6	−5 03 24	≤3.1	≤4.8	0
CSO11	5 32 59.3	−5 05 31	≤5.7	6.2±1.7†	0
CSO12=MMS7	5 32 58.7	−5 05 49	≤4.7	5.1±1.7†	0
CSO13=MMS8	5 32 58.9	−5 07 11	—^{a}	≤5.9	0
CSO14=MMS9	5 32 58.4	−5 07 37	—^{a}	≤7.1	0
CSO15	5 32 55.1	−5 08 34	—^{b}	—^{c}	0
CSO16=FIR1c	5 32 56.0	−5 09 02	—^{b}	—^{c}	0
CSO17=FIR1b	5 32 55.9	−5 09 28	—^{b}	—^{c}	0
CSO18=FIR1a	5 32 56.7	−5 09 46	—^{b}	—^{c}	0
CSO19	5 32 57.3	−5 10 12	—^{b}	—^{c}	0
CSO20=FIR2	5 32 56.7	−5 10 27	—^{b}	—^{c}	0
CSO21	5 32 58.7	−5 10 18	—^{b}	—^{c}	0
MMS10	5 33 04.5	−5 07 34	—^{a}	≤7.1	0

†: contaminated with each other.

a: contaminated by unidentified source located at 5h33m00.4s −5d07m37.2s (B1950) and source 24 in Yamauchi et al. 1996.

b: contaminated by source 24 in Yamauchi et al. 1996.

c: contaminated by source 21 in Yamauchi et al. 1996.

10.2 Orion Nebula (M42) (PV)

We observed the Orion Nebula region on 1993 Aug 30–31. In Figure 10.2, we show the two energy-band images obtained with SISs. Protostar candidates indicated by crosses, especially the Class 0 protostars detected by Chini et al. (1997a) and Lis et al. (1998) are indicated by asterisks.

In this region, the protostar detection is difficult because of the large contamination from the Orion Trapezium region (Yamauchi et al. 1996). For example, Ori KL and OMC-1 FIR4 are completely embedded in the emission from the Orion Trapezium. In addition, due to the strong X-rays (i.e. source 20, 24, and 28 in Yamauchi et al. 1996) probably lying in front of the molecular core, make it difficult to see X-rays from inside the core. Therefore, we see no significant X-ray emission from the protostars in both the soft and hard band image (see Table 10.2).

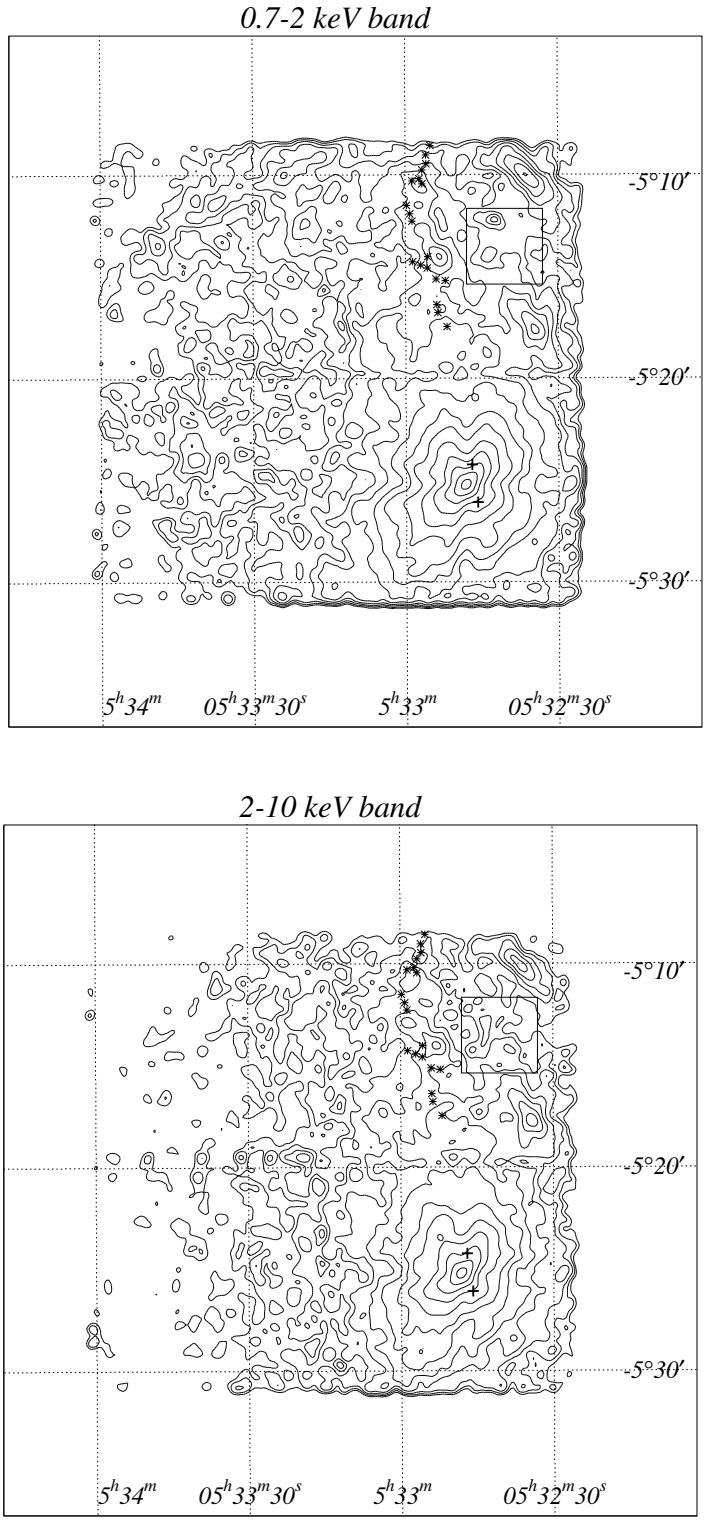

Figure 10.2: X-ray images of the Orion Nebula region (PV), obtained with SISs. The contour levels for both of the band maps, in units of (10^{-3}counts/SIS/ks/pixel), are : -0.9, -0.7, -0.5, 0.1, 0.8, 2, 4, 7, 12, 20, 30, 50, 80, and 130, for the soft band, and -0.2, 0.0, 0.3, 0.8, 2, 3,5, 8, 12, 20, 30, 50, 80, and 130, for the hard band.

Table 10.2: Protostar candidates in Orion Nebula region (PV)

Name Name	RA (1950)	Dec (1950)	0.7–2 keV (cts ks^{-1} SIS^{-1})	2–10 keV (cts ks^{-1} SIS^{-1})	Class
CSO16=FIR1c	5 32 56.0	−5 09 02	≤2.3	≤2.3	0
CSO17=FIR1b	5 32 55.9	−5 09 28	≤6.1	≤1.5	0
CSO18=FIR1a	5 32 56.7	−5 09 46	—[a]	≤4.6	0
CSO19	5 32 57.3	−5 10 12	—[a]	—[a]	0
CSO20=FIR2	5 32 56.7	−5 10 27	—[a]	—[a]	0
CSO21	5 32 58.7	−5 10 18	—[a]	—[a]	0
CSO22=FIR3	5 32 59.8	−5 11 30	—[a]	—[a]	0
CSO23=FIR4	5 32 59.1	−5 11 55	—[b]	—[b]	0
CSO24=FIR5	5 32 58.7	−5 12 17	—[b]	—[b]	0
CSO25=FIR6b	5 32 55.6	−5 14 02	—[b]	—[b]	0
CSO26	5 32 58.6	−5 14 16	≤7.7	—[b]	0
CSO27	5 32 57.0	−5 14 26	—[c]	—[c]	0
CSO28=FIR6a	5 32 55.7	−5 14 35	—[c]	—[c]	0
CSO29=FIR6c	5 32 54.0	−5 15 07	—[c]	—[c]	0
CSO30=FIR6d	5 32 52.2	−5 15 12	—[c]	—[c]	0
CSO31	5 32 53.9	−5 16 23	—[d]	—[d]	0
CSO32	5 32 53.7	−5 16 47	—[d]	—[d]	0
CSO33	5 32 51.9	−5 17 28	—[d]	—[d]	0
OriKL	5 32 47	−5 24 14	—[d]	—[d]	I
OMC-1FIR4	5 32 45.9	−5 26 06	—[d]	—[d]	I

a: contaminated by source 24 in Yamauchi et al. 1996.

b: contaminated by source 24 and 28 in Yamauchi et al. 1996.

c: contaminated by source 20 in Yamauchi et al. 1996.

d: contaminated by Trapezium region.

10.3 Orion Nebula (M42) (AO 5)

In AO 5, we observed the Orion Nebula region with ASCA dividing the period into two. The first observation was done for ≈50 ksec exposure on September 23–24 1997, and the second observation was done for ≈10 ksec exposure on September 30–October 1 1997. At the first observation, no data were available for SIS 1, because of a trouble of the data acquisition. In Figure 10.3 and 10.4, we show the two energy-band X-ray images obtained with SISs. Due to the large X-ray flux of the Trapezium, we can see no significant X-ray emissions from the protostars in both the soft and hard band images.

Table 10.3: Protostar candidates in Orion Nebula (AO5, the 1st day)

Name	RA (1950)	Dec (1950)	0.7–2 keV (cts ks^{-1} SIS^{-1})	2–10 keV (cts ks^{-1} SIS^{-1})	Class
OriKL	5 32 47	−5 24 14	—[a]	—[a]	I
OMC-1FIR4	5 32 45.9	−5 26 06	—[a]	—[a]	I

a: contaminated by Trapezium region.

Table 10.4: Protostar candidates in Orion Nebula (AO5, the 2nd day)

Name	RA (1950)	Dec (1950)	0.7–2 keV (cts ks^{-1} SIS^{-1})	2–10 keV (cts ks^{-1} SIS^{-1})	Class
OriKL	05 32 47	−05 24 14	—[a]	—[a]	I
OMC-1FIR4	05 32 45.9	−05 26 06	—[a]	—[a]	I

a: contaminated by Trapezium region.

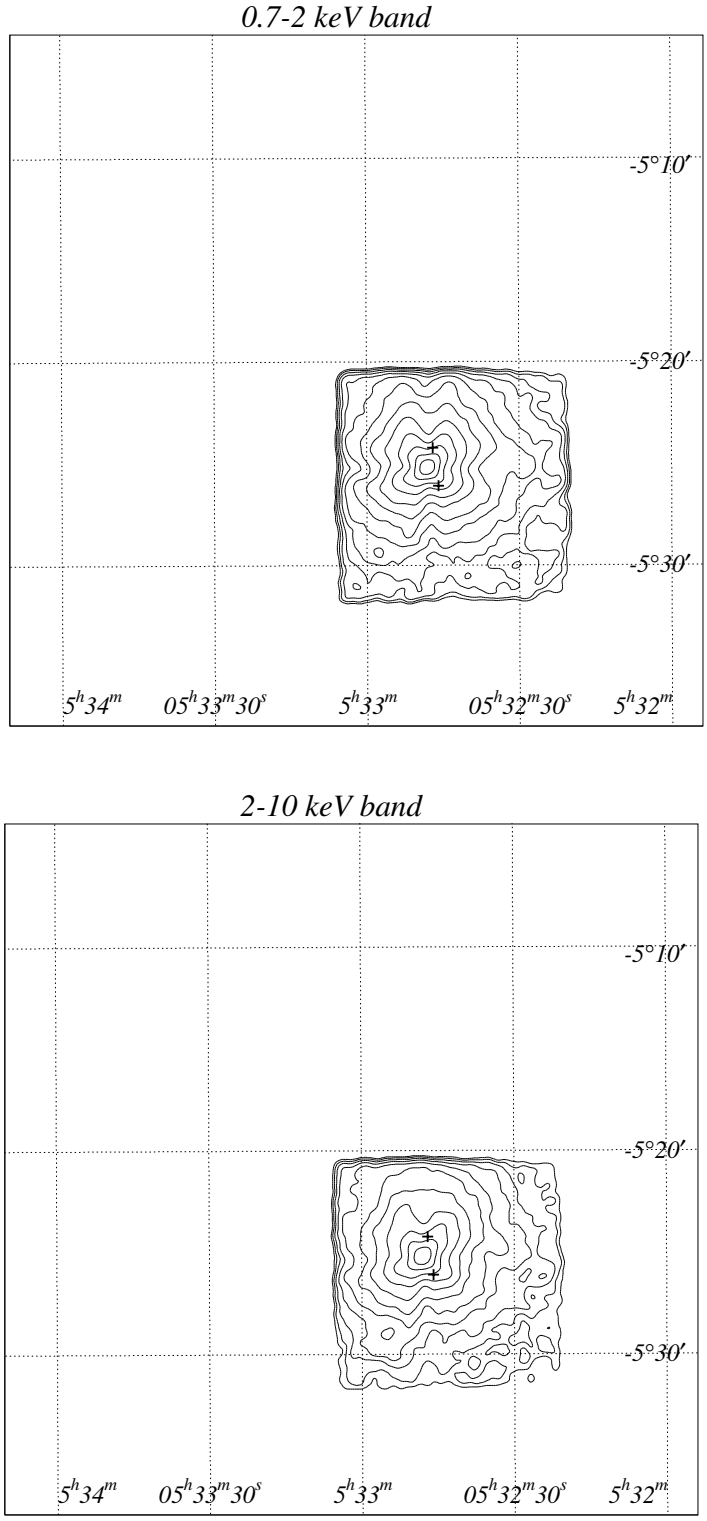

Figure 10.3: X-ray images of the Orion Nebula region (1st day), obtained with SISs. The contour levels for both of the band maps, in units of (10^{-3}counts/SIS/ks/pixel), are: 0.6, 1.0, 1.6, 2.5, 4.0, 6.3, 10, 16, 25, 40, 63, and 100.

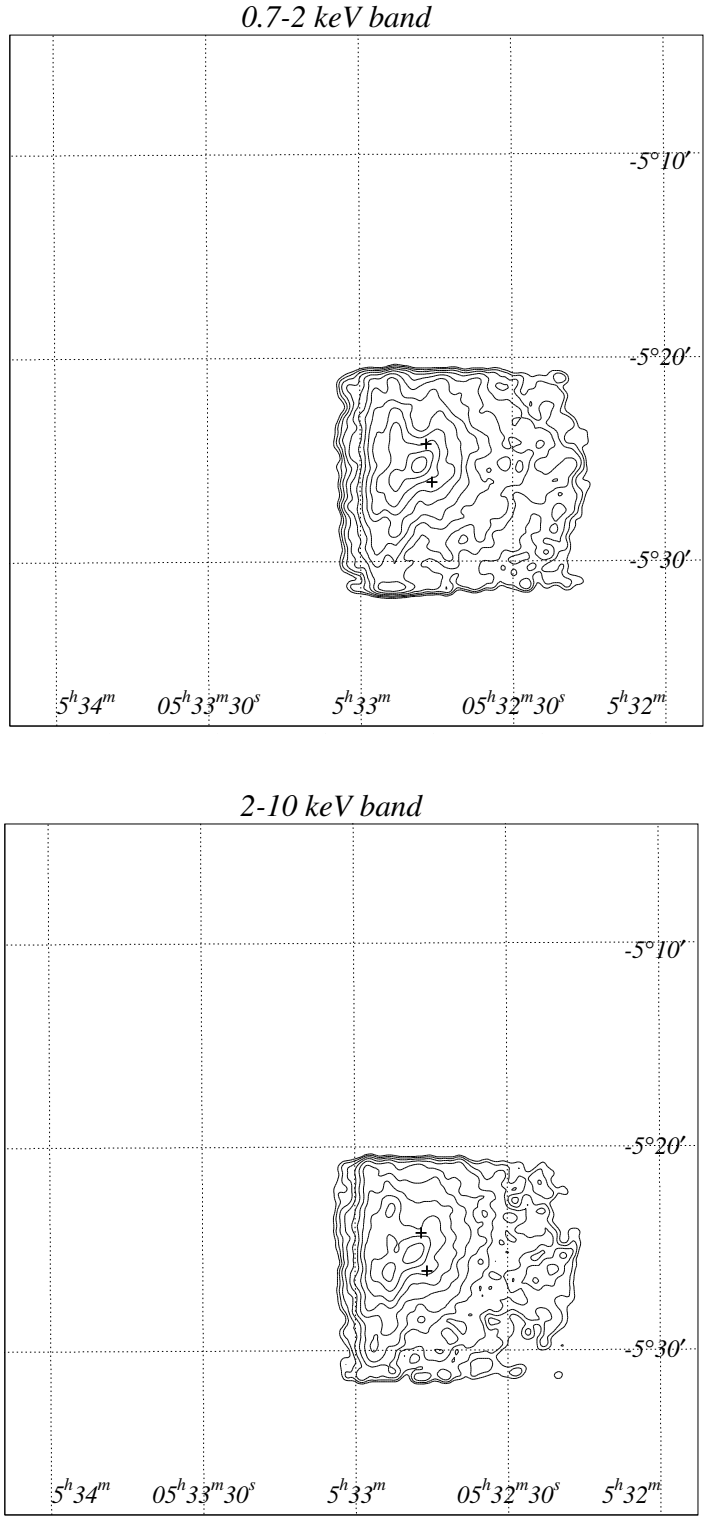

Figure 10.4: X-ray images of the Orion Nebula region (2nd day), obtained with SISs. The contour levels for both of the band maps, in units of (10^{-3}counts/SIS/ks/pixel), are: 0.6, 1.0, 1.6, 2.5, 4.0, 6.3, 10, 16, 25, 40.0, 63, and 100.

10.4 L1641 North

We observed the L1641 North region on March 13–15 1994. In Figure 10.5, we show the two energy-band X-ray mages obtained with SISs together with Protostar candidates indicated by crosses.

We see no significant X-ray emission from the protostars in both the soft and hard band images.

Table 10.5: Protostar candidates in L1641 North region

Name	RA (1950)	Dec (1950)	0.7–2 keV (cts ks^{-1} SIS^{-1})	2–10 keV (cts ks^{-1} SIS^{-1})	Class	ref
HH34IRS	5 33 03.7	−6 28 53	—[a]	—[a]		1
HH222VLA	5 33 15.62	−6 24 54.72	—[b]	≤1.7		2
L1641North	5 33 52.7	−6 24 02	3.3±0.8[c]	3.1±0.7[c]		3

a: This source is on the gap between CCD chips.

b: contaminated by V571 Ori (CTTS) and/or NGC1977 222 (CTTS).

c: highly confused with Parenago 2375.

References for the coordinates – (1) Reipurth et al. 1986 A&A 164 51;

(2) Yusef-Zadeh, F. et al. 1990, ApJ 348, L64;

(3) Fukui et al. 1993

Figure 10.5: X-ray images of the L1641 North region, obtained with SISs. The contour levels, in units of (10^{-3}counts/SIS/ks/pixel), are : 0.2, 0.4, 0.8, 1.3, 2.2, and 3.6 for the soft band, 0.1, 0.3, 0.5, 0.8, and 1.4 for the hard band.

10.5 HH212

We observed the L1630 HH212 region on February 28–March 1 1998. In Figure 10.6, we show the two energy-band X-ray images obtained with SISs, together with a Class 0 protostar indicated by asterisk. We see no significant X-ray emission from the protostar in both soft and hard band images.

Table 10.6: Protostar candidates in HH212 region

Name	RA (1950)	Dec (1950)	0.7–2 keV (cts ks^{-1} SIS^{-1})	2–10 keV (cts ks^{-1} SIS^{-1})	Class
HH212-mm	5 41 19.0	−1 04 08	$\leq$0.25	$\leq$1.0	0

References for the coordinates – Carkner et al. 1998

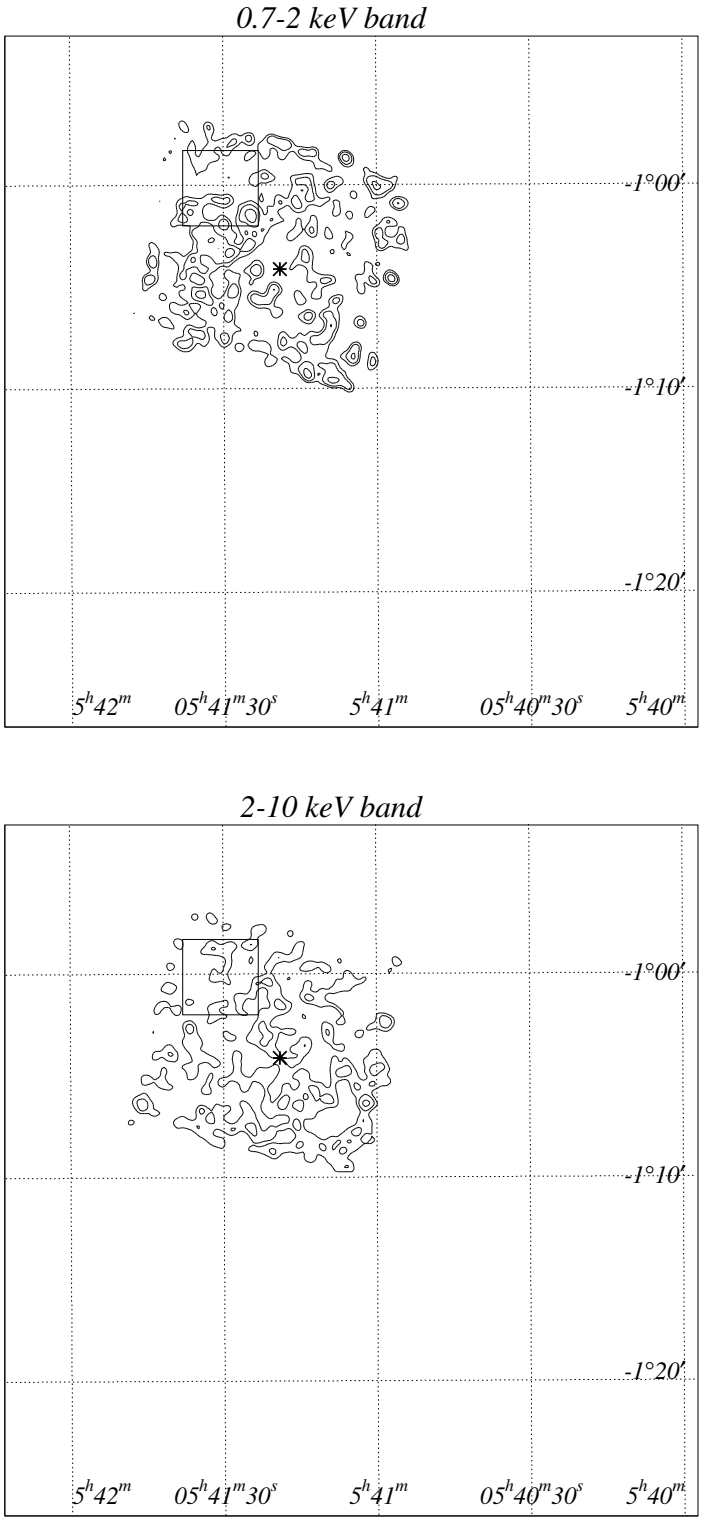

Figure 10.6: X-ray contour maps of the HH212 region, obtained with SISs. The contour levels, in units of (10^{-3}counts/SIS/ks/pixel), are : 0.002, 0.05, and 0.1 for the soft band, 0.03, 0.1, and 0.3 for the hard band.

10.6 HH91

We observed the L1630 HH91 region on March 1–2 1998. In Figure 10.7, we show the two energy-band X-ray images obtained with SISs, together with Class 0 protostars indicated by asterisks. We see no significant X-ray emission from the protostars in both the soft and hard band images.

Table 10.7: Protostar candidates in HH91 region

Name	RA (1950)	Dec (1950)	0.7–2 keV (cts ks^{-1} SIS^{-1})	2–10 keV (cts ks^{-1} SIS^{-1})	Class
HH91IRS	5 39 25.9	−1 15 01	$\leq$0.42	$\leq$1.6	I?

References for the coordinates – Moneti, A. & Reipurth, B. 1995

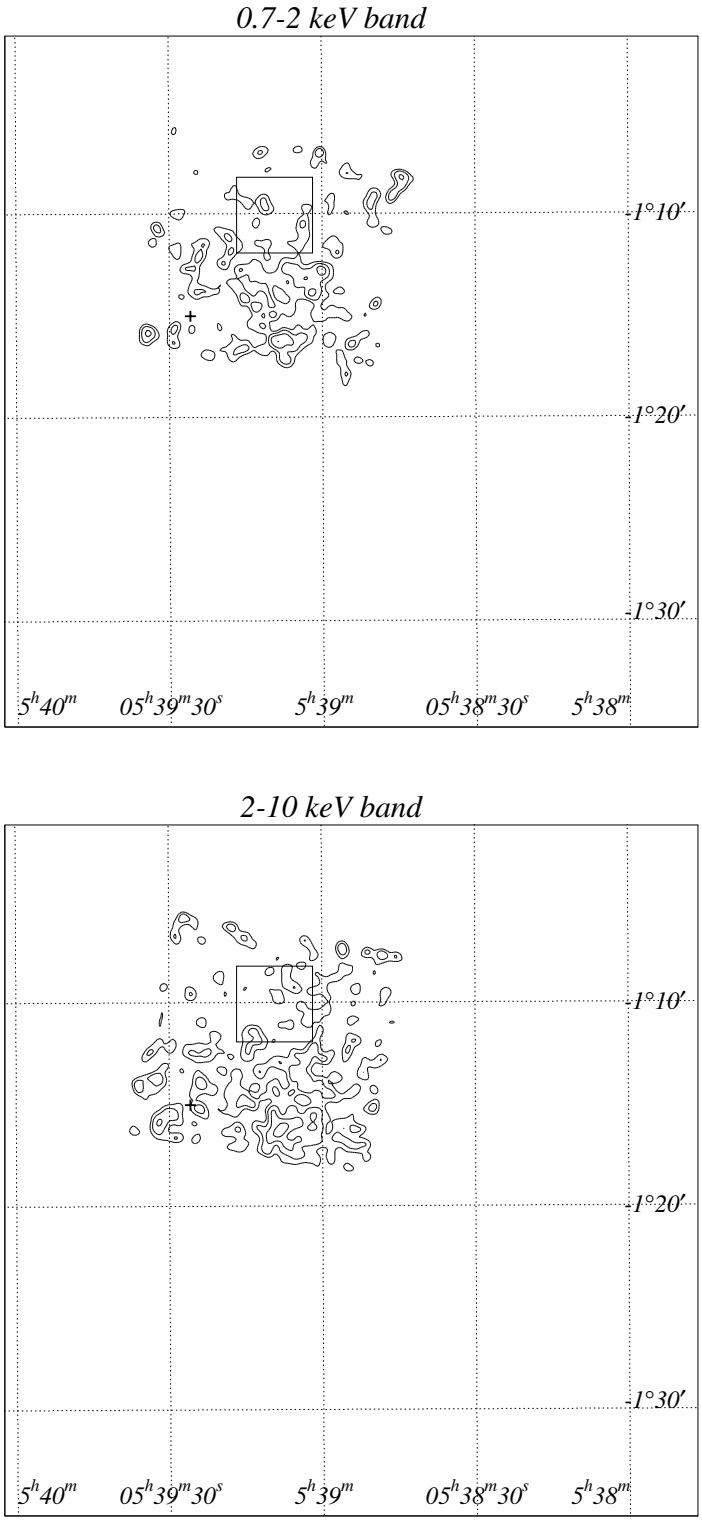

Figure 10.7: X-ray images of the HH91 region, obtained with SISs. Protostar candidate (HH91IRS) is indicated by cross. The contour levels, in units of (10^{-3}counts/SIS/ks/pixel), are : 0.04, 0.1, 0.2, and 0.4 for the soft band, 0.04, 0.1, and 0.2 for the hard band.

10.7 L1582B

L 1582 B is one of the dark filaments coincident with a northern fragment of the λ Orionis molecular ring, at an estimated distance of 400 pc (Maddalena & Morris 1987). The cloud contains RNO 43 (Cohen 1980) at the edge, which is the brightest of a group of HH objects knots (RNO 43 *a* to *d*, Jones et al. 1984).

The high-velocity CO emission present around the HH objects shows a double pattern of overlapping blue-shifted and red-shifted gas previously attributed to a pair of outflows seen nearly a pole-on geometry (RNO 43 N and RNO 43 S, see Edwards & Snell 1984). Jones et al. (1984) found that the proper motion vectors of the HH objects associated with the two outflow components all pointed away from a single far-infrared source of luminosity 12.4 $L_{\odot}$ (Cohen & Schwarts 1987, assuming a distance of 400 pc) located farther south, on the axis defined by the two high-velocity emission regions.

We observed the L1582B region on February 22–24 1998. We show the two energy-band X-ray images obtained with SISs, together with protostars in Figure 10.8. We see no significant X-ray emission from the protostars in both soft and hard band images.

Table 10.8: Protostar candidates in L1582B region

Name	RA (1950)	Dec (1950)	0.7–2 keV (cts ks^{-1} SIS^{-1})	2–10 keV (cts ks^{-1} SIS^{-1})	Class
RNO43IRS	05 29 30.74	+12 47 34.3	$\leq$0.18	$\leq$0.36	0

References for the coordinates – Chini et al. 1997b

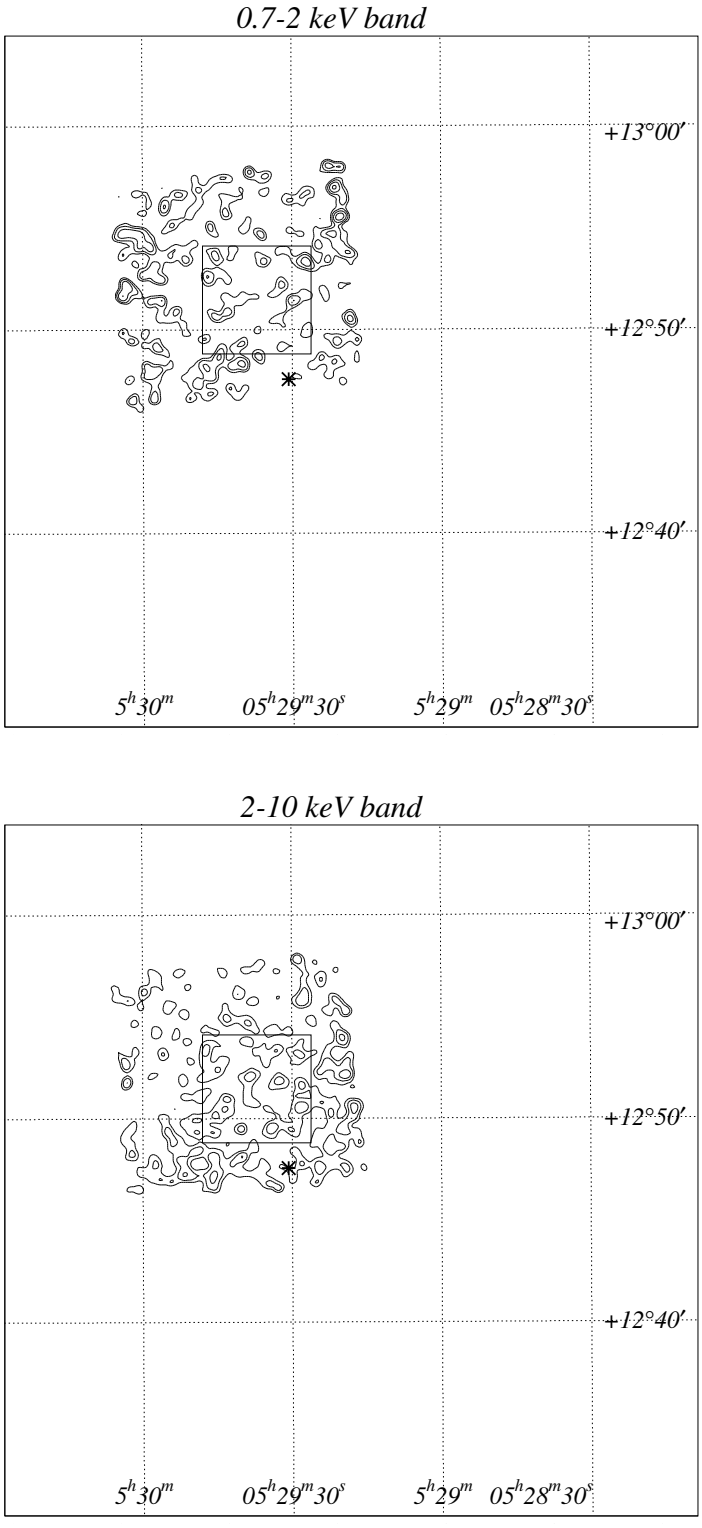

Figure 10.8: X-ray images of the L1582B region, obtained with SISs. The contour levels, in units of (10^{-3}counts/SIS/ks/pixel), are: 0.02, 0.05, 0.09, and 0.15 for the soft band, 0.01, 0.07, and 0.2 for the hard band.

Chapter 11

Discussions

11.1 X-ray Loud vs. X-ray Quiescent

We proved 99 protostar candidates through a survey in 17 fields (24 observations) of dark clouds.

In the soft band (0.7–2 keV), there were 53 protostar candidates which were almost contamination-free. From the sources, we detected 3 sources (5% of the total) with $S/N > 5$ level, although two of them are not point-like but diffuse.

In the hard band (2–10 keV), there were 59 protostar candidates which were almost contamination-free from the other TTSs. From the sources, we detected 22 sources (40% of the total) with $S/N > 5$ level, although some of them are contaminated with the other protostar candidates or are not point-like but diffuse emissions, then the minimum number of the detection is 18 sources (30% of the total).

The detected and non-detected sources are listed in Table 11.1. In this section, we discuss the reason for the detection and non-detection.

Table 11.1: X-ray detection of protostar candidates

Name	Field	Detection[a]		Variability[b]	SED	L_{bol}	Outflow[c]	$\dot{M}_{outflow}$[d]
		Soft	Hard	Hard		$[L_\odot]$		$[10^{-5} M_\odot \text{ yr}^{-1}]$
WL12	Oph	N	N		I	6.4	extend	
IRS27=WL22	Oph	N	D	long	II?	15.7		
WL16	Oph	N	D	long	II?	18.3		
IRS29=WL1	Oph	N	N		I	1.1		
EL29	Oph	N	D	flare	I	36.3	overlap	
IRS34	Oph	N	D	—	II	0.8		
IRS43=YLW15	Oph	N	D	flare	I	7.2	overlap	
IRS44	Oph	N	D	—	I	8.9	overlap	2
IRS46	Oph	N	D	—	I	0.8		
IRS48	Oph	N	N		I	10.7	extend	
IRS51	Oph	N	D	long	I	2.2	overlap	
IRS54	Oph	N	N		I	9.9		
WL6	Oph	N	D	sin?, long	I	1.02	overlap	
LFAM1	Oph	—	—		I	0.04		
WL19	Oph	N	D	long	II–IID	0.12		
RhoOphB	Oph	N	N		I		(bipolar)	
GY245=CRBR72	Oph	N	N		I			
GY284	Oph	N	N		I			
CRBR42=GY91	Oph	N	N		I			
CRBR85	Oph	—	D	—	I			
LFAM26	Oph	N	D	long	I			
YLW256=GY256	Oph	N	—		I			
VLA1623	Oph	—	—		0	1	extend	0.5
IRAS16293-2422	Oph	—	N		0	18.1	extend	4
IRS2=TS13.1	CrA	—	D	long	I	11.0		
IRS5=TS2.4	CrA	—	D	long	I	0.9		
IRS1=TS2.6	CrA	—	D	long	I			
IRS9=R2	CrA	—	D	long	I	0.6		
IRS7=R1	CrA	—	D	flare, long	I	3.6	overlap	
IRS32	CrA	N	N		I	1.3		

Table 11.1–*Continues*

Name	Field	Detection[a]		Variability[b]	SED	L_{bol}	Outflow[c]	$\dot{M}^{d}_{outflow}$
		Soft	Hard	Hard		$[L_{\odot}]$		$[10^{-5} M_{\odot}\ \mathrm{yr}^{-1}]$
IRAS04108+2803B	Tau	N	N		I	0.6		
CW Tau	Tau	—	—		II			
IRAS04113+2758	Tau	—	N		II	2.0		
IRAS04361+2547	Tau	N	N		I	2.5	extend	0.9
IRAS04365+2535	Tau	N	N		I	1.9	extend	
IRAS04368+2557	Tau	N	N		0	1.3		
IRAS04369+2539	Tau	—	—		II	4.6		0.3
IRAS04154+2823	Tau	—	—		I	0.3		
CoKu Tau-1	Tau	—	—		I			
L1551IRS5	Tau	N	N		I	21.0	extend	2
HLTau	Tau	—	—		II	6.0	extend	
L1551NE	Tau	N	N		I	3.9		
HH30IRS	Tau	—	—					
Th28	lup	—	—					
SMM9=S68N	Serp	N	N		0			
SMM1=FIRS1	Serp	N	N		0	50		
SMM3	Serp	—	—		0	<11		
SMM4	Serp	—	—		0	<11		
SMM2	Serp	—	—		0			
FUOri	Serp	N	—		0			
EC95	Serp	D	D	short	I?			
IRAS2(NGC1333)	Perseus	—	—		0	40		
IRAS4A(NGC1333)	Perseus	—	N		0	14		>0.2(?)
IRAS4B(NGC1333)	Perseus	—	N		0	14		>0.2(?)
SVS12	Perseus	D	D	—		13.0		
L1448C	Perseus	N	N		0	10	extend	0.1–2
L1448IRS3	Perseus	N	N		I	9	extend	2

Table 11.1–*Continues*

Name	Field	Detection[a]		Variability[b]	SED	L_{bol}	Outflow[c]	$\dot{M}^{d}_{outflow}$
		Soft	Hard	Hard		$[L_{\odot}]$		$[10^{-5} M_{\odot}\ \mathrm{yr}^{-1}]$
CSO1	Ori	N	N		0			
CSO2	Ori	N	D	—	0			
CSO3	Ori	N	N		0			
CSO4	Ori	N	N		0			
CSO5=MMS1	Ori	N	N		0	<55		
CSO6=MMS2	Ori	N	N		0			
CSO7=MMS3?	Ori	N	N		0			
CSO8=MMS4	Ori	N	N		0	<56		
CSO9=MMS5	Ori	N	N		0			
CSO10=MMS6	Ori	N	N		0	<60		
CSO11	Ori	N	D	—	0			
CSO12=MMS7	Ori	N	D	—	0	76		
CSO13=MMS8	Ori	—	N		0	<89		
CSO14=MMS9	Ori	—	N		0	<94		
CSO15	Ori	—	—		0			
CSO16=FIR1c	Ori	N	N		0	128		
CSO17=FIR1b	Ori	N	N		0			
CSO18=FIR1a	Ori	—	N		0	<138		
CSO19	Ori	—	—		0			
CSO20=FIR2	Ori	—	—		0	<157		
CSO21	Ori	—	—		0			
MMS10	Ori	—	N		0			
CSO22=FIR3	Ori	—	—		0			10
CSO23=FIR4	Ori	—	—		0			100
CSO24=FIR5	Ori	—	—		0			
CSO25=FIR6b	Ori	—	—		0			
CSO26	Ori	N	—		0			
CSO27	Ori	—	—		0			

Table 11.1–*Continues*

Name	Field	Detection[a]		Variability[b]	SED	L_{bol}	Outflow[c]	$\dot{M}^{d}_{outflow}$
		Soft	Hard	Hard		$[L_{\odot}]$		$[10^{-5} M_{\odot}\ \mathrm{yr}^{-1}]$
CSO28=FIR6a	Ori	—	—		0			
CSO29=FIR6c	Ori	—	—		0			
CSO30=FIR6d	Ori	—	—		0			
CSO31	Ori	—	—		0			
CSO32	Ori	—	—		0			
CSO33	Ori	—	—		0			
OriKL	Ori	—	—		I			3000
OMC-1FIR4	Ori	—	—		I			
HH34IRS	Ori	—	—					
HH222VLA	Ori	—	N					
L1641North	Ori	D	D	—				20
HH212-mm	Ori	N	N		0			
HH91IRS	Ori	N	N		I?			
RNO43IRS	Ori	N	N		0			20

a: Detection in soft band (0.7–2 keV) and hard band (2–10 keV). D and N means detection and non-detection, respectively. "—" means undistinguishable due to a contamination from the other bright source.

b: X-ray variability at the hard band; short – variability within one day, long – variability in days to years, flare – X-ray flare, sin – sinusoidal modulation

c: Feature of red- and blue-shifted lobes in molecular outflow (see subsection 11.1.4)

d: Massloss rate derived from Wu, Huang, and He 1996; $\dot{M}_{outflow} = M_g \times \delta V / R_{max}$.

11.1.1 Age Effect: When a Star Begins to Emit X-rays ?

In observations of Orion cloud, we obtained a hint for X-rays from Class 0 objects lying OMC2/3 region (see Table 11.1, Table 11.2). The OMC 2/3 region was included in the field of view of GIS among the four observations executed on Aug 30–31 1993, Sep 23–24 1997, Sep 30–Oct 1 1997. Then we accumulated all the GIS data, in order to search the detection in this region by GIS which has more sensitive in hard band than SIS.

We show the X-ray contour maps of the OMC 2–3 region, obtained with GISs (combined images of GIS 2 and 3) in Figure 11.1. Class 0 sources (Chini et al. 1997a, Lis et al. 1998) are indicated by asterisks.

In this deep exposure map ($\approx$ 95 ksec $\times$ 2 GIS), the hard X-ray distribution is rather well correlated to "islands" of the 350 μm and 1.3 mm peaks, i.e. embedded protostars, within limited spatial resolution of GIS. The distribution is also correlated with the filament of the molecular cloud (Chini et al. 1997a). In particular, hard X-ray enhancement around CSO1, CSO3–10 (MMS1–6), CSO12 (MMS7), CSO14 (MMS9) in OMC 3 and CSO 21 in OMC 2 is highly suggestive. As for the sources, the MMS 6 is surrounded by a region of high-velocity emission in the velocity range v_{LSR} =14–18 km s^{-1} (Chini et al. 1997a). and from MMS 7, a large HH flow of $\sim$10$'$ was discovered to (Yu et al. 1997).

On the other hand, no excess is found from this region in the soft X-ray band (0.7–2 keV) (see above panel). This indicates the hard X-rays are coming deep inside the molecular core. Then this result would be the first evidence for the hard X-ray emissions from inside the cores (350 μm peak, 1.3 mm peak) of OMC2 and OMC3, where Class 0 protostars are lying, and we suppose that X-rays from Class 0 protostars have been already emitted.

As for Class I and II phases, we detected 14 sources of 29 Class I samples, while we detected 4 sources of 5 Class II samples. Then we found that all the evolutional phases emit X-ray certainly. We listed the detection rates of each evolutional phase in Table 11.2, seperating by the source distance. These rates were obtained with SIS detectors. In the Table 11.2, it is shown that there are few Class 0 sources in near molecular clouds and few Class I sources in distant molecular clouds. Then we obtain no apparent effect by age statistically without bias by distances.

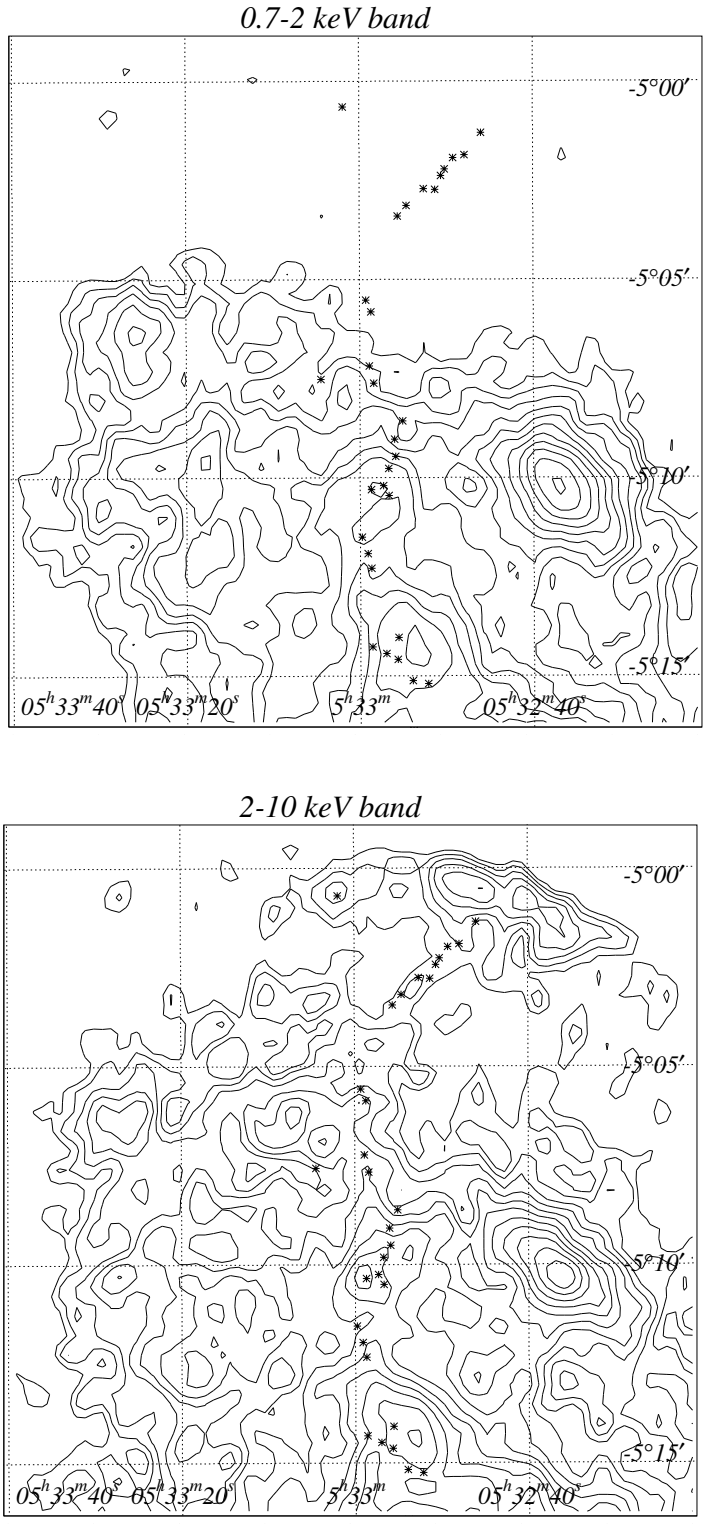

Figure 11.1: X-ray contour maps of the OMC 2–3 region, obtained with GISs (combined images of GIS 2 and 3). Class 0 sources (350 μm sources: Lis et al. 1998) are indicated by asterisks. The contour levels, in units of (counts/GIS/ks/pixel), are: 3.6, 4.3, 5.2, 6.3, 7.5, 9.1, 10.9, 13.1, 15.8, 19.0, 22.8, 27.4 for the soft band, and 3.0, 3.5, 4.2, 5.0, 5.9, 7.1, 8.4, 10.0, 11.9, 14.1, 16.8 for the hard band. Vignetting is not corrected. Background is not subtracted.

Table 11.2: Detection rates of protostar candidates at each phase (2–10 keV band)

SED	Distance		
	∼150 pc	∼300 pc	∼ 500 pc
0	0/2	0/5	3/20
I	13/26	1/2	0/1
II	4/5	0/0	0/0

11.1.2 Stellar Mass Effect

In the first order, the bolometric luminosity derived at IR band represents the stellar mass. Then, to investigate the dependence of detection on stellar mass, we made a diagram of X-ray flux versus bolometric luminosity as seen in Figure 11.2. We chose the samples from ρ Oph, R CrA, and Taurus cloud, which lie at the almost same distance of about 150 pc, and excluded the sources in flare phase. From this diagram, we find that the detected protostar candidates have bolometric luminosities range from 0.1 to 50 solar luminosity. The bolometric luminosities of non-detected protostars also indicate similar distribution, and we see no apparent difference between detected protostars and non-detected ones in the stellar mass.

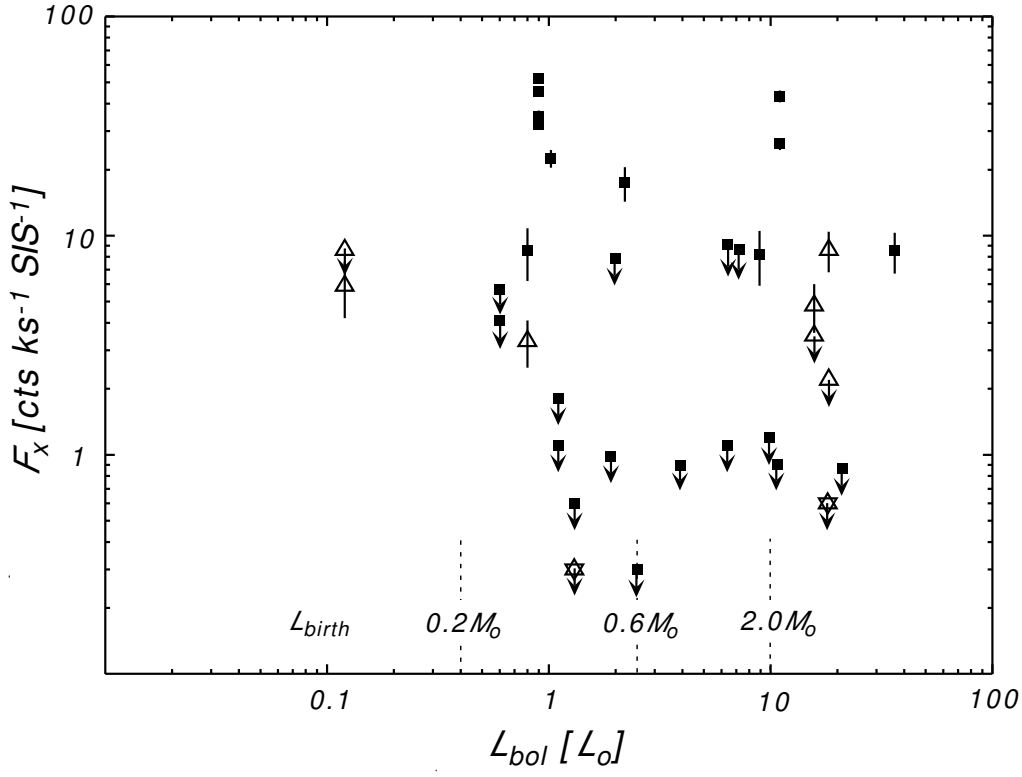

Figure 11.2: Bolometric luminosity versus X-ray flux of protostar candidates in ρ Oph, R CrA, and Taurus cloud. Class 0s, Class Is, and Class IIs are shown by open stars, filled squares, and open triangles, respectively. The range of birth line luminosities L_{birth} corresponding to three typical stellar masses (0.2, 0.6, and 2.0 $M_\odot$; from Bontemps et al. 1996) are indicated by vertical dotted lines. The protostar candidates in flare phase are excluded from these samples.

11.1.3 Long Term Variability Effect

Several selected fields, which include ρ Oph, RcrA and Orion, have been repeatedly observed. In the first observation of the ρ Oph region, two Class I sources WL6 and EL29 were found to be hard X-ray sources (see section 4.1). However, in the second observation (3.5 years later) these two Class I sources were found to The kinematic timescale corrected for the inclination for outflows from X-ray emitting protostars is around 5×10^4 yr, which is as same as the timescale of (2–5)$\times10^4$ yr for typical outflows (Levreault 1988; Wu, Huang, & He 1996). To investigate the evolutionary stage of X-ray emitting protostars in their outflow phase, we follow a scheme of a decline in the outflow force that was presented by Bontemps et al. (1996). For a low-mass protostar, the outflow force is reported typically $F_{CO} \sim 10^{-4}$ $M_\odot$ km s^{-1} yr^{-1} at the early Class 0 stage and $F_{CO} \sim 2 \times 10^{-6}$ $M_\odot$ km s^{-1} yr^{-1} at the late Class I stage. The force corrected for the inclination of the X-ray emitting protostars is of order 3×10^{-6} $M_\odot$ km s^{-1} yr^{-1}. Therefore, the observed four X-ray emitting protostars are in the late Class I stage according to this scheme.

be very faint (section 4.2). In contrast, we found a new hard X-ray source (> 2 keV) at the position of another Class I star YLW15.

Similarly, in the RCrA cloud, we found an apparent flux variations of the X-ray complex consisting of R2 and R1 in 2.6 years between the second and the third observations (section 5.2 and section 5.3). Other Class I sources in RCrA also showed long time variabilities in the three observations (see the Count rates in Table 5.1, Table 5.2 and Table 5.3).

We then conclude that hard X-rays from Class I protostars are highly variable over long time spans, and we suspect that the hard X-ray non-detection from the majority of Class I objects is, at least partly, due to the long-term time variability, in which duty ratio of high flux state would be small.

11.1.4 Geometry Effect: A Unified Picture ?

To search the characteristics of both detected and non-detected protostars further, we executed the observations of CO outflows toward five X-ray emitting protostar candidates in the ρ Ophiuchi region, collaborating with Sekimoto, Tatematsu, Umemoto, Koyama, Hirano, and Yamamoto.

We have carried out the outflow observations of ^{12}CO (J = 2–1) with the

Caltech Submillimeter Observatory, and ^{12}CO (J = 1–0) with the Nobeyama 45 m telescope for four Class I sources (EL 29, WL 6, IRS 44, IRS 46) and one Class II source (WL 10), which were firmly identified with the first observations (section 4.1). These infrared sources are located in the core region of the ρ Ophiuchi cloud, as defined by the C^{18}O (J = 1–0) emission (Wilking & Lada 1983). The X-ray (L_X) and infrared (L_{IR}) luminosities of these sources are $\sim 10^{30}$ ergs s^{-1} (section 4.1) and 0.3–48 $L_\odot$ (Wilking et al. 1989), respectively.

We found bipolar flows from four X-ray emitting YSOs out of the five samples (Figure 11.3). Since IRS46 is close to the outflow source IRS44, with a separation of 24 arcsecs, it is not clear whether or not the observed outflow belongs to IRS46 or IRS44. Terebey et al. (1989) observed the IRS 44/IRS 46 region with the Owens Valley Millimeter Interferometer of a beam size of 5–12 arc-sec, and detected a CO outflow from IRS 44, but not from IRS 46. Thus here, we assume that the outflow emission from IRS46 is at a negligible level in comparison with that from IRS44. The high detection rate (4/5) of outflows from the X-ray emitting protostars suggests that a low mass pre-main sequence star starts to emit X-rays in the outflow phase of stellar evolution. In surveys of T Tauri stars, outflows were detected from about 10% (Lada 1985). Bontemps et al. (1996) detected outflows from almost all (∼90%) Class I sources. Thus, we confirmed that the X-ray sources observed with ASCA are protostars which are in an earlier phase of stellar evolution than T Tauri stars.

The kinematical time-scale of the outflows from X-ray emitting protostars, after the correction of the inclination angle, is around 5×10^4 yr, which is nearly the same as that the time-scale of $(2\text{–}5)\times10^4$ yr for typical outflows (Levreault 1988; Wu, Huang, & He 1996). To investigate the evolutionary stage of X-ray emitting protostars in their outflow phase, we follow the scheme of Bontemps et al. (1996), which present a decrease of the outflow force along the evolutional phase. For a low-mass protostar, the outflow force is reported typically $F_{CO} \sim 10^{-4} M_\odot$ km s^{-1} yr^{-1} at the early Class 0 stage and $F_{CO} \sim 2 \times 10^{-6} M_\odot$ km s^{-1} yr^{-1} at the late Class I stage. The outflow forces of the X-ray emitting protostars, after the correction of the inclination angle, are all in the order $3\times10^{-6} M_\odot$ km s^{-1} yr^{-1}. Therefore, the observed four X-ray emitting protostars are in the late Class I stage according to this scheme.

The most notable feature of these out-flows is that the blue and red lobes show

compact feature; they are largely overlapped each other, suggesting nearly pole-on geometry (Figure 11.3). According to the three-dimensional outflow model by Cabrit & Bertout (1986, 1990), these outflows have an inclination angle of around 10° for a half-cone opening angle of 30°.

Apart from our CO observations, there are outflow observations which support the pole-on configuration of the X-ray emitting protostars. The molecular outflow from Class I source IRS 7 (=R1) in the R CrA cloud core (see also section 5.1) were observed by Levreault (1988) and Anderson et al. (1997). Since the blue and red lobes of the outflow overlap each other (see Fig 11.4; from Figure 4 in Anderson et al. 1997), we estimate the inclination angle is around 30°. The bright X-ray source, YLW 15 (=IRS 43: Class I), in the ρ Ophiuchi cloud (see also section 4.2) has also overlapped feature of blue- and red-lobes, which implies a nearly pole-on configuration (Bontemps et al. 1996; Figure 11.5). In Figure 11.3, Figure 11.4, and Figure 11.5, we summarize all the outflow features of detected protostars.

For comparison, we show the outflow features of non-detected sources in Figure 11.6 and Figure 11.7 and Table 11.1. All these have extended feature of blue- and red- lobes. It implies that we see the outflows from almost perpendicular angles. For example, the inclination angle of L1551 IRS 5 is larger than 55° (Ohashi et al. 1996), and that of VLA 1623 is 80°–85° (André et al. 1990).

We summarize the outflow features of protostars in Table 11.1. X-ray detected protostars show pole-on geometries in the outflow features, and there are no protostars which show edge-on geometries. On the other hand, non X-ray detected protostars show edge-on geometries, and there are no protostars which show pole-on configurations.

Consequently, we propose a unified picture with analogy of Seyfert I and II galaxies; every protostar emits X-rays, but the X-rays can only be detected from pole-on viewing angle, whose inclination angle is smaller than about 45°. In this geometry, the line of sight gas is mainly due to the relatively lower density of the bipolar flow and is not due to denser circumstellar disks. Thus hard X-rays are less absorbed. X-ray non-detected protostars have an edge-on geometry, on the other hand, hence X-rays are completely blocked by an extremely high column along the circumstellar disk.

It is quite natural that X-ray emitting protostars have a pole-on configuration, because a circumstellar gas disk absorbs even hard X-rays, if the X-rays are emitted

from the nearest part of the protostar. For hard X-rays at 5 keV, the optical depth becomes unity at a column density of 3×10^{23} cm^{-2} (Morrison & McCammon 1983). On the other hand, the column density of gas disks of protostars is reported to be more than 10^{24} cm^{-2}. For example, the circumstellar disk around the outflow source B335 is reported to have a column density of 1–6×10^{24} cm^{-2} (Hirano et al. 1992). Keene & Masson (1990) reported that a possible 65 AU circumstellar disk around L1551-IRS 5 has a column density of 6×10^{26} cm^{-2}, on the basis of 2.73 mm continuum observations.

It is noteworthy that two X-ray emitting protostars (EL 29 and IRS 44) are reported to have an extended circumstellar disk. Simon et al. (1987), using lunar occultation technique in the K-band, detected extended emission from EL 29 (7 mas $\sim$ 1 AU in diameter) and IRS 44 (80 AU in diameter) among the 18 young stars observed in the Taurus and Ophiuchus clouds. Zinnecker et al. (1986) also reported two symmetric components around EL29 with L-band speckle observations, a compact core with a diameter of about 8 AU and an extended halo with a diameter of 320–480 AU. These extended structures observed in the infrared may lend additional support for a nearly pole-on configuration of the circumstellar disk of these protostars, because symmetrically extended structure would be found in the case of a disk pole-on configuration.

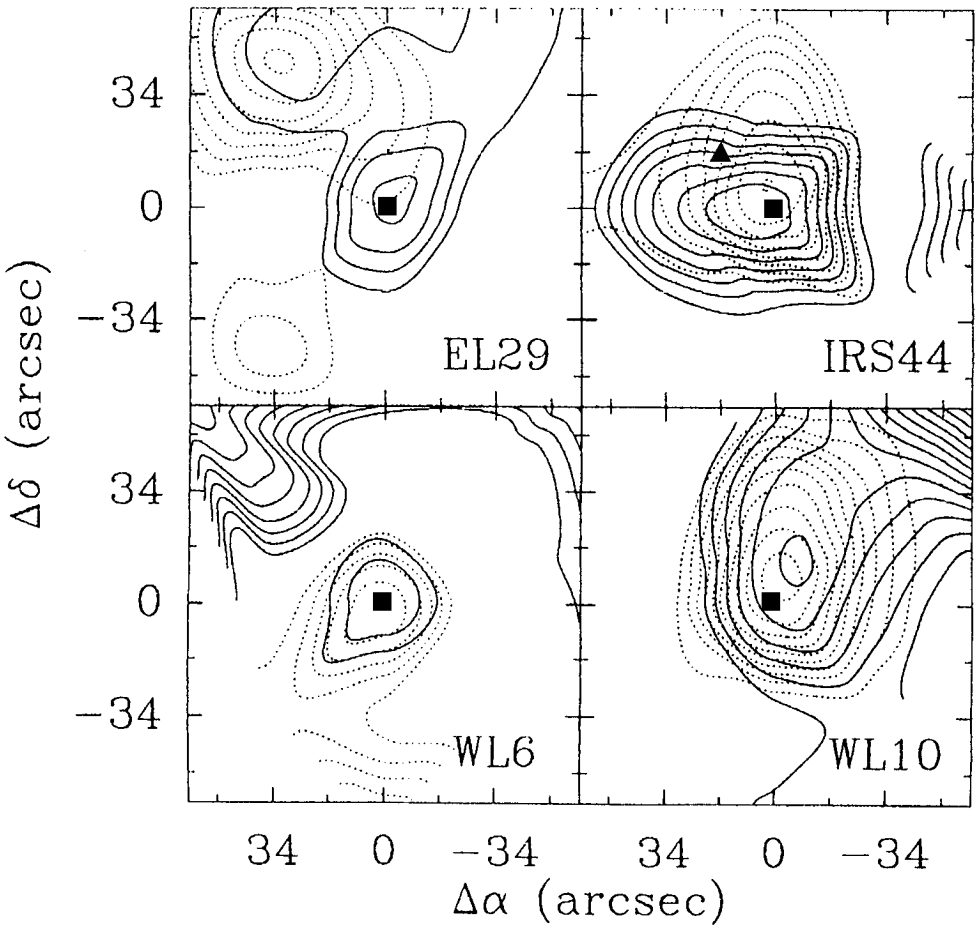

Figure 11.3: X-ray emitting protostars:
Integrated intensity CO ($J = 2-1$) maps of the blueshifted (solid contours) and redshifted (dotted contours) outflow emission for four X-ray emitting protostars. Filled squares show the positions of the infrared sources. A filled triangles shows the position of IRS 46. Integration ranges (lobe, velocity interval in km s^{-1}) and contours (lowest contour, step in K km s^{-1}) are as follows: EL 29: (blue, -4 to 0) (low 0.6, step 0.2) (red, 8 to 12) (low 1.5 step 0.5); IRS 44: (blue, -4.5 to -0.5) (low 0.6, step 0.2) (red, 9 to 13) (low 0.6 step 0.2); WL 6: (blue, -4 to 0) (low 0.6, step 0.2), (red, 7 to 11) (low 1.0 step 0.3); WL 10: (blue, -4 to 0) (low 0.9, step 0.3), (red, 7 to 11) (low 0.9, step 0.3).

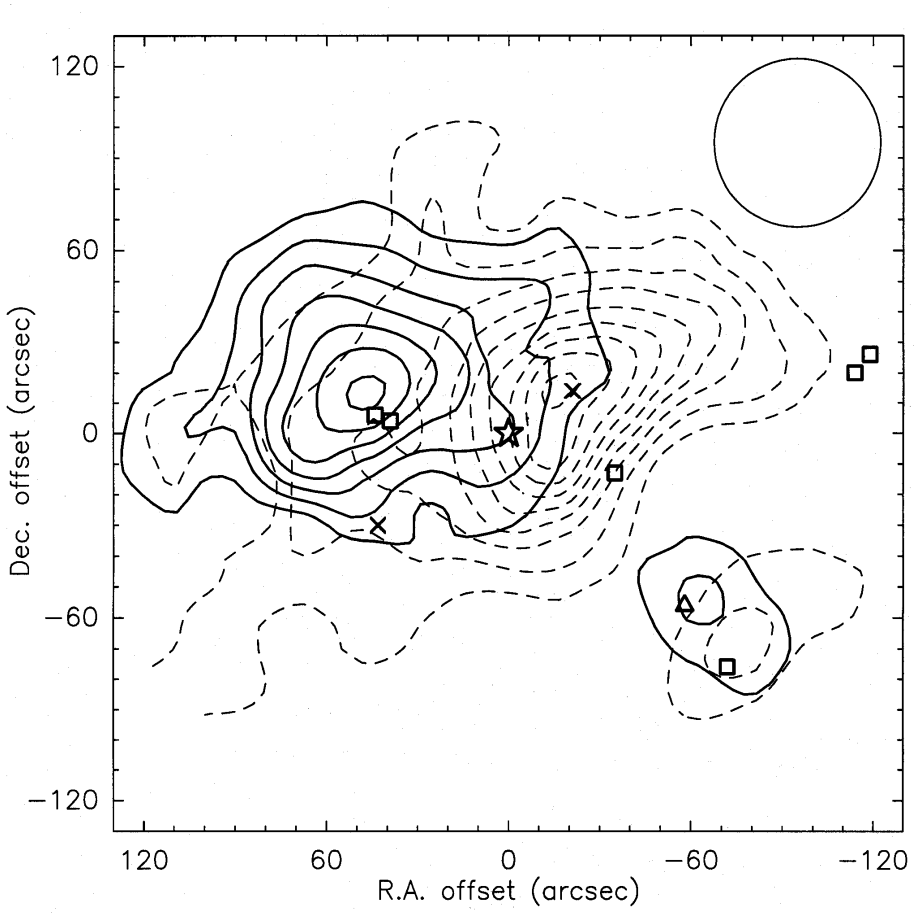

Figure 11.4: X-ray emitting protostar:
The $HCO^+(J = 1 - 0)$ outflows around X-ray emitting protostar RCrA IRS7 (=R1) (Anderson et al. 1998; Fig.4). The blue (full line contour) and redshifted (dashed line contour) outflows cover the velocity range $-15 \sim 0$ km s^{-1}, and $10 \sim 25$ km s^{-1} respectively. The contour levels are from 0.5 K km s^{-1} in increments of 0.5 K km s^{-1}. The location of the IRS 7 (=R5) is denoted by a star, the T Tauri star T CrA (left) and the Herbig Ae/Be star R CrA (right) are denoted by crosses, the Herbig-Haro objects are denoted by squares whilst the embedded infrared source HH100–IR is denoted by a triangle.

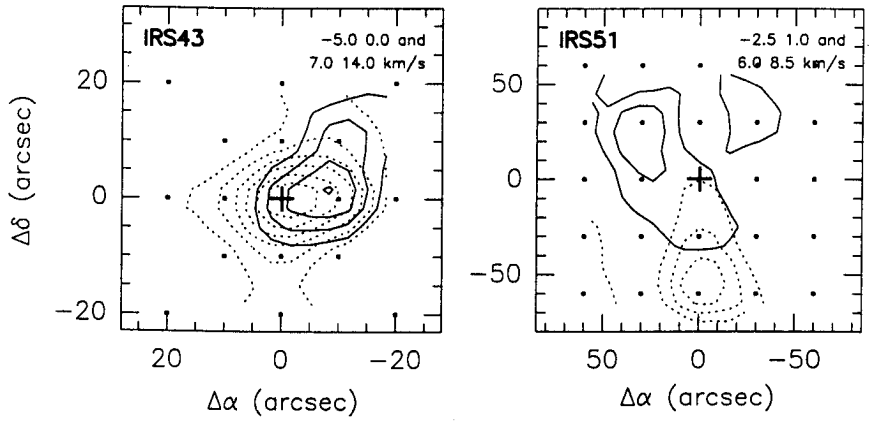

Figure 11.5: X-ray emitting protostars:
^{12}CO ($J = 2 - 1$) maps of the blue (solid contours) and redshifted (dotted contours) outflow emission for two X-ray emitting protostars (IRS43=YLW15 and IRS51). Positions of central YSOs marked by crosses; blue- and red- shifted integration intervals indicated in upper left corners. Sources, lowest contours, and contour steps (for the blue- and red-shifted emission, respectively) are: IRS43 (0.9, 0.5), (0.9, 0.5) K km s^{-1}, IRS51 (1.2, 0.4), (1.2, 0.4) K km s^{-1}. From Bontemps et al. (1996).

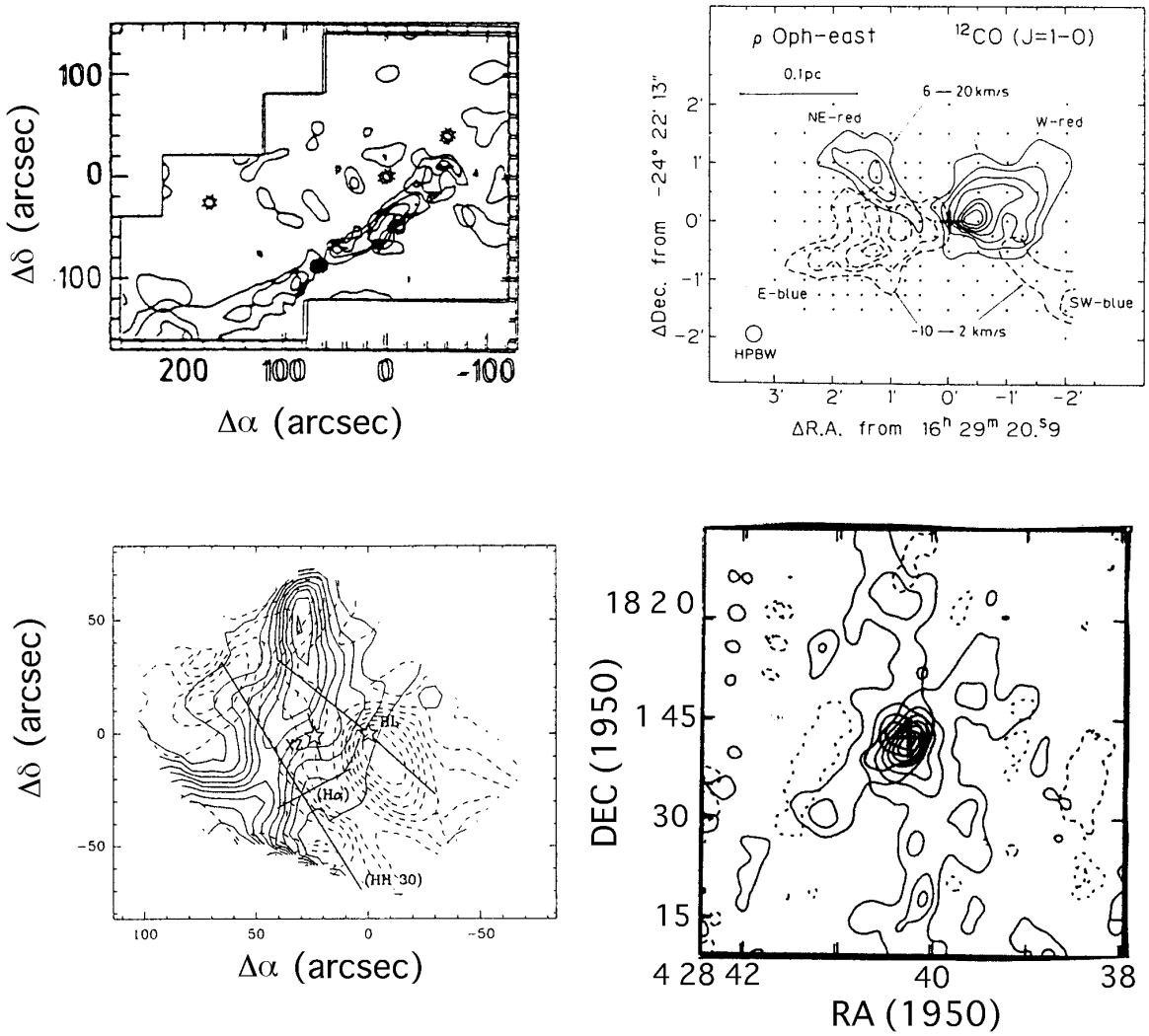

Figure 11.6: X-ray non-detected protostars:
Outflow maps of non-X-ray-detected protostars.
upper-left: VLA1623, André et al. (1990)
upper-right: IRAS 16293-2422 in RHo Oph, Mizuno et al. (1990)
lower-left: HL Tau Monin, et al. (1996)
lower-left: L1551 IRS5, Ohashi et al. (1996)

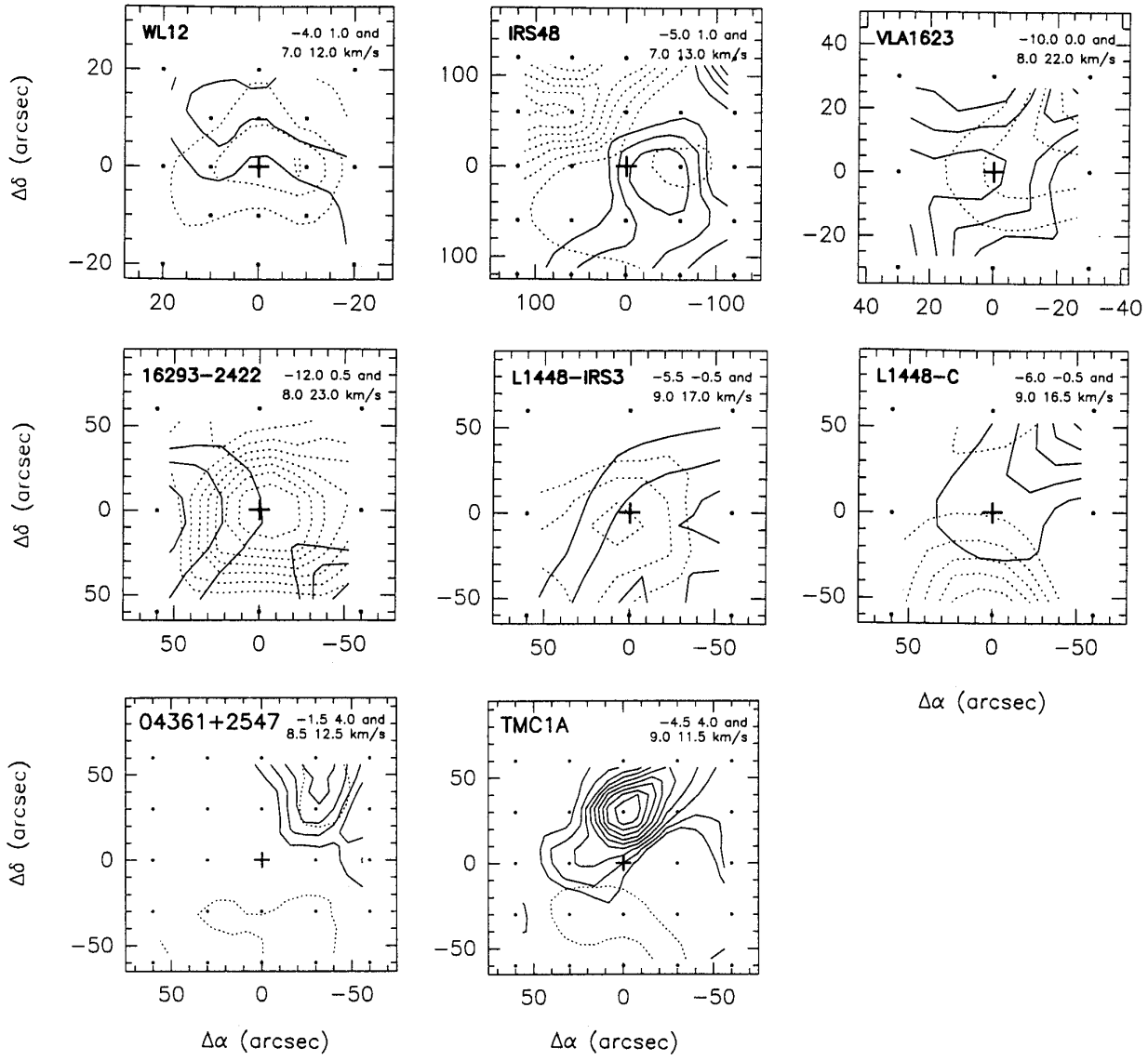

Figure 11.7: X-ray non-detected protostars:
^{12}CO ($J = 2 - 1$) maps of the blue (solid contours) and redshifted (dotted contours) outflow for eight X-ray emitting protostars (WL12, IRS48, VLA1623, IRAS16293-2422 in Rho Oph Core, L1448-IRS3, L1448-core in L1448, IRAS04361+2547, TMC1A=IRAS04365+2535 in Taurus). Positions of central YSOs marked by crosses; blue- and red-shifted integration intervals indicated in upper left corners. Sources, lowest contours, and contour steps (for the blue- and red-shifted emission, respectively) are: WL12 (0.8, 0.5), (0.7, 0.5) K km s^{-1}, IRS48 (2.0, 0.5), (2.0, 1.0) K km s^{-1}, VLA1623 (3.0, 1.5), (3.0, 1.5) K km s^{-1}, IRAS16293-2422 (8.0, 5.0), (10.0, 5.0) K km s^{-1}, L1448-IRS3 (1.2, 1.0), (2.0, 1.0) K km s^{-1}, L1448-core (1.4, 1.0), (2.0, 1.0) K km s^{-1}, IRAS04361+2547 (1.2, 0.5), (0.7) K km s^{-1}, TMC1A=IRAS04365+2535 (1.0, 0.6), (0.7) K km s^{-1}. From Bontemps et al. (1996).

11.1.5 Host Cloud Effect: Magnetic Field Orientation

In Table 11.3, we list the X-ray detection rate from protostars in each of the clouds. We see apparent difference of the detection rate from a cloud to cloud. For example, the detection rates in ρ Oph and RCrA are very high (50% and 80%, respectively), but we detected no protostars in Taurus, which is almost at the same distance to those of ρ Oph and RCrA.

Table 11.3: Detection rates of protostar candidates in each molecular cloud (2–10 keV band)

Distance	Field	Detection		
[pc]	Region(#†)	Yes	No	(%)
∼150	ρ Oph(2)	8	9	47
	RCrA(1)	5	1	83
	Taurus(4)	0	8	0
	Lupus(1)	0	0	–
∼300	Serpens(1)	1	2	33
	Perseus(2)	1	4	20
∼500	Orion(6)	4	19	17

†: Number of the field of view

There are some reports that all the magnetic fields in one cloud lie with the same orientation (e.g. Goodman & Heiles 1994 – Ophicus; Goodman et al. 1990 – Taurus, Ophicus), while we can not uniquely derive the direction of the magnetic field with only the observed polarization.

On the other hand, in the Table 11.1, we can see that all the outflow features measured in Taurus show extended feature (∼ edge-on geometry) and all the outflow feature in the ρ Oph main body and RCrA show overlapped, i.e., pole-on geometry.

Based on the above two results, although the measured samples are still limited, we can assume that most of the sources in Taurus have a edge-on geometry, while those in the ρ Oph main body and RCrA have a pole-on geometry. This scenario could at least partly explain the apparent difference of the detection rate from a cloud to cloud.

11.2 Mechanism of X-ray Flares

Like TTSs, we obtained some flares from protostars (EL 29, R1 and YLW 15). These X-ray flares imply that greatly enhanced magnetic activity, already well-established in older TTSs and the Sun, is present in the earlier protostellar phase. In this point of view, we discuss the flare properties on protostars.

11.2.1 Individual Flare (1) — EL29

In the first observation of the ρ Oph region (section 4.1), we detected X-ray flare from EL29. From the light curve, we estimated exponential decay time and the total energy. Since the decrease in the hardness ratio is attributable to a decrease of the plasma temperature, we could estimate the plasma density from the decay time beyond on the assumption of radiative cooling of a thin thermal plasma. We also estimated the flare loop length (assuming a single-loop) based on the analogy of a solar flare (van den Oord 1988) with aspect ratio (diameter/loop length) $a = 0.1$, and the $\Gamma = 1$ (ratio of the cross-section between the loop top and bottom). The detailed procedure is written in Appendix. The derived physical parameters are shown in Table 11.4. The electron density and flare loop length are $1{\times}10^{11}$ cm^{-3} and $3{\times}10^{11}$ cm, respectively. Assuming equilibrium between the thermal pressure and magnetic field pressure, we estimated the magnetic field strengths of the X-ray emitting plasma to be 200 Gauss. The electron density and magnetic field strength is comparable to those of solar flares, but the loop size is 1–3 orders of magnitude larger; it is larger than solar radius.

Table 11.4: Flare parameters of EL 29.

Source	τ	$L_{X,peak}$ (2–10 keV)	E_{tot} (2–10 keV)	n_e	l	B
	[ks]	[10^{31} erg s^{-1}]	[10^{36} erg]	[10^{11} cm^{-3}]	[10^{11} cm]	[G]
EL 29	8.3	5.4	0.4	1	3	200

τ: e-folding time of the lightcurve decrease; $L_{X,peak}$: X-ray luminosity in 2–10 keV band at the flare peak; E_{tot}: X-ray total energy emitted by the flare during its cooling phase in 2–10 keV band; n_e: electron density; l: loop length; B: minimum value of the magnetic field confining the loop plasma

11.2.2 Individual Flare (2) — YLW15

In the second observation of the ρ Oph region (section 4.2), we have discovered a peculiar time behavior from YLW15: quasi-periodic flares. Here we examine the relation between each of the flares and the physical conditions, then discuss the origin of the quasi-periodic flares.

Physical Conditions of the Triple Flare

If the three intermittent flares are attributed to a single persistent flare, with the three events due to geometrical modulation, such as occultation of the flaring region by stellar rotation or orbital rotation of the inner disk, then only the emission measure should show three peaks and the temperature would smoothly decrease during the three flares. However, in our case, we see the temperature follows the same pattern as the luminosity, decreasing after each jump at the peaks, as indicated in Table 4.5 and Figure 4.4. To test further, we fitted the data in phases 1–8 with a single exponential decay model, and confirmed that it is rejected with 89 % confidence. We then interpret the 2–10 keV variability of YLW15 as due to a triple flare, in which each flare followed by a cooling phase. Now, we label the phases 1–3, 4–6, and 7–8 as Flare I, Flare II, and Flare III, respectively, and discuss separately. We focus on the cooling phases to estimate the physical conditions of the plasma in each flare.

Flare I

Here we assume that the plasma responsible for Flare I is confined in one semi-circular magnetic loop with constant cross section along the tube flux, with length L, and diameter-to-length (aspect) ratio a, based on the similarity between stellar and solar flares, and on the analogy of the solar flares.

To the decay of Flare I, we apply a quasi-static cooling model (van den Oord & Mewe 1989), in which the hot plasma cools quasi-statically as a result of radiative (90 %) and conductive (10 %) losses (see detailed comment in Appendix §1). If the loop indeed cools quasi-statically, the temperature T and the emission measure (EM) must satisfy the relation $T^{13/4}/EM = cst.$

We calculate the values of $T^{13/4}/EM$ for the three successive bins (phases 1–3) of Flare I to be $(T/10^7\,\mathrm{K})^{13/4}/(EM/10^{54}\,\mathrm{cm}^{-3}) = 61 \pm 55,\ 59 \pm 42,\ 25 \pm 18.$

These values are consistent with a constant value within the rather large errors. In fact, we fit the data to the quasi-static model, and get satisfactory values of χ^2_{red} for the count rates, temperature, and emission measure (see Table 11.5 panel 1).

Thus we conclude that our hypothesis of quasi-static cooling is well verified; an underlying quiescent coronal emission may not be required. From the peak values of T and EM, and the quasi-static radiative time scale, we derived loop parameters as listed in Table 11.6. The detailed procedure is written in Appendix. The value of 0.07 found for a is within the range for solar active-region loops ($0.06 \leq a_{\odot} \leq 0.2$, Golub *et al.* 1980), which supports the initial assumption that the flare is due to a solar-type activity.

Flares II and III

The appearance of Flare II can be interpreted either by the re-heating of the cooling plasma during Flare I, or by the heating of a plasma different from that of Flare I. In the latter case, the lightcurve and EM would be the sum of Flare I component and new flare component. The EM of the new flare component can be derived by subtracting the component extrapolated from Flare I. The derived EM are 1.6±0.4 (phase 4), 2.5±0.8 (phase 5), and 1.9±1.5 (phase 6). Then we fitted the lightcurve and EM with the quasi-static model assuming the above two possibilities. However, in both of the cases, the model did not reproduce the lightcurve and EM simultaneously, and the quasi-static cooling model cannot be adopted throughout the triple flare but Flare I.

For simplicity, we fitted the parameters in Flare II with an exponential model. The best-fit parameters are shown in Table 11.5, and each models for the reheating and the distinct flare assumptions are shown by the dashed and the dotted lines in Figure 4.4, respectively. The obtained χ^2_{red} and the timescale for each lightcurve and EM were similar between the two assumptions. Therefore both of the possibilities cannot be discriminated. As for EM, both of the fits show no decay or very long time decay, which is not seen in the usual solar flares. The constant feature in EM makes the quasi-static model unacceptable. Since we cannot derive the aspect ratio of Flare II by fitting with quasi-static cooling model, assuming the ratio derived in Flare I and that radiative cooling is dominant, we deduced the plasma parameters as shown in Table 11.6. Here, we derived the values assuming the reheating scenario

(the former assumption). The results show that the plasma density and the volume remain roughly constant from Flare I. This supports that Flare II resulted from reheating of the plasma created by Flare I.

As for Flare III, because of the poor statistics and short observed period, the fits to lightcurve with the exponential model give no constrain between the above two possibilities. The fitting results are shown in Table 11.5 and Figure 4.4. We derived the plasma parameters of Flare III doing the same procedure for Flare II, as shown in Table 11.6. These values are similar to those in Flare I and II. All these results support the scenario that a quasi-periodic reheating makes the triple flare. The heating interval is $\sim$20 hour. The loop size is approximately constant through the three flares and is as large as $\sim$14 $R_{\odot}$. The periodicity and possible large-scale magnetic structure support a scenario that differential rotation between a central star and inner disk twisted magnetic field lines, which confine a high temperature plasma in the loop, then by the re-connection of the field line, the same plasma is reheated periodically (e.g., Hayashi, Shibata, & Matsumoto 1996).

Such a quasi-periodic reheating has never been detected in the other protostar candidates. The reason is thought because there have been no other observation of star forming region executed for such a long time as this observation of Rho Oph. We suspect that other protostars can have such a quasi-periodic flares, when they are active phase.

Table 11.5: Fitting of cooling phase of flares from YLW15

fit analytical expression (F)	F	α	F_p	τ [ks]	χ^2_{red} (d.o.f.)
[1]	[2]	[3]	[4]	[5]	[6]
$F_{1,qs}(t) = F_p \times \{1 + (t - t_1)/3\tau\}^{-\alpha}$	I [cnts ks^{-1}]	4	172 ± 5	31 ± 1	0.8 (45)
	kT [keV]	8/7	5.6 ± 0.6	[31]	0.5 (2)
	EM [10^{54} cm^{-3}]	26/7	10.4 ± 0.9	[31]	0.4 (2)
$F_2(t) = F_p \times exp\{-(t - t_2)/\tau\}$	I [cnts ks^{-1}]	–	62 ± 3	33 ± 3	1.7 (47)
	kT [keV]	–	4 ± 1	50 ± 20	1.5 (1)
	EM [10^{54} cm^{-3}]	–	3 ± 1	> 53	0.4 (1)
$F_{1+2}(t) = F_{1,qs}(t) + F_2(t)$	I [cnts ks^{-1}]	–	46 ± 3	29 ± 2	1.6 (47)
	EM [10^{54} cm^{-3}]	–	1.6 ± 0.8	> 54	0.6 (1)
$F_3(t) = F_p \times exp\{-(t - t_3)/\tau\}$	I [cnts ks^{-1}]	–	35 ± 2	58^{+24}_{-13}	1.4 (24)
	kT [keV]	–	5 ± 3	55 (> 16)	$\chi^2 = 0$ (0)
	EM [10^{54} cm^{-3}]	–	2.5 ± 0.7	71 (> 23)	$\chi^2 = 0$ (0)
$F_{1+2+3}(t) = F_{1+2}(t) + F_3(t)$	I [cnts ks^{-1}]	–	28 ± 2	63 ± 15	1.4 (24)

Panel 1 gives the quasi-static fit for Flare I. Panel 2 (Panel 3) gives the exponential fit for Flare II (Flare III): first assuming that the flares are reheating of the same plasma volume as the previous flare; second assuming that the three flares are independent (the previous flares contribute to the latter flares). $t_{\rm I}$, $t_{\rm II}$, and $t_{\rm III}$ are the beginning time of Flare I, II, and III, respectively. We assume only positive values for the decay time (Column [5]). The errors are at 90 % confidence level.

Table 11.6: Physical properties for the triple flare from YLW15

Flare #	a	l [$R_\odot$]	n_e [10^{11} cm^{-3}]	B [G]	$L_{X,peak}$ [10^{31} erg s^{-1}]	τ [ks]	E_{tot} [10^{36} erg]
1	0.07±0.02	14±2	0.5±0.1	150±20	20±1	31±1	6.0±0.5
2	[0.07±0.02]	11±5	0.4±0.1	120±30	8±1	33±3	2.8±0.6
3	[0.07±0.02]	15±10	0.3±0.2	100±60	4.6±0.5	58^{+24}_{-13}	2.7±1.0

a: diameter-to-length ratio of the loop; L: loop length; n_e: electron density; B: minimum value of the magnetic field confining the loop plasma; $L_{X,peak}$: X-ray luminosity at the flare peak in the 0.1–100 keV band; τ: characteristic decay time of the lightcurve; E_{tot}: total energy released during the cooling phase in X-ray wavelength.

11.2.3 kT vs. EM

Recently, Shibata & Yokoyama (1999) reexamined Feldman et al. (1995) 's correlation between flare temperature T and emission measure $EM = n^2V$, by including solar micro flares observed by Yohkoh (Shimizu 1995) and two YSO's flares obtained with ASCA (V 773 Tau: Tsuboi et al. 1998, R1 in RCrA: Koyama et al. 1996). As a result, they found that the correlation is well represented by the power-law relation, $EM \propto T^a$ with power-law index $a \simeq 8.3 \pm 1.0$. The universal correlation is well explained with their model on the basis of magnetic reconnection with heat conduction and chromospheric evaporation, assuming that the gas pressure of a flare loop is comparable to the magnetic pressure. The theory predicts the relation $EM \simeq 10^{46}\ (B/15\mathrm{G})^{-5}\ (\mathrm{n}_e/10^9\ \mathrm{cm}^{-3})^{3/2}\ (T/10^7\ \mathrm{K})^{17/2}\ \mathrm{cm}^{-3}$. The interesting point is that all the observational data points, including close binary flares (RS CVn system – F–G dwarf + K subgiant: π Peg from Doyle et al. 1991 and UX Ari from Tsuru et al. 1989; Algol – B 8V + K2IV from Stern et al. 1992), lie on the line of around B = 5–15 G. The predicted magnetic field strength predicted by them (5–15 G) is about 10 times smaller than those estimated for solar and stellar flares (e.g. Tsuneta 1996, Ohyama & Shibata 1998, Tsuboi et al. 1998). However, it should be noted that their estimated value refers to only "average" strength of "dissipated component" of magnetic field. (That is, the reconnection could be partial.)

We confirm the relation to the flare data of T Tauri stars which we detected in this survey. We added three TTS data; one is a flare on ROXs7 (at PV phase in Rho Oph region: subsection 4.1), and the others are the flares on ROXs21 and SR24N (at AO6 in Rho Oph region: section 4.2). We analyzed them using GIS data and show the results in Figure 11.8. We see all the T Tauri stellar flares lied on the power-law relation around B$\sim$5G (see Figure 11.8). We thus demonstrated for the first time that the diagram of Shibata & Yokoyama (1999) provides further support on the magnetic reconnection scenario for the flare of T Tauri stars.

The next, we plotted the flare property of protostars on the same diagram. Figure 11.8 shows the log-log plot. From this plot, we confirmed that the protostars indicated by filled squares lie also on the "universal correlation" around B$\sim$5G, and then we conclude the X-ray flares from protostars are most likely originated by magnetic reconnection as well as the other cool stars.

11.2.4 Flare Scales

Although we had evidence that X-ray flares of protostars originate magnetically, it is not clear where the protostellar magnetic fields are generated. Then we here compare the physical properties of the protostellar flares with those of the other cool stars.

For the samples of cool stars, we selected bright flare sources including RS CVns as seen in Table 11.7. All the flare sources have a well-determined temperature using a wide range of energy band of $Tenma, Ginga$, and $ASCA$ satellites. The densities and volumes for all the sources were derived assuming that radiative cooling is dominant.

As a result, we found that the three flares occured on the YLW15 are on the high end of the energy distribution for protostellar flares, with total energies in excess of 3–6 $\times 10^{36}$ ergs. Although the plasma densities, temperatures, and then derived equipartition magnetic fields are typical of stellar X-ray flares, the emitting volume of the triple flare is huge; it exceeds the volumes in binary systems of RS CVns by a few orders of magnitude. The large size of this magnetic structure would be correspondent with a star-disk scale, and then at least in the case of the triple flare on the YLW15, a star-disk interaction in protostars would be implied.

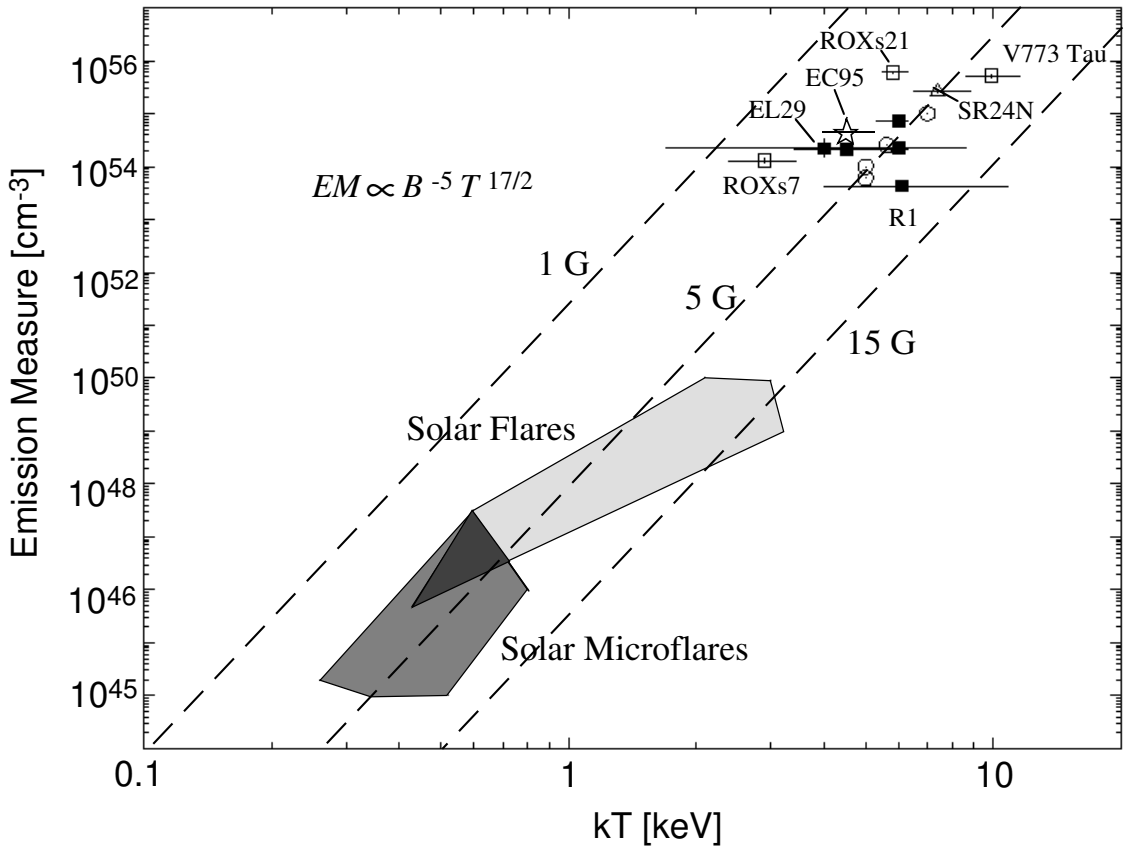

Figure 11.8: log-log plot of emission measure (EM) vs. plasma temperature (kT) of solar flares (from Feldman et al. 1995 and references therein), solar microflares observed by Yohkoh SXT (from Shimizu 1995), four stellar flares (open circles: from Feldman et al. 1995 and references therein), three flares on Class IIIs (open squares; V 773 Tau from Tsuboi et al. 1998, ROXs7 from Kamata et al. 1997, ROXs21 in this work), a flare on Class II (open triangle; SR24N from this work), five flares on Class Is (filled squares; R1 in R CrA from Koyama et al. 1996, EL 29 from Kamata et al. 1997, the untitled three filled squares are three flares on YLW 15 in chapter 3). The $EM - T$ relation curves based on equation [$EM \propto B^{-5}T^{17/2}$: Shibata & Yokoyama 1998] are also plotted for $B = 1$, 5, and 15 G.

Table 11.7: Comparison with the other flares

Source	SED	n_e $[10^{11}\,\mathrm{cm}^{-3}]$	V $[10^{33}\,cm^3]$	τ [ks]	kT_{peak} [keV]	EM_{peak} $[10^{55}\,\mathrm{cm}^{-3}]$	E_{tot} $[10^{36}$ erg]	ref.
YLW15(I)	I	0.5	3	31	6	0.7	6	
YLW15(II)	I	0.4	2	33	5	0.3	3	
YLW15(III)	I	0.3	2	58	4	0.2	3	
EL29	I	1	0.2	8	4	0.3	0.4	
RCrA	I	1	0.04	20	6	0.04	0.2	(1)
SR24N	II	5	0.1	6	7	3	6	
ROXs31	III	3	0.6	7	6	6	13	
ROX7	III	3	0.01	6	3	0.1	0.1	
V773Tau	III	3	0.6	8	10	5	8	(2)
Algol		1	0.09	20	5	0.1	0.6	(3)
π Peg		8	0.006	2	6	0.3	0.2	(4)
AU Mic		6	0.002	2	5	0.06	0.03	(5)

reference: (1) Koyama et al. 1996 and Hamaguchi private comm.

(2) Tsuboi et al. 1998

(3) Stern et al. 1992

(4) Doyle et al. 1991

(5) Cully et al. 1993

11.3 Emission Mechanism of Persistent X-rays

We detected some protostars in non-flare state. The spectra have line emission from highly ionized iron ($\sim$ 6.7 keV) and are well fitted by thin thermal plasma model.

11.3.1 L_X vs. V sin i

From protostar WL6, we obtained suggestive time variability; sinusoidal light curve with constant temperature (section 4.1). It can be interpreted due to the spin period of a protostar. If the sinusoidal modulation of WL 6 is really due to the spin of the central star, the period is only about one day which is shorter than those of the other evolutional stage (TTSs: $\sim$3–7 day, Sun: $\sim$28 day).

In low-mass stars, a relation between L_X vs. V sin i has been known (Pallavicini et al. 1981, Feigelson et al. 1993). Assuming the spin period of 1 day and stellar radius of $1R_{\odot}$, we estimated V sin i of the protostars, then plot the quiescent X-ray properties of in the diagram. We see that all of the protostar data lie on the same line of the correlation obtained with more evolved low mass stars (Figure **??**). Thus the quiescent X-rays from protostars are most likely to be originated by magnetic reconnection as well as the more aged low mass stars.

From protostar WL6, we obtained suggestive time variability; sinusoidal light curve with constant temperature (section 4.1). It can be interpreted due to the spin period of a protostar. If the sinusoidal modulation of WL 6 is really due to the spin of the central star, the period is only about one day, and then apparently shorter than those of the other evolutional stage (TTSs: $\sim$3–7 day, Sun: $\sim$28 day).

In low-mass stars, a relation between L_X vs. V sin i has been known (Pallavicini et al. 1981, Feigelson et al. 1993). Then assuming the spin period, we plot the quiescent properties of protostars in the diagram, and we found that all of them lie on the correlation (Figure 11.9). Thus the quiescent X-rays from protostars are most likely to be originated by the magnetic reconnection process, which is proposed for the older low-mass stars (e.g. TTSs, main sequence stars).

11.3.2 kT vs. EM

To investigate the origin for persistent X-ray further, we made the same log-log plot of emission measure (EM) vs. plasma temperature (kT) as that in subsection 11.2.3, but for the data in the quiescent phase of protostars. The diagram is shown in Figure 11.10.

In the Figure 11.10, we see rather horizontally scattered plot than that in the flare phase (Figure 11.8). The temperatures of protostars are systematically higher than those of TTSs, and we see a correlation of $EM \sim$ constant.

If the origin of the quiescent X-rays in these YSOs are integrated emissions of small flares, the deviation of emission measure of WTTSs from the line [B$\sim$5G] indicates that WTTSs should have a larger number of smaller flares than those of protostars. However, one puzzle is that the temperature of protostar in quiescent is comparable to that in the flare phase, and the X-rays are explained by only one large flare. Therefore we might require the modification of mini-flare model for the quiescent X-rays from the protostars.

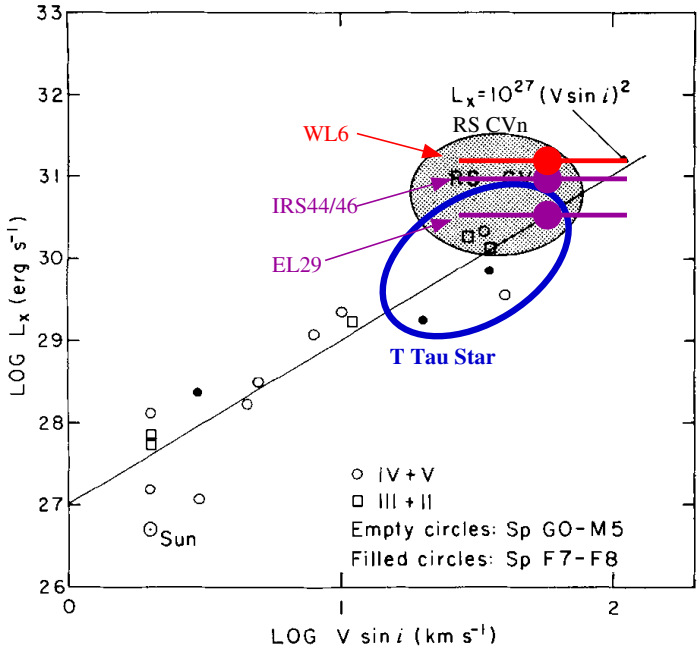

Figure 11.9: L_X vs. V sin i diagram of main sequence low-mass stars (Pallavicini et al. 1981) T Tauri stars (Feigelson et al. 1993), and protostars (this work) in quiescent state. Protostars are shown by filled circles. The properties are obtained by assuming spin period of 1 day (WL6) and $R_* = 1^{+1}_{-0.5} R_\odot$.

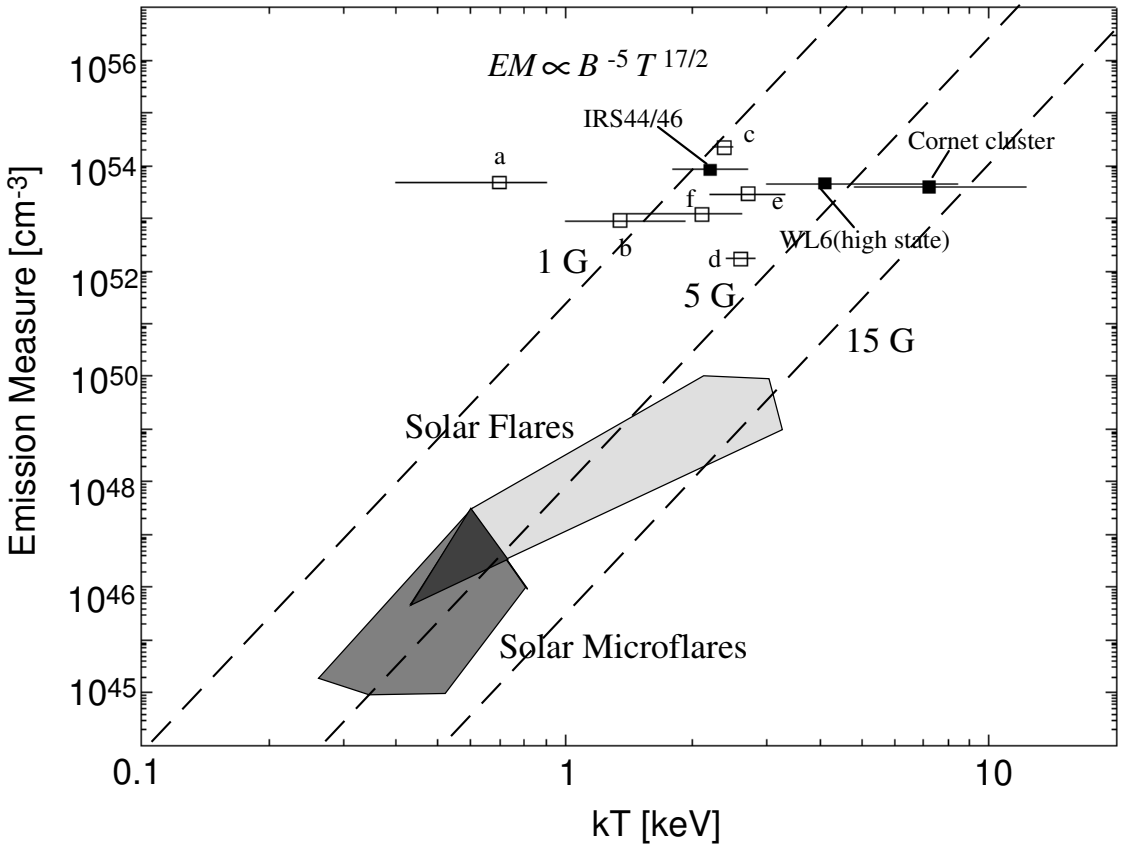

Figure 11.10: log-log plot of emission measure (EM) vs. plasma temperature (kT) of quiescent X-ray of YSOs overlaid with solar flares (from Feldman et al. 1995 and references therein), solar microflares observed by Yohkoh SXT (from Shimizu 1995). Filled squares indicate Class I protostars (WL6 and IRS 44/46 in Rho Oph – section 4.1, Cornet cluster in R CrA– Koyama et al. 1996). Open squares indicate five Class IIIs (a: ROX21, b: ROX7, c: ROX8 in Rho Oph – this work, d: CrA1 in R CrA – Koyama et al. 1996, e: Ced 110, f: CHX10a in ChaI – Yamauchi et al. 1998). The stellar mark indicates the proto-Herbig Ae/Be star EC95 see section 8.1. The $EM - T$ relation curves based on equation [$EM \propto B^{-5}T^{17/2}$: Shibata & Yokoyama 1998] are also plotted for $B = 1$, 5, and 15 G.

11.4 Intermediate-mass Protostars

We would like to note the X-ray emission from one "proto-Herbig Ae/Be star" EC95. EC95 lies in Serpens cloud (section 8.1), and is believed to be intermediate-mass protostar. We detected it in both soft and hard band. We found that the EC95 has temperature of about 5 keV, which is higher than the typical temperature of TTSs in quiescent state; it is comparable to the temperatures of protostars in quiescent state.

The X-rays from intermediate-mass stars are already big puzzle, because they are believed to have no convective zone on the stellar surface, then the magnetic origin have been hard to explain the X-rays. Also, the shock heating of the stellar winds can not explain the X-ray temperature, because the wind velocity is only about 100 km s^{-1} at most. From EC95, we obtained a hint of time variability like contiguous small flares.

Then assuming that the emissions mainly come from one flare at each moment, we plot the properties on the log-log plot (Figure 11.8) of emission measure (EM) vs. plasma temperature (kT). On the diagram, EC95 lies on the universal correlation. Then we conclude that the origin of the X-ray from EC95 is the same as those of low-mass protostars – magnetic origin. Medium-mass stars might have magnetic activities only in the youngest phase, which are amplified in convective zone of the star itself, or in the boundary layer between the star and the circumstellar disk.

Chapter 12

Summary

We have conducted an X-ray survey of 17 fields (totally 24 observations) in nearby star forming regions. 40% of the protostar candidates are detected with $S/N > 5$ level in the 2–10 keV band, while in the soft band, the detection rate is less than 5%.

- In the Orion molecular cloud 2–3 region, we obtained a hint for the hard X-rays from Class 0 protostars.
- Both bolometric luminosities of the X-ray detected and non-detected protostar candidates range from 0.1 to 50 solar luminosity. Thus no systematic difference of the the bolometric luminosity is found between the X-ray detected and non-detected protostar candidates.
- Hard X-rays from protostars are variable over long time spans. Then the no hard X-ray from many Class I objects is, at least partly, due to the long-term time variability.
- X-ray detected protostars showed pole-on geometry in the outflow features, while X-ray non-detected protostars showed edge-on geometry (non-overlapped feature in outflow), without exception. X-ray non-detection from edge-on protostars would be due to the complete blocking of X-rays by an extremely high column along the circumstellar disk.
- Following the detection of protostellar flare from R1 in R CrA, we detected flares from EL 29 and YLW 15 in Rho Oph. Plotting on the (kT vs. EM)

diagram, we found that all the flares lie on the "universal" power-law correlation which hold among cool stellar flares. Then we conclude that the X-ray flares from protostars are most likely originated by magnetic reconnection as well as the other more evolved cool stars.

- YLW 15 showed quasi-periodic flares which occurred every ∼20 hours. It is consistent with quasi-periodic reheating of the same plasma loop of $\sim 14\,R_\odot$ with diameter-to-length ratio $a \sim 0.07$. The derived large-scale magnetic structure and the observed periodicity imply that the reheating originates in a star-disk interaction caused by a differential rotation between them.

- WL 6 showed time variability, which is not flare-like, but is sinusoidal modulation with constant temperature. This implies the rotation of protostar. The period of one day is apparently shorter than the spin periods in the more evolved stage (TTSs, Sun).

- Taking the period of WL6 to be a typical spin period of protostars and assuming stellar radius of $1R_\odot$, we plot the data of protostars in the quiescent state on the (L_X vs. V sin i) diagram, and found that they lie on the correlation which holds in cool stars generally. This result implies that the quiescent X-rays from protostars are due to magnetic origin as those in the more evolved low mass stars.

- Plotting the properties in the quiescent state on the (kT vs. EM) diagram, we found a relation of $EM \sim$ constant. Temperatures of protostars are systematically higher than those of TTSs. If we adopt the universal correlation in flare X-rays, the temperature and EM of protostar in the quiescent state should be originated from a few number of large flare, which contradict to the quiescent flux. Therefore we might require the modification of the mini-flare model in quiescent state.

- We detected X-rays from a intermediate-mass protostar EC95, which exhibited time variability like contiguous flares, and high temperature. Plotting on the (kT vs. EM) diagram, we confirmed that it lies on the universal correlation which holds among flare sources. Then we interpret that the origin of X-rays from EC95 is the same as that of low-mass stars – magnetic origin.

Acknowledgments

I am indebted to many people for their help with this thesis.

I would like to express my largest gratitude to Prof. K. Koyama for his continuous advice and encouragement including on the attitude as a scientist throughout 5 years of my graduate course.

I am much obliged to Drs. Y. Sekimoto, K. Tatematsu, T. Umemoto, N. Hirano, S. Yamamoto and Mr. Y. Asou for the fruitful collaboration between X-ray and radio observations. I wish to express my thanks to Prof. K. Shibata, Dr. Mitsuru Hayashi, and Dr. T. Yokoyama for their useful discussions on the solar and stellar flares. I am grateful to Profs. T. Montmerle, E. D. Feigelson, and Mr. N. Grosso for our nice collaboration and stimulating me and giving useful advice on X-rays from protostars. I appreciate Prof. Masahiko Hayashi and Dr. N. Kobayashi who invited me to the exciting world of star formation and advised me from radio and infrared sides. I would like to thank Drs. S. Yamauchi, M. Itoh, and S. Skinner for their valuable comments on the X-ray analysis of star forming regions. I wish to thank Drs. H. Awaki, and T. Tsuru for their continuous guidance and advice both in scientific and experimental sides.

My fruitful and cheerful graduate course owes much to following people. I would like to thank Drs. S. Ueno, I. Hayashi, M. Ozaki, H. Matsumoto, Y. Maeda, H. Tomida, Mr. M. Sakano, Ms. M. Nishiuchi, Mrs. K. Hamaguchi, H. Murakami, J. Yokogawa, K. Imanishi, and M. Tsujimoto, for their encouragement, technical help and discussions. I also thank all the members of the infrared group in our cosmic-ray laboratory for new topics on the infrared field. I am grateful to Prof. Maihara for providing me enjoyable suggestions relating to various aspects of astrophysics. I thank Dr. Sogawa for the useful comments on magnetic fields in molecular clouds and Dr. Terada for discussion for intermediate-mass YSOs. I express thanks to Ms. Y. Nakakoji for her warm help on a lot of office work.

I thank all the members of the *ASCA* team for their support for this study. All the observational data were obtained by the members of the *ASCA* team. I am indebted to the staff of the *ASCA* Guest Observers Facility. My analysis was mainly performed

using the FTOOLS and XANADU packages, which were provided by GSFC/NASA. This research has made by using the HEASARC database, SkyView service (GSFC/NASA), the NASA Astrophysics Data System abstract service and the IPAC/NASA extra galactic database (NED). I am also grateful to the XRT-*ASCA* simulation team who has enabled me to create the appropriate response file utilized in the present thesis. Some figures were created using the IDL & DISPLAY45 software packages.

I acknowledges the award of Research Fellowship of the Japan Society for Young Scientists.

Appendix A

Determination of Physical Parameters of the Flares

A.1 Loop Parameters

Since some parts of our analysis are based on the model of Van den Oord & Mewe (1989, hereafter VM), which has been generally applied to a flare decay for solar-type flares, we briefly review the VM model here. VM assumes that the thermal energy in a plasma is decreased by radiative and conductive losses with respective time constant of τ_r and τ_c. Then the decay time is given as $1/\tau_{eff} = 1/\tau_r + 1/\tau_c$. VM further assume that the flare light curve and temperature decrease exponentially with decay times τ_d and τ_T, respectively. This effective cooling time is related to observed time scales by $1/\tau_{eff} = 7/8\tau_T + 1/2\tau_d$. We assume here that the flare occurs in only one semi-circular loop with a constant cross section along the tube flux. The geometrical parameters are: radius R ($R = L/\pi$; length L), diameter-to-length ratio a, and volume V. VM gives a relation of L versus a, depending on τ_{eff}, the temperature and the emission measure (hereafter EM), and the ratio τ_r/τ_c. Note that the relation is applied in any time interval during an assumed exponential decay epoch of the light curve and temperature.

Due to the limited photon number, we usually use the time averaged temperatures (T) and the EMs. For example, we have: $\overline{T} = \int_{t_i}^{t_f} T(t')\,dt'/(t_f - t_i)$, where t_i and t_f are, respectively the start and stop times to accumulate the data for estimating the temperature.

We now have a relation between L and a, but the ratio τ_r/τ_c is uncertain, and

it might even change during the decay of the flare. Therefore, we assume that the flare volume cools quasi-statically, or evolves through a sequence of *quasi-static equilibrium*, in which the plasma loop satisfies a scaling law, and $\tau_r/\tau_c = cst$.

The dependency of τ_r and τ_c on the temperature and EM, and relation of $\tau_r/\tau_c = cst$ lead to the relation of $T^{13/4}/EM = cst$.

VM analytically gives several physical quantities versus time, which all depend on the quasi-static radiative time scale ($\tau_{r,qs}$). The time scale $\tau_{r,qs}$ can be estimated from the light curve which must be proportional to the radiative loss. The T and EM should be fitted to the above relation using this value of $\tau_{r,qs}$. Then we can give the peak values $kT_{p,qs}$, $EM_{p,qs}$ (see Col. [4]–[5] in our Table 11.5 panel 1 for details).

Using the expressions for the radiative time (eq.[23a] of VM), the EM (eq.[3] of VM) and the scaling law (SL[2], eq.[196] of VM), we obtain the loop characteristics for the quasi-static model:

$$a = 1.38 \times (\tau_{r,qs}/10\,ks)^{-1/2} \times (kT_{p,qs}/keV)^{-33/16} \times (EM_{p,qs}/10^{54}\,cm^{-3})^{1/2}, \quad (A.1)$$

$$L = 1.0\,R_\odot \times (\tau_{r,qs}/10\,ks) \times (kT_{p,qs}/keV)^{7/8}, \quad (A.2)$$

$$n_e = 4.4 \times 10^{10}\,cm^{-3} \times (\tau_{r,qs}/10\,ks)^{-1} \times (kT_{p,qs}/keV)^{3/4}. \quad (A.3)$$

Using the expression for the ratio τ_r/τ_c on page 252 of VM, we found $\tau_r/\tau_c = \mu \times f$, with the parameter μ depending only on the exponent of the temperature in the expression for the radiative loss (for temperature above 20 MK, $\mu = 0.18$), and the multiplicative function f coming from the expression for the mean conductive energy loss (formula [7] of VM), which is equal to 4/7 for a loop with a constant section. Thus, $\tau_r/\tau_c = 0.1$. [1] In other words, the quasi-static model implies that 91 % of the lost energy are radiative : radiation is the dominant energy loss process.

Assuming that the cooling is only radiative, we can use simplified relations based on the exponential decay of the light curve, the temperature, and the EM:

$$n_e = 4.4 \times 10^{10}\,cm^{-3} \times (\tau_d/10\,ks)^{-1} \times (kT_p/keV)^{3/4},\ for\ kT > 2\,keV, \quad (A.4)$$

$$L = 7.4\,R_\odot \times (a/0.07)^{-2/3} \times (\tau_d/10\,ks)^{2/3} \times (kT_p/keV)^{-1/2} \times (EM_p/10^{54})^{1/3}, \quad (A.5)$$

with kT_p (EM_p) the peak value of the temperature (EM).

[1] VM wrote $\tau_r/\tau_c = \mu = 0.18$, and the analytical expression for the conductive energy loss in the quasi-static model without taking this multiplicative factor 4/7 into account (see Table 5 of VM).

A.2 Magnetic Field

Assuming equi-partition between the magnetic pressure $B^2/8\pi$ and the ionized gas pressure $2n_e kT$, we can obtain the minimum value of the magnetic field which confine the X-ray emitting plasma:

$$B = 28.4\,G \times (n_e/10^{10}\,cm^{-3})^{1/2} \times (kT/keV)^{1/2} \tag{A.6}$$

A.3 Released Energy

For estimating the energy released by a flare, we need the peak luminosity value of the flare. As the light curve must be proportional to the intrinsic luminosity, we can fit the time averaged intrinsic luminosities with the same model used for the light curve fitting. This gives the peak luminosity, $L_{X,\,peak}$, and a characteristic decay time τ. Thus, the total energy released by a flare is:

$$E_{tot} \sim 10^{35}\,erg \times (L_{X,\,peak}/10^{32}\,erg\ ,s^{-1}) \times (\tau/ks) \tag{A.7}$$

References

Adams, F. C., Lada, C. J., Shu, F. H. 1987, ApJ. 312, 788

Agrawal, P. C., Koyama, K., Matsuoka, M., Tanaka, Y. 1986

Alcalá, J. M., Krautter, J., Covino, E., Neuhäuser, R., Schmitt, J. H. M. M., Appenzeller, I., Jankovics, I., Krautter, J. 1983, A&A 225, 432

Wichmann, R. 1997, A&A Trefe.tex 319, 184

Anderson, I. M., Harju, J., Knee, L. B. G., Haikala, L. K. 1997, A&A 321, 575

André, P., Martin-Pintado, J., Montemerle, T. 1990, A&A, 236, 180

André, P. 1994, In The Cold Universe, ed. T. Montmerle, C. J. Lada, I. F. Mirabel, J. Trân Thanh Vân, pp. 179, 92. Gif-sur-Yvette, France: Frontières

André, P., Montmerle, T. 1994, ApJ 420, 837

André, P., Ward-Thompson, D., Barsony, M. 1993, ApJ 406, 122

Anglada, G., et al. 1989, ApJ 341, 208

Appl, S., Camenzind, M. 1992, A&A 256, 354

Bachiller, R., Cernicharo, J. 1984, A&A 140, 414

Bachiller, R., Cernicharo, J. 1986a, A&A 166, 283

Bachiller, R., Cernicharo, J. 1986b, A&A 168, 262

Bachiller, R., Cernicharo, J., Martin-Pínтado, J., Tafalla, M., Lazareff, B. 1990, A&A 231, 174

Bachiller, R., Andre, P., Cabrit, S. 1991a, A&A 241, L43

Bachiller, R., Martin-Pintado, J., Fuente, A. 1991b, A&A 243, L21

Bachiller, R., Terebey, S., Jarrett, T., Martín-Pintado, J., Beichman, C. A., van Buren, D. 1994b, ApJ 437, 296

Bachiller, R., Guilloteau, S., Dutrey, A., Planesas, P., Martin-Pintado, J. 1995, A&A 299, 857

Bally, J., Devine, D. 1994, ApJL 428, L65

Bally, J., Devine, D., Hereld, M., Rauscher, B. J. 1993a, ApJL 418, L75

Bally, J., Lada, C. J., Lane, A. P. 1993b, ApJ 418, 322

Bally, J., Stark, A. A. 1983, ApJL, 266, L61

Bally, J., Devine, D., Alten, V., Sutherland, R. S. 1997, ApJ 478, 603

Barsony, M. 1995, In Clouds, Cores, and Low Mass Stars, ed. D. P. Clemens, R. Barvainis, pp. 197, San Francisco: Astron. Soc. Pac.

Barsony, M., Kenyon, S. J., Lada, E. A., & Teuben, P. J. 1997, ApJS 112, 109

Beichman, C. A. et al. 1986, ApJ 307, 337

Benson, P. C., Myers, P. C. 1989, ApJS 71, 89

Bertout, C, Regev, O. 1992, ApJL, 399, L163

Batrla, W., Wilson, T. L., Bastien, P., Ruf, K. 1983, A&A 128, 279

Bibo, E. A., Thé, P. S., Dawanas, D. N., 1992, A&A 260, 293

Bieging, J. H., Cohen, M. 1985, ApJL 289, L5

Bieging, J. H., Cohen, M., Schwartz, P. R. 1984, ApJ 282, 699

Blaauw, A. 1991, In The Physics of Star Formation and Early Stellar Evolution, eds. C. J. Lada and N. D. Kylafis (Dordrecht: Kluwer), pp. 125–154

Blake, G. A., Mundy, L. G., Carlstrom, J. E., Padin, S. Scott, S. L., Scoville, N. Z., Woody, D. P. 1996, ApJ 472, L19

Bontemps, S., André, P., Tereby, S., Cabrit, S. 1996, A&A 311, 858

Borgman & Bllauw 1990

Bouvier, J. 1990, AJ 99, 946

Bouvier, J., Appenzeller, I. 1992, A&A 92, 481

Bouvier, J., Bertout, C., Benz, W., Mayor, M. 1986, A&A 165, 110

Brown, A. 1987, ApJL 322, 31

Bührke, Th., Mundt, R., Ray, T. P. 1988, A&A 200, 99

Burke, B. E., Mountain, R. W., Daniels, P. J., Dolat, V. S., Cooper,M. J.1994, IEEE Trans. Nucl. Sci. 41, 375

Cabrit, S., Bertout, C. 1986, ApJ 307, 313

Cabrit, S., Bertout, C. 1990, ApJ 348, 530

Cabrit, S., André, P. 1991, ApJL 379, L25

Camenzind, M. 1990, Rev. Mod. Astron. 3, 234

Cappa de Nicolau, C. E., Pöppel, W. G. L., 1991 A&AS 88, 615

Carkner, L., Feigelson, E. D., Koyama, K., Montmerle,T. 1995, A&AS 186, 905

Carkner, L., Kozak, J. A., Feigelson, E. 1998, AJ 116, 1933

Casali, M. M., Eiroa, C., Duncan, W. D. 1993, A&A 306, 427

Casanova, S., Montmerle, T., Feigelson, E. D., André, P. 1995, ApJ 439, 752

Castets, A., Langer, W. D. 1994, A&A 294, 835

Cernicharo, J., Bachiller, R., Duvert, G., Gonzlez-Alfonso, E., Gmez-Gonzlez, J. 1992. A&A 261, 589

Cernicharo, J., Reipurth, B. 1996, Preprint

Chernin, L., Masson, C. R., Pino, E. G. D., Benz, W. 1994, ApJ 426, 204

Cernis, K. 1990, Ap&SS 166, 35

Cesaroni, R., Olmi, L., Walmsley, C. M., Churchwell, E., Hofner, P. 1994, ApJL 435, L137

Cesaroni, R., Wilson,T. L. 1994, A&A 281, 209

Chandler, C., Wood, D. O. S. 1997, MNRAS 287, 445

Chen, H., Myers, P. C., Ladd, E. F., Wood, D. O. 1995, ApJ 445, 377

Chen, H., Grenfell, T. G., Myers, P. C., Huges, J. D. 1997, ApJ 478, 295

Chernin, L. M., Masson, C. R. 1995a, ApJ 443, 181

Chini, R. 1981, A&A 99, 346

Chini, R., Reipurth, B., Ward-Thompson, D., Bally, J., Nyman, L.-A., Sievers, A., Billawala, Y. 1997a, ApJ 474, L135

Chini, R., Reipurth, B., Sievers, A., Ward-Thompson, D., Haslam, C. G. T., Kreysa, E., Lemke, R. 1997b, A&A 325, 542

Cohen, M., Bieging, J. H., Schwartz, P. R. 1982, ApJ 253, 707

Cohen, M., Kuhi, L. V. 1979, ApJS 41, 743

Cohen, M., Schwarts, R. D. 1980, MNRAS 191, 165

Cohen, M. 1980, AJ 85, 29

Cohen, M., Schwarts, R. D. 1983, ApJ 265, 877

Cohen, M., Schwarts, R. D. 1987, ApJ 316, 311

Cohen, M. 1990, ApJ 354, 701 (erratum: ApJ 362, 758)

Comerón, F., Torra, J. 1992, A&A 261, 94

Comerón, F., Torra, J. 1994, A&A 281, 35

Contopoulos, J., Lovelace, R. V. E. 1994, ApJ 429, 139

Cully, S. L., Siegmund, O. H. W., Vedder, P. W., & Vallerga, J. V. 1993, ApJL 414, L49

Curiel, S., Raymond, J., Rodriguez, L. F., Canto, J., Moran, J. M. 1990, ApJ 365, L85

Curiel, S., Rodríguez, L. F., Moran, J. M., Cant, J. 1993, ApJ 415, 191

Dame, T. M., Ungerechts, R. S., Cohen, R. S., De Geus, E. J., Grenier, I. A. 1987, ApJ 322, 706

Davis, C. J., Dent, W. R. F., Matthews, H. E., Aspin, C., Lightfoot, J. F. 1994a, MNRAS 266, 933

Davis, C. J., Eislöffel, J. 1995, A&A 300, 851

De Campli, W. M. 1981, ApJ 244, 124

De Geus, E., de Zeeuw, P. T., Lub, J. 1989, A&A 216, 44

Dent, W. R. F, Matthews, H. E., Walther, D. M. 1995, MNRAS 277, 193

Dougados, C., Carpenter, J., Meyer, M., Strom, S. E. 1996, Preprint

Doyle, J. G., et al. 1991, MNRAS 248, 503

Draine, B. T., Roberge, W. G., Dalgarno, A. 1983, ApJ 264, 485

Edwards, S., Snell, R. L. 1984, ApJ 281, 237

Edwards, S. 1995, Rev. Mex. Astron. Astrof. (Ser. Conf.) 1, 309

Edwards, S., Ray, T., Mundt, R. 1993, In Protostars and Planets III, ed. E. H. Levy, J. I. Lunine, pp. 567, Tucson: Univ. Ariz. Press

Eiroa, C., Casali, M. M. 1989, A&A 223, L17

Eiroa, C. 1991, In: Reipurth, B. (ed) Low Mass Star Formation in Southern Molecular Clouds, ESO Scientific Report No.11, p.197

Eiroa, C., Casali, M. M. 1992, A&A 262, 468

Eiroa, C., Torrelles, J. M., Gomez, J. F., et al. 1992, PASJ 44, 155

Elias, J. H. 1978a, ApJ 224, 453

Elias, J. H. 1978c, ApJ 224, 857

Feigelson 1994, in New Horizon of X-Ray Astronomy, ed. F. Makino & T. Ohashi (Universal Academy Press, inc), 21

Feigelson, E. D., Casanova, S., Montmerle, T., Guibert, J. 1993, ApJ 416, 623

Feigelson, E. D., DeCampli, W. M. 1981, ApJL 243, L89

Feigelson, E. D., Montmerle, T. 1999, ARA&A in press

Feldman, U., Laming, J. M., Doschek, G. A. 1995, ApJ 451, L79

Ferreira, J., Pelletier, G. 1993a, A&A 276, 625

Ferreira, J., Pelletier, G. 1993b, A&A 276, 637

Ferreira, J., Pelletier, G. 1995, A&A 295, 807

Fukui, Y., Iwata, T., Mizuno, A., Bally, J., Lane, A. P. 1993, in Protostars and Planets III, ed. E. H. Levy, J. I. Lunine, (tucson & London: Univ. of Arizona Press), p. 603

Gagné, M. G., Caillault, J-P., Stauffer, J. R. 1995, ApJ 445, 280

Gahm, G. F., Johanson, L. E. B., Liseau, R. 1993, A&A 274, 415

Garden, R. P., Hayashi, M., Gatley, I., Hasegawa, T., Kaifu, N. 1991, ApJ, 374, 540

Genzel, R., Stutzki, J. 1989, ARA&A 27, 41

Gibb, A. G., Litte, L. T., Heaton, B. D., Lehtinen, K. K. 1995, MNRAS 277, 341

Gimore, W. 1980, AJ 85, 894

Giovannetti, P., Caux, E., Nadeau, D., Monin, J.-L. 1998, A&A 330, 990

Giovanardi, C., Lizano, S., Natta, A., Evans, N. J. II, Heiles, C. 1992, ApJ 397, 214

Gotthelf, E. 1996, ASCANEWS (Greenbelt: NASA GSFC) 4, 31

Gould, B. A. 1879, Uranometria Argentina, ed. P. E. Corni, Buenos Aires, p.354

Gredel, R., Dalgarno, A. 1995, ApJ 446, 852

Greene, T. P., Young, E. T. 1989, ApJ 339, 258

Greene, T., Lada, C. 1996, ApJ 461, 345

Greene, T., Meyer, M. R. 1995, ApJ 450, 233

Greene, T. P., Wilking, B. A., André, P., Young, E. T., Lada, C. J. 1994, ApJ 434, 514

Grosso, N., Montmerle, T., Feigelson, E. D., André, P., Casanova, S., Gregorio-Hetem, J. 1997, Nature 387, 56

Guilloteau, S., Bachiller, R., Fuente, A., Lucas, R. 1992, A&A 265, L49

Guillout, P., Sterzik, M. F., Schmitt, J. H. M. M, Motch, C., Neuhäuser, R. 1998a, A&A 337, 113

Guillout, P., Sterzik, M. F., Schmitt, J. H. M. M, Motch, C., Egret, D., Voges, W., Neuhäuser, R. 1998b, A&A 334, 540

Hanner, M. S., Brooke, T. Y., Tokunaga, A. T. 1995, ApJ 438, 250

Harju, J., Walmsley, C. M., & Wouterloot, J. G. A. 1991, A&A 245, 64

Harju, J., Walmsley, C. M., & Wouterloot, J. G. A. 1993, A&AS 98, 51

Hartmann, L. W., Soderblom, D. R., Stauffer, J. R. 1987, AJ 93, 907

Harvey, P., Joy, M., Wilking, B.A. 1984, ApJ 278, 156

Hayashi, M., Hasegawa, T., Ohashi, N., Sunada, K. 1994, ApJ 426, L324

Hayashi, M. R., Shibata, K., & Matsumoto, R. 1996, ApJL, 468, L37

Henning, Th., Laundhardt, R., Steinacker, J., Thamm, E., 1994, A&A 291, 546

Herbig, G. H. 1963, ApJ 137, 398

Herbig, G. H., Jones, B. F. 1983, AJ 88, 1040

Herbig, G. H., Vrba, G. H., Rydgren, A.E. 1986, AJ 91, 575

Henriksen, R. N., Ptuskin, V. S., Mirabel, I. F. 1991, A&A 248, 221

Heyer, M. H., Graham, J. A. 1989, PASP 100, 816

Hirano, N., Kameya, O., Kasuga, T., Umemoto, T. 1992, ApJ 390, L85

Ho P. T. P., Barrett, A. H., Myers, P. C., Matsakis, D. N., Cheung, A. C., Chui, M. F., Townes, C. H., Yngvesson, K. S. 1979, ApJ 234, 912

Hodapp, K. W. 1994, ApJS 94, 615

Huges, J., Hartigan, P., Clampitt, L. 1993, AJ 105, 571

Huges, J., Hartigan, P., Krautter, J., Kelemen, J. 1994, AJ 108, 1071

Huges, J., Hartigan, P., Krautter, J., Kelemen, J. 1992, AAS 181, 10305

Hurt, R. L., Barsony, M., Wootten, A. 1996, ApJ 456, 686

Hurt, R. L., Barsony, M. 1996, ApJ 460, L45

Ishisaki, Y., Matsuzaki, K., Shirahashi, A., Takahashi, T., & Itoh, R. 1998, Interactive Tool for Data Analysis for DISPLAY45 (version 1.80)

Janesick, J., Elliott, T. Garmire, G. 1985, Proc. X-ray Instrumentation in Astronomy, SPIE 597, 364

Jarrett, T. H., Dickman, R. L., Herbst, W. 1989, ApJ 345, 881

Jennings, R., Cameron, D., Cudlip, W., Hirst, C. 1987, MNRAS 226, 461

Jones, B. F., Herbig, G. H. 1979, AJ 84, 1872

Jones, B. F., Cohen, M., Sirk, M., Jarrett, R. 1984, AJ 89, 1404

Kamata, Y., Koyama, K., Tsuboi, Y., & Yamauchi, S. 1997, PASJ 49, 461

Keene, J., Masson, C. R. 1990, ApJ 355, 635

Kenyon, S. T., Hartmann, L. W., Strom, K. M., Strom, S. E. 1990, AJ 99, 869

Kenyon, S. J., Calvet, N., Hartmann, L. 1993, ApJ 414, 676

Keto, E. R., Ho, P. T. P., Haschick, A. D. 1988, ApJ 324, 920

Knackle, R. F., Strom, K. M., Strom, S. E., Kunkel, W. E. 1973, ApJ 179, 847

Knee, L. B. G., CAmeron, M., Liseau, R. 1990, A&A 231, 419

Knude, J., Hog, E. 1998, A&A 338, 897

Königl, A. 1989, ApJ 342, 208

Königl, A. 1991, ApJL 370, L39

Königl, A., Ruden, S. P. 1993, In Protostars and Planets III, ed. E. H. Levy, J. I. Lunine, pp. 641, Tucson: Univ. Ariz. Press

Krautter, j., Kelemen, J. 1987, Mitt. Astron. Ges. 70, 397

Krautter, J. 1991, In: Reipurth, B. (ed) Low Mass Star Formation in Southern Molecu lar Clouds, ESO Scientific Report No.11, p.197

Krautter, J., Wichmann, R., Schmitt, J. H. M. M., Alcala, J. M., Neuhäuser, R., Terranegra, L. 1997, A&AS 123, 329

Koyama, K. 1987, PASJ 39, 245

Koyama, K., Asaoka, I., Kuriyama, T., Tawara, Y. 1992, PASJ 44, L225

Koyama, K., Maeda, Y., Ozaki, M., Ueno, S., Kamata, Y., Tawara, Y., Skinner, S., Yamauchi, S. 1994, PASJ 46, L125

Koyama, K., Hamaguchi, K., Ueno, S., Naoto, K., Feigelson, E. D. 1996, PASJ 48, L87

Lada, C. J., Gottlieb, C., Litvak, M., Lilley, A. E. 1974, ApJ 194, 609

Lada, C. J. 1985, ARA&A 23, 267

Lada, C. J. 1987, Proc. IAU Symp. 115, eds. M.Peimbert and J. Jugaku (Dordrecht: D. Reidel), pp. 1–18

Lada, C. J. 1991, In The Physics of Star Formation and Early Evolution, ed. C. J. Lada, N. D. Kylafis, pp. 329. Kluwer: Dordrecht

Lada, C. J., Wilking, B. A. 1984, ApJ 287, 610

Lada, E. A., Bally, J. Stark, A. 1991, ApJ 368, 432

Ladd, E. F., Lada, E. A., Myers, P. C. 1993, ApJ 410, 168

de Lara, E., Chavarria-K., C., Lopéz-Molina, G., 1991, A&A 243, 139

Leous, J. A., Feigelson, E. D., André, P., Montmerle, T., 1991, ApJ 379, 683

Levreault, R. M. 1988, ApJS 67, 283

Levy, E. H., Araki, S. 1989, Icarus 81, 74

Lis, D. C., Serabyn, E., Keene, J., Dowell, C. D., Benford, D. J., Phillips, T. G., Hunter, T. R., Wang, N. 1998, accepted by ApJ

Lizano, S., Heiles, C., Rodríguez, L. F., Koo. B. C., Shu, F. H. et al. 1988, ApJ 328, 763

Loren, R. B., Sandqvist, A., Wootten, A. 1983, ApJ 270, 620

Loren, R. B. 1989a, ApJ 338, 902

Loren, R. B. 1989b, ApJ 338, 925

Lovelace, R. V. E., Berk, H. L., Contopoulos, J. 1991, ApJ 376, 696

Lovelace, R. V. E., Romanova, M. M., Contopoulos, J. 1993, ApJ 403, 158

Maddalena, R. J., Moscowitz, J., Thaddeus, P., Morris, M. 1986, ApJ 303, 375

Maddalena, R. J., Morris, M. 1987, ApJ 323, 179

Makishima, K., Tashiro, M., Ebisawa, K., Ezawa, H., Fukazawa, Y., Gunji, S., Hirayama, M., Idesawa, E., Ikebe, Y. et al. 1996, PASJ 48, 171

Marraco, H. G., Rydgren, A. E. 1981, AJ 86, 62

McCaughrean, M. J., Rayner, J. T., Zinnecker, H. 1994, ApJL 436, L189

McMullin, J. P., Mundy, L. G., Wilking, B. A., Hezel, T., Blake, G. A. 1994, ApJ 424, 222

Migenes, V., Johnston, K. J., Pauls, T. A., Wilson, T. L., 1989, ApJ 347, 294

Mizuno, A., Fukui, Y., Iwata, T., Nozawa, S., Takano, T. 1990, ApJ 356, 184

Mizuno, A., Onishi, T., Hayashi, M., Ohashi, N. Sunada, K., Hasegawa, T., Fukui, Y. 1994, Nature 368, 719

Mizuno, A., Onishi, T., Yonekura, Y., Nagahama, T., Ogawa, H., Fukui, Y. 1995, ApJ 445, L161

Moneti, A., Reipurth, B. 1995, A&A 301, 721

Monin, J.-L., Pudritz, R. E., Razareff, B. 1996, A&A 305, 502

Montmerle, T., Koch-Miramond, L., Falgarone, E., Grindlay, J. E. 1983, ApJ 269, 182

Montmerle, T., Feigelson, E. D., Bouvier, J., & André, P. 1993, in Protostars and Planets III, ed. E. H. Levy & J. I. Lunine (Tucson: Univ.Arizona Press), 689

Morse, J. A., Hartigan, P., Cecil, G., Raymond, J. C., Heathcote, S. 1992, ApJ 399, 231

Morrison, R., McCammon, D. 1983, ApJ 270, 119

Motte, F., André, P., Neri, R. 1998 A&A 336, 150

Mundt, R., Fried, J. W. 1983, ApJL 274, L83

Murata, Y., Kawabe, R., Ishiguro, M., Kasuga, T., Morita, K.-I., Takano, T., Hasegawa, T. 1990, ApJ 359, 125

Myers, P. C., Benson, P. J. 1983, ApJ 266, 309

Myers, P. C. 1985, in Protostar and Planets II, eds. D. C. Black and M. S. Matthews (Tucson: Univ. of Arizona), pp. 81

Myers, P. C., Fuller, G. A., Mathieu, R. D., Beichman, C. A., Benson, P. J., Schild, R. E., Emerson, J. P. 1987, 319, 340

Myers, P. C., Bachiller, R. B., Caselli, P., Fuller, G. A., Mardones, D. et al. 1995, ApJL 449, L65

Myers, P. C., Fuller, G. A., Mathieu, R. D., Beichman, C. A., Benson, P. J. et al. 1987, ApJ 319, 340

Myers, P. C., Ladd, E. F. 1993, ApJL 413, L47

Najita, J. R., Shu, F. H. 1994, ApJ 429, 808

Neuhäuser, R., Sterzik, M. F., Schmitt, J. H. M. M., Wichmann, R., Krautter, J. 1995, A&A4 297, 391

Neuhäuser, R., Preibisch, Th. 1997, A&A 322, L37

Ohashi, N. 1992, Ph.D. thesis, Nagoya Univ.

Ohashi, T., Ebisawa, K., Fukazawa, Y., Hiyoshi, K., Horii, M., Ikebe, Y., Ikeda, H., Inoue, H. et al. 1996, PASJ 48, 157

Ohashi, N. Hayashi, M., Ho, P. T. P., Momose, M., Hirono, N. 1996, ApJ 466, 957

Ohyama, M., Shibata, K. 1998, ApJ 499, 934

Onishi, T., Mizuno, A., Kawamura, A., Ogawa, H., Fukui, Y. 1998, ApJ 502, 296

van den Oord, G. H. J., Mewe, R. 1989, A&A 213, 245

Ostriker, E. C., Shu, F. H. 1995, ApJ 447, 813

Ozawa, H., Nagase, F., Ueda, Y., Dotani, T., Ishida, M. 1999, ApJ 523, L81

Pelletier, G., Pudritz, R. E. 1992, ApJ 394, 117

Persi, R., Palagi, F., Felli, M. 1994, A&A 291, 577

Phillips, J. P., White, G. J., Rainey, R. R., Avery, L. W., Richardson, K. J., Griffin, M. J., Cronin, N. J., Monteiro, T., Hilton, J. 1988, A&A 190, 289

Pöpel, W. 1997, Fundamental of Cosmic Physics, Vol. 18

Preibisch, T., Zinnecker, H., & Schmitt, J. H. M. M. 1993, A&A 279, L33

Preibisch, T., Neuhäuser, R., & Alcala, J. M. 1995, A&A 304, L13

Preibisch, T., Sonnhalter, C., Yorke, H. 1995, A&A 299, 144

Preibisch, T. 1996, A&A 310, 456

Preibisch, T. 1997, A&A 324, 690

Preibisch, Th. 1998, A&A 338, L25

Pringle, J. E. 1989, MNRAS 236, 107

Prusti, T., Clark, F. O., Laureijs, R. J., Wakker, B. P., Wesselius, P. R. 1992, A&A 259, 537

Pudritz, R. E., Pelletier, G., Gómez de Castro, A. I. 1991, In The Physics of Star Formation and Early Evolution, ed. C. J. Lada, N. D. Kylafis, pp. 539, Kluwer: Dordrecht

Reipurth, B., Wamsteker, W. 1983, A&A 119, 14

Reipurth, B. 1985, A&AS 61, 319

Reipurth, B., Bally, J., Graham, J. A., Lane, A. P., Zealey, W. J. 1986, A&A 164, 51

Reipurth, B. 1989, A&A 220, 249

Reipurth, B., Cernicharo, C. 1995, Rev. Mex. Astron. Astrof. (Ser. Conf.) 1, 43

Reipurth, B., Heathcote, S. 1992, A&A 257, 693

Reipurth, B., Eiroa, C. 1992, A&A 256, L1

Reipurth, B. 1993, ApJ 408, 49

Reynolds, S. P. 1986, ApJ 304, 713

Richer, J. S., Hills, R. E., Padman, R. 1992, MNRAS 254, 525

Rodríguez, L. F., Lizano, S., Cantó, J., Escalante, V., Mirabel, I. F. 1990, ApJ 365, 261

Rosner, R., Golub, L., Vaiana, G. S. 1985, ARA&A 23, 413

Rossano, G. S. 1978 AJ 83, 234

Rosso, F., Pelletier, G. 1994, A&A 287, 325

Rudolph, A., Welch, W. J., Palmer, P., Dubrulle, B. 1990, ApJ 363, 528

Ruiz, A., Alonso, J. L., Mirabel, I. F. 1992, ApJL 394, L57

Russell, A. P. G., Bally, J., Padman, R., Hills, R. E. 1992, ApJ 387, 219

Rybichi, G. B., Lightman, A. P. 1979 in Radiative process in Astrophysics, a wily-interscienccе publication

Sandell, G., Aspin, C., Duncan, W. D., Russel, A. P. G., Robson, E. I. 1991, ApJ 376, L17

Saraceno, P., André, P., Ceccarelli, C., Griffin, M., Molinari, S., 1996, A&A, 309, 827

Sargent, A. I. 1979, ApJ 233, 163

Scoville, N. Z., Kwan, J. 1976, ApJ 206, 718 Serlemitsos, P. J., Jolota, L., Soong, Y., Kunieda, H., Tawara, Y., Tsusaka, Y., Suzuki, H., Sakima, Y. et al. 1995, PASJ 47, 105

Shibata, K., Uchida, Y. 1986, PASJ 38, 631

Shibata, K., Yokoyama. T. 1999, in preparation

Shimizu, T. 1995, PASJ 47, 251

Shu, F. H., Adams, F. C. & Lizano, S. 1987, ARA&A, 25, 23

Shu, F. H. 1995, Rev. Mex. Astron. Astrof. (Ser. Conf.) 1, 375

Shu, F. H., Lizano, S., Ruden, S. P., Najita, J. 1988, ApJL 328, L19

Shu, F. H., Najita, J., Ostriker, E., Wilkin, F., Ruden, S., Lizano, S. 1994a, ApJ 429, 781

Shu, F. H., Najita, J., Ruden, S., Lizano, S. 1994b, ApJ 429, 797

Shull, J. M., Beckwith, S. 1982. ARA&A 20, 163

Silk, J., Norman, C. 1983, ApJL 272, L49

Simon, M., Howell, R. R., Longmore, A. J., Wilking, B. A., Peterson, D. M., Chen, W. P. 1987, ApJ 320, 344

Skinner S., Guedel M., Koyama K., Yamauchi S. 1997, ApJ 486, 886

Smith, M. D. 1994, MNRAS 266, 238

Snell, R. L., Loren, R. B., Plambeck, R. L. 1980, ApJL 239, L17

Snell, R. L., Heyer, M. H., Schloerb, F. P. 1989, ApJ 337, 739

Stelzer, B., Neuhäser, R., Casanova, S., & Montmerle, T. 1999, A&A 344, 154

Stanke, T., McCaughrean, M. J., Zinnecker, H. 1998, A&A 332, 307

Stern, R. A., Uchida, Y., Tsuneta, S., Nagase, F. 1992, ApJ 400, 321

Strom, S. E., Grasdalen, G. L., Strom, K. M. 1974, ApJ 191, 111

Strom, S. E., Vrba, F. J., Strom, K. M. 1976, AJ 81, 638

Strom, S. E., Strom, K. M., Edwards, S. 1988, in Galactic and Extragalactic Star Formation, eds. R. Pudritz and M. Fich, (Kluwer, Doedrecht), P. 53

Strom, S. E. 1995, Rev. Mex. Astron. Astrof. (Ser. Conf.) 1, 317

Strom, K. M., Strom, S. E. 1994, ApJ 424, 237

Tachihara, K., Dobashi, K., Mizuno, A., Ogawa, H., Fukui, Y. 1996, PASJ 48, 489

Tanaka, Y., Inoue, H., Holt, S. S. 1994, PASJ 46, L37

Tatematsu, K., et al. 1993a, ApJ 404, 643

Tatematsu, K., Umemoto, T., Murata, Y., Chen, H., Hirano, N., Takaba, H. 1993b, ApJ 419, 746

Taylor, K. N. R., Storely, J. W. V. 1984, MNRAS, 209, 5P

Terebey, S., Vogel, S. N., Myers, P. C. 1989, ApJ 340, 472

Terebey, S., Beichman, C. A., Gautier, T. N., Hester, J. J. 1990, ApJL 362, L63

Terebey, S. 1991, Mem. Soc. Astron. Ital. 62(4), 823

Torbett, M. V. 1984, ApJ 278, 318

Tsuboi, y., Koyama, K., Murakami, H., Hayashi, M., Skinner, S., Ueno, S. 1998, ApJ 503, 894

Tsuneta, S. 1996, ApJ 456, 840

Tsuru, T. et al. 1989, PASJ 41, 679

Uchida, Y., Shibata, K. 1984, PASJ 36, 105

Uchida, Y., Shibata, K. 1985, PASJ 37, 515

Umemoto, T., Ohashi, N., Murata, Y., Tatematsu, K., Suzuki, M. 1994, in Astronomy with Millimeter and Submillimeter Wave Interferometry, IAU Colloqium 140, ed. M. Ishiguro & Wm. J. Welch, 245

Ungerechts. H., Güsten, R. 1984, A&A, 131, 177

Ungerechts, H. Thaddeus, P. 1987, ApJS 63, 645

Vrba, F. J., Strom, K. M., Strom, S. E., Grasdalen, G. L. 1975, ApJ 197,77

Vrba, F. J., Strom, S. E., Strom, K. M. 1976, AJ 81, 958

Walker, C. K., Narayanan, G., Boss, A. 1994, ApJ 431, 767

Walter, F. M., Brown, A., Mathieu, R. D., Myers, P. C., Vrba, F. J. 1988, AJ 96, 297

Walter, F. M., Boyd, W. T. 1991, ApJ 370, 318

Ward-Thompson, D., Scott, P. F., Hills, R. E., André, P. 1994, MNRAS 268, 276

Wardle, M., Königl, A. 1993, ApJ 410, 218

Welch, W. J. W., Dreher, J. W., Jackson, J. M., Terebey, S., Vogel, S. N. 1987, Science 238, 1550

White, G. J., Casali, M. M., Eiroa, C. 1995, A&A 298, 594

Wilking, B. A., Lada, C. J. 1983, ApJ 274, 698

Wilking, B. A., Taylor, K. N. R., Storey, J. W. V. 1986, AJ 92, 103

Wilking, B. A. 1989, PASP 101, 229

Wilking, B. A., Lada, C. J., Young, E. T. 1989, ApJ 340, 823

Wilking, B., Greene, T., Lada, C., Meyer, M., Young, E. 1992, ApJ 397, 520

Wilking, B. A., McCaughrean, M. J., Burton, M. G., Giblin, T., Rayner, J. T., Zinnecker, H. 1997, AJ 114, 2029Thé, P. S., de Winter, D., Pérez, M. R. 1994, A&AS 104, 315

Wilner, D. J., Welch, W. J., Forster, J. R. 1995, ApJL 449, L73

Wilson, T. L., Gaume, R. A., Johnston, K. J., Schmid-Burgk, J. 1996, in 'Science with Large Millimeter Arrays', ed. P. Shaver, (Heidelverg: Springer-verlag), 177

Wiramihardja, S. D., Kogure, T., Yoshida, S. Ogura, K., Nakano, M. 1989, PASJ 41, 155

Wiseman, J. J., Ho, P. T. P. 1996, Nature 382, 139

Wolf, G., Lada, C. J., Bally, J. 1990, AJ 100, 1892

Wright, M. C. H., Plambeck, R. L., Wilner, D. J. 1996, ApJ 469, 216

Wu, Y., Huang, M., He, J. 1996, A&AS 115, 283

Yamauchi, S., Koyama, K. 1993, ApJ 405, 268

Yamauchi et al. 1999 accepeted by ApJ

Yu, K. C., Bally, J., Devine, D. 1997, ApJ 485, L45

Yusef-Zadeh, F., Cornwell, T. J., Reipurth, B., Roth, M. 1990, ApJ 348, L61

Yusef-Zadeh, F., Cornwell, T., Reipurth, B. 1990, ApJ 348, L64

Zhou, S., Evans, N. J. II, Kömpe, C., Walmsley, C. M. 1993, ApJ 404, 232

Zickgraf, F. -J., Alcala, J. M., Krautter, J., Sterzik, M. F., Appenzeller, I., Motch, C., Pakull, M. W. 1998, A&A 339, 457

Zinnecker, H., Chelli, A., Perrier, C. 1986, in IAU Symp. 115, Star-forming Regions, ed. M. Peimbert, J. Jugaku (Dordrecht: Kluwer), 71

Zinnecker, H., McCaughrean, M., Rayner, J. 1998, Nature 394, 862